

MIXTURES OF POLYELECTROLYTES AND SURFACTANTS AT THE  
OIL/WATER INTERFACE

by

BRANDON K. SCHABES

A DISSERTATION

Presented to the Department of Chemistry and Biochemistry  
and the Graduate School of the University of Oregon  
in partial fulfillment of the requirements  
for the degree of  
Doctor of Philosophy

June 2019

DISSERTATION APPROVAL PAGE

Student: Brandon K. Schabes

Title: Mixtures of Polyelectrolytes and Surfactants at the Oil/Water Interface

This dissertation has been accepted and approved in partial fulfillment of the requirements for the Doctor of Philosophy degree in the Department of Chemistry and Biochemistry by:

Marina Guenza	Chairperson
Geraldine L. Richmond	Advisor
Mark C. Lonergan	Core Member
Raghuveer Parthasarathy	Institutional Representative

and

Janet Woodruff-Borden	Vice Provost and Dean of the Graduate School
-----------------------	--

Original approval signatures are on file with the University of Oregon Graduate School.

Degree awarded June 2019

© 2019 Brandon K. Schabes  
This work licensed under a Creative Commons  
**Attribution-NonCommercial-ShareAlike**



## DISSERTATION ABSTRACT

Brandon K. Schabes

Doctor of Philosophy

Department of Chemistry and Biochemistry

June 2019

Title: Mixtures of Polyelectrolytes and Surfactants at the Oil/Water Interface

Life itself would not exist without chemical modification of aqueous surfaces. As humanity explores and designs ever-more-complex interfacial systems, multicomponent polymer/surfactant (P/S) mixtures could increase the functionality of designed interfaces. Many applications involve an oil phase, but understanding of P/S assembly at oil/water interfaces is lacking. Most conventional techniques are unfeasible or impossible at buried interfaces.

This dissertation uses a non-invasive and interface specific technique – vibrational sum frequency (VSF) spectroscopy – to study the fundamental forces that control coadsorbing P/S systems. Because the VSF response is nonlinear, the net orientation of the participating dipoles can be determined from the phase relationships of the resultant data. VSF spectroscopy is powerful, but not all-knowing; many corroborating techniques are used to construct a holistic model of P/S behavior.

The first three chapters of this dissertation introduce the system of interest and the techniques by which it will be explored. Chapter III introduces the benefits of selective deuteration, and the information contained within VSF spectra is explained and demonstrated for a simple surfactant interface.

Chapter IV looks critically at previous literature conclusions regarding a model P/S system. The oil/water adsorption is compared with what is known previously about adsorption at the air/water interface. Ultimately, it is found that similar electrostatic effects lead to ordered adsorption at both interfaces, but two conclusions from air/water are not replicated: the formation of multilayers and the persistence of polymer adsorption in the presence of micelles. A more robust interfacial picture is constructed, which demonstrates the wealth of information obtained from vibrational spectroscopies.

Chapter V explores a carboxylate-containing polyelectrolyte which has been used previously to model environmental humic acid molecules. The low charge-density causes hydrophobic forces to play a much larger role in P/S coadsorption. The adsorbed polymer's interfacial structure depends strongly on polymer concentration. At first, only hydrophobic P/S interactions cause modest coadsorption, but once a threshold polymer concentration is surpassed, specific electrostatic interactions uncoil adsorbed polyelectrolyte. Electrostatic effects are identified as the foremost contributor to the system's enhanced surface activity.

This dissertation includes both published and unpublished co-authored materials.

## CURRICULUM VITAE

NAME OF AUTHOR: Brandon K. Schabes

### GRADUATE AND UNDERGRADUATE SCHOOLS ATTENDED:

University of Oregon, Eugene  
Kalamazoo College, Kalamazoo

### DEGREES AWARDED:

Doctor of Philosophy, Chemistry, 2019, University of Oregon  
Bachelor of Arts, Chemistry, 2011, Kalamazoo College

### AREAS OF SPECIAL INTEREST:

Chemistry Education  
Spectroscopy of Fluid Interfaces  
Environmental Chemistry

### PROFESSIONAL EXPERIENCE:

Graduate Teaching Fellow, Department of Chemistry and Biochemistry,  
University of Oregon, Eugene, 2011 – 2018

Teaching Assistant, General Chemistry Department of Chemistry,  
Kalamazoo College, Kalamazoo, 2008 – 2011

Research Experience for Undergraduates in the Gillan Laboratory,  
University of Iowa, Iowa City, 2009

Research Experience for Undergraduates in the Cherepy and Zaitseva  
Laboratories, Lawrence Livermore National Laboratory, Livermore, 2010

### GRANTS, AWARDS, AND HONORS:

Graduate Teaching Award, Chemistry, University of Oregon, 2015

Math and Science Competitive Scholarship, Kalamazoo College, 2007 – 2010

PUBLICATIONS:

Schabes, Brandon K., Hopkins, Emma J., and Richmond, Geraldine L. “Molecular Interactions Leading to the Coadsorption of Surfactant Dodecyltrimethylammonium Bromide and Poly(styrene sulfonate) at the Oil/Water Interface.” *Langmuir*, 2019, in press.

Schabes, Brandon K., Altman, Rebecca M., and Richmond, Geraldine L. “Come Together: Molecular Details into the Synergistic Effects of Polymer–Surfactant Adsorption at the Oil/Water Interface.” *The Journal of Physical Chemistry B* 122, no. 36 (September 13, 2018): 8582–90.

Hensel, Jennifer K., Andrew P. Carpenter, Regina K. Ciszewski, Brandon K. Schabes, Clive T. Kittredge, Fred G. Moore, and Geraldine L. Richmond. “Molecular Characterization of Water and Surfactant AOT at Nanoemulsion Surfaces.” *Proceedings of the National Academy of Sciences* 114, no. 51 (December 19, 2017): 13351–56.

Zaitseva, Natalia, Andrew Glenn, Leslie Carman, Robert Hatarik, Sebastien Hamel, Michelle Faust, Brandon Schabes, Nerine Cherepy, and Stephen Payne. “Pulse Shape Discrimination in Impure and Mixed Single-Crystal Organic Scintillators.” *IEEE Transactions on Nuclear Science* 58, no. 6 (December 2011): 3411–20.

## ACKNOWLEDGMENTS

I wish to express sincere gratitude to the many people with whom I have been lucky enough to work. Geri Richmond, thank you for being both a research bulldog and science empowerment role model. To every past and current member of the Richmond lab, I appreciate and encourage your eccentric vibrancy. To Ellen Robertson, Laura McWilliams, and Andrew Carpenter, thank you for both your empathy and your advice (and for knowing which was more needed during any given catastrophe). To Brandi Baldock, Tom Greenbowe, and Randy Sullivan, thank you for understanding that teaching chemistry can be fun, and for believing in my future as an educator. This investigation was supported in part by the U.S. Department of Energy, Office of Science, Condensed Phase and Interfacial Molecular Science Division under award number DE-SC0014278.

For my parents, who made every possible sacrifice for my education.

## TABLE OF CONTENTS

Chapter	Page
I. INTRODUCTION .....	1
II. BACKGROUND, THEORY, AND EXPERIMENTAL TECHNIQUES .....	4
Interaction of Light with Matter: Second Order Processes.....	4
Spectral Fitting Procedure.....	8
Laser System and Experimental Setup .....	9
Dynamic Light Scattering .....	12
Zeta Potential Measurements .....	12
UV-Vis Turbidity Measurements .....	13
Tensiometry .....	13
Sample Preparation .....	14
Conclusions.....	15
III. THE OIL/WATER INTERFACE UNDER THE EFFECTS OF SURFACTANTS .....	17
The Neat Oil/Water Interface.....	17
Surfactant Adsorption to the Oil/Water Interface .....	19
Spectral Characteristics of the Surfactant Interface.....	22
Conclusions.....	26
IV. STRUCTURAL DETAILS OF DTAB-INDUCED ADSORPTION AND DESORPTION OF A POLYELECTROLYTE/SURFACTANT LAYER AT THE OIL/WATER INTERFACE .....	27
Introduction.....	28
Sample Preparation .....	30

Chapter	Page
DTAB Induces Adsorption of PSS .....	31
No PSS Adsorption Above the System Critical Micelle Concentration.....	36
Interfacial Charge Reversal Within the Two-Phase Region .....	38
Summary .....	40
Conclusions.....	41
<b>V. MIXED SYSTEMS, MIXED FORCES: HYDROPHOBIC AND ELECTROSTATIC POLYELECTROLYTE/SURFACTANT INTERACTIONS LEAD TO ENHANCED COADSORPTION.....</b>	<b>43</b>
Introduction.....	44
Zeta Potential and Surface Pressure Measurements .....	46
Vibrational Sum Frequency Spectroscopy Measurements .....	51
Regime I: 1.4 $\mu\text{M}$ – 4.2 $\mu\text{M}$ PAA.....	53
Regime II: 14 $\mu\text{M}$ – 140 $\mu\text{M}$ PAA.....	54
Regime III: 30 – 4200 $\mu\text{M}$ PAA .....	56
Summary .....	58
Conclusions.....	58
<b>VI. CONCLUSIONS .....</b>	<b>61</b>
<b>APPENDICES .....</b>	<b>64</b>
<b>A. FITTING PARAMETERS FOR PSS/DTAB SPECTRA.....</b>	<b>64</b>
<b>B. CALCULATION OF PAA FRACTIONAL IONIZATION.....</b>	<b>67</b>
<b>C. FITTING PARAMETERS FOR PAA/CTAB SPECTRA.....</b>	<b>70</b>
<b>REFERENCES CITED.....</b>	<b>73</b>

## LIST OF FIGURES

Figure	Page
1. Schematic of the laser setup used for VSF spectroscopy experiments.....	10
2. Schematic of the sample cell and collection geometry used.....	11
3. IR transmission of CCl <sub>4</sub> and SFG spectrum from gold.....	11
4. Schematic of the suspended gold mirror used for normalization .....	12
5. Example of a water droplet extruded into CCl <sub>4</sub> to determine surface tension.....	14
6. VSF spectra of the neat CCl <sub>4</sub> /H <sub>2</sub> O interface in the O H stretching region .....	18
7. Schematic representation of molecular environments at the oil/water interface ...	18
8. VSF spectra of the neat CCl <sub>4</sub> /H <sub>2</sub> O interface in the O H stretching region .....	19
9. Molecular structures of DTAB and CTAB.....	20
10. Dependence of n-octane/H <sub>2</sub> O surface tension on DTAB concentration.....	21
11. Dependence of n-octane/H <sub>2</sub> O surface tension on CTAB concentration.....	22
12. Dependence of n-octane/H <sub>2</sub> O surface tension on PSS concentration.....	23
13. VSF spectra of 15 μM CTAB at the CCl <sub>4</sub> /H <sub>2</sub> O and CCl <sub>4</sub> /D <sub>2</sub> O interface .....	24
14. VSF spectra of 15 μM CTAB with 2 mM NaCl at the CCl <sub>4</sub> /H <sub>2</sub> O interface .....	24
15. VSF spectra of 15 μM CTAB and 15 μM d-CTAB with 1 ppm PAA .....	26
16. Molecular structures of PSS and DTAB.....	31
17. Surface pressure isotherm, bulk zeta potential, dynamic light scattering size, and optical density for 0.10 mM PSS with variable DTAB concentration.....	32
18. Dynamic surface pressure data for DTAB and DTAB with PSS .....	34
19. VSF spectra of DTAB/PSS in the O-D and C-H stretching regions.....	35
20. VSF spectra of DTAB and DTAB/PSS in the O-D and C-H stretching regions...	37

Figure	Page
21. VSF spectra of d-DTAB/PSS in the C-D and C-H stretching regions .....	39
22. Cartoon representing adsorption of DTAB/PSS at the oil/water interface .....	41
23. Molecular structures of PAA and CTAB.....	45
24. Solution pH and bulk PAA fractional ionization.....	46
25. Bulk solution zeta potential and surface pressure as a function of PAA under fixed CTAB.....	47
26. UV/Vis extinction data for PAA/CTAB solutions at 450 nm.....	48
27. Dynamic surface tension for CTAB and PAA.....	50
28. VSF spectra of PAA/d-CTAB as a function of PAA concentration under fixed d-CTAB showing C-D and O-D modes.....	52
29. VSF spectra of PAA/d-CTAB as a function of PAA concentration under fixed d-CTAB showing carboxylate, carbonyl, and C-H modes .....	53
30. Cartoon representing the adsorption of PAA/CTAB at the oil/water interface .....	59
31. The relationship between PAA concentration and $pK_0$ .....	68
32. The relationship between PAA concentration and $m$ .....	69

## LIST OF TABLES

Table	Page
1. Nonzero elements of $\chi_{ijk}^{(2)}$ at an interface along the $xy$ plane .....	7
2. Physical characteristics of DTAB and CTAB .....	20
3. Bulk data for the concentration range studied in Chapter V .....	46
4. Parameters used to fit 15 mM DTAB/PSS spectra in Figure 4.3b.....	64
5. Parameters used to fit 15 mM d-DTAB/PSS spectra in Figure 4.5a .....	65
6. Parameters used to fit 15 mM d-DTAB/PSS spectra in Figure 4.5b .....	66
7. PAA $pK_0$ and $m$ values as used by Arnold .....	67
8. PAA fractional ionization calculated using Equation A.1 .....	68
9. Fitting parameters used for fits to experimental spectra in Chapter V .....	70

# CHAPTER I

## INTRODUCTION

*God made the bulk; surfaces were invented by the devil.*  
Wolfgang Ernst Pauli<sup>1</sup>

An extraterrestrial observer ignorant to the importance of interfaces would conclude that Earth is nothing but a molten rock. Crucial interfaces exist all over the world. Material science happens on a substrate. Gases are exchanged through surfaces. The majority of medicinal drugs target membrane proteins.<sup>2</sup> The trouble from – and the solution to – an oil spill comes from alteration of the ocean surface. The most common class of molecules which target interfaces are detergents. However, their harshness to life make them impractical for many applications. To these ends, biologically benign modification of interfaces has been proposed as a way to achieve similar results with fewer side effects.<sup>3</sup> For oil spill cleanup, this would involve fewer chemicals introduced into the environment.<sup>4-6</sup> Emulsions containing oil-soluble drugs can be rendered biocompatible by the adsorption of polymer layers which can additionally assist in targeted drug delivery.<sup>7-9</sup> Consumer-targeted 2-in-1 shampoo is specially formulated to lather away oils while simultaneously conditioning hair with silky smooth polymers.<sup>10</sup> In all three examples, the structure-function relationship of the adsorbate determines the interfacial properties.

Unfortunately, surfaces are notoriously difficult to study. Compared to the bulk, the surface is miniscule. A moderate adsorbate layer is ~2 nm thick; within the 10 mL aqueous sample with which I conduct my experiments the interface thus makes up ~0.00007% of the total volume. Most conventional analytical techniques cannot resolve the interface from the prodigious bulk. Others, like those requiring high vacuum, are impractical at fluid interfaces. Some interfacial techniques – such as small angle x-ray scattering and neutron reflectometry – can successfully characterize air/water surfaces but fail at the oil/water interface. Spectroscopic techniques involving the interaction of two or more photons are forbidden in centrosymmetric media, such as in the bulk. Chapter II of this dissertation will introduce the nonlinear spectroscopic technique vibrational sum

frequency (VSF) spectroscopy, which only gives coherent signal from oriented dipoles at the interface, where system centrosymmetry is broken. Essentially, VSF spectroscopy measures a vibrational spectrum of the interface. Since the vibrational modes of organic molecules are well characterized, VSF spectroscopy is used to determine the net orientation and bonding environment of the individual adsorbate dipoles. While VSF spectroscopy has been extensively used to study surfactant monolayers at air/water interfaces, its application to oil/water interfaces is still in its infancy. Furthermore, VSF spectroscopy has been underutilized in the study of mixed adsorbate systems such as those chronicled herein. To my knowledge, these studies are the first in which the powerful VSF spectroscopy is focused on mixed adsorption at the oil/water interface.

This work studies two classes of molecules: One seeks out surfaces, the other constructs the world. Surfactants are widespread in nature and industry due to their strong adsorption to the surface of water. Polymers make up proteins, fabrics, plastics, and much more – they can interact with surfactants both electrostatically and hydrophobically. These polymer/surfactant (P/S) combinations will form macromolecular complexes that have properties unlike either component on its own. A promising replacement for harsh detergents is the use of synergic P/S interactions, where similar surface coverage happens with the use of far less and far more benign chemicals. These “mixed” systems offer other benefits, such as specialization, functionalization, tunability, and long-term emulsion stabilization. Why – and how – different polymer surfactant combinations give rise to the properties they do has been an ongoing question in the literature for decades. This dissertation characterizes the concentration-dependent adsorption of two model P/S systems by determining the net surface charge, extent of adsorption, and polymer orientation. Chapter II outlines the theory and application of VSF spectroscopy, alongside corroborating experimental techniques. The practical application of VSF spectroscopy is demonstrated in Chapter III for a simple surfactant solution. Additionally, Chapter III demonstrates the importance of selective deuteration in vibrational spectroscopies, and relates tensiometric and spectroscopic trends. Chapter IV evaluates whether coadsorption of sodium poly(styrene sulfonate) and dodecyltrimethylammonium bromide forms complex oil/water multilayer structures such as has been previously reported at the air/water interface. Chapter IV is in press; Emma J. Hopkins performed zeta potential,

dynamic light scattering, and UV/Vis absorption measurements while Janson Hoehner assisted in collection of tensiometry data. Chapter V explores how cetyltrimethylammonium bromide interacts hydrophobically and electrostatically with poly(acrylic acid) to ultimately create three “regimes” of concentration-dependent polymer structure. Chapter V has been previously published; Rebecca M. Altman assisted in collection of tensiometry data. Lastly, Chapter VI will summarize the findings and their relevance to the field.

## CHAPTER II

### BACKGROUND, THEORY, AND EXPERIMENTAL TECHNIQUES

Despite the importance of oil/water interfaces for industrial and environmental studies, most interfacial work on aqueous systems occurs at the air/water or solid/water interface. While the behavior of oil/water interfaces is often inferred from air/water work, direct tests of their conclusions are difficult considering the inaccessibility of a buried interface to most analytical techniques. Employing techniques like neutron reflectivity, small-angle X-ray scattering, small-angle neutron scattering, ellipsometry, and atomic force microscopy at the oil/water interface is often problematic or fully impossible. Vibrational sum frequency spectroscopy (VSF) is a well-established non-linear spectroscopy that non-invasively detects oriented vibrational modes from adsorbed interfacial molecules.<sup>11-15</sup> The technique is interfacially specific and sensitive to changes of a molecule's orientation and solvation environment. However, there are experimental limitations to the information provided. This chapter describes the fundamental interactions of light with matter which give rise to the sum frequency phenomenon. This chapter also details various corroborating techniques which aid in interpretation of VSF spectra, along with sample preparation and experimental procedures.

#### **Interaction of light with matter: second order processes**

When light propagates through any medium, the oscillating electromagnetic field induces movement of the electrons within that medium. The effect induces an electric dipole,  $\boldsymbol{\mu}$ , which can be summarized mathematically as:

$$\boldsymbol{\mu} = \boldsymbol{\mu}_0 + \alpha \mathbf{E} \quad (2.1)$$

where  $\boldsymbol{\mu}_0$  is the permanent dipole of the material, and  $\alpha$  is the material's polarizability. Most materials do not contain a permanent dipole, including those studied here, so  $\boldsymbol{\mu}_0$  will not be considered further. The sum of all the induced dipoles gives the induced polarization per unit volume  $\mathbf{P}$ , which depends on the macroscopic average of  $\alpha$ , commonly known as the first-order susceptibility,  $\chi^{(1)}$ :

$$\mathbf{P} = \epsilon_0 \chi^{(1)} \mathbf{E} \quad (2.2)$$

where  $\epsilon_0$  is the vacuum permittivity. This relation explains ordinary optical phenomena like reflection and refraction, however it breaks down under high intensity electric fields, such as those produced by a laser.

When high intensity light interacts with a medium, higher-order susceptibility terms must be included to accurately describe the induced polarization:

$$\mathbf{P} = \epsilon_0(\chi^{(1)}\mathbf{E} + \chi^{(2)}\mathbf{E}^2 + \chi^{(3)}\mathbf{E}^3 + \dots) \quad (2.3)$$

where  $\chi^{(2)}$  and  $\chi^{(3)}$  are the second and third order susceptibilities, respectively, which explain how higher-order electric fields can oscillate at a different frequency than the incident light. When the interacting electric fields have identical frequency, the second term of Equation 2.3 describes “second harmonic generation” and the resultant electric field oscillates at twice the input frequency. In the case that two different frequencies of light are interacting on the medium, there are induced polarizations which oscillate at the difference (difference frequency generation) and the sum (sum frequency generation) of the two incident fields. In sum frequency spectroscopy, which is the focus of this dissertation, a visible beam  $\omega_{Vis}$  is overlapped in space and time with a tunable infrared beam  $\omega_{IR}$  to generate the sum frequency beam  $\omega_{SF}$ . Isolating the second term from Equation 2.3 and rewriting it for sum frequency spectroscopy using a visible and IR beam gives the induced second order polarization of interest for these experiments:

$$\mathbf{P}^{(2)} = \epsilon_0\chi^{(2)}\mathbf{E}_{Vis}\mathbf{E}_{IR}. \quad (2.4)$$

It can be seen that the important information obtained by VSF spectroscopy is contained within  $\chi^{(2)}$ , which explains the relationship between the incident electric fields and the resultant response. It is a third rank tensor containing 27 elements, each of which describes a different combination of input and response polarizations. Since the SFG experiment always takes place within some laboratory reference plane, it is helpful to rewrite Equation 2.4 with respect to the polarization induced in the  $i$  direction from electric fields in the  $j$  and  $k$  direction:

$$P_i^{(2)} = \epsilon_0\chi_{ijk}^{(2)}\mathbf{E}_{j,Vis}\mathbf{E}_{k,IR}. \quad (2.5)$$

Under the electric dipole approximation,<sup>11</sup> many of the  $\chi_{ijk}^{(2)}$  components are zero, due to selection rules explained below. Consider a molecular dipole within a centrosymmetric environment, such as in bulk liquid water. Since the environment is isotropic in all

directions, there will be no change in the  $\chi_{ijk}^{(2)}$  response if the direction of any given input is reversed:

$$\chi_{ijk}^{(2)} = \chi_{-i-j-k}^{(2)}. \quad (2.6)$$

Likewise, there will be no change under the reversal of the reference frame:

$$\chi_{ijk}^{(2)} = -\chi_{-i-j-k}^{(2)}. \quad (2.7)$$

The only valid solution for Equations 2.6 and 2.7 requires that  $\chi_{ijk}^{(2)} = 0$ . Thus, second order processes are forbidden in centrosymmetric media.

Notably, there is a break in centrosymmetry at a system's surface and  $\chi_{ijk}^{(2)} \neq 0$  for some combinations of  $i, j$ , and  $k$ . For these experiments I define the interface between two fluids as the  $xy$  plane, and the system has  $C_{\infty}$  symmetry along the  $z$  axis. Assuming an infinite plane, the  $x$  and  $y$  directions are equivalent ( $x = -x = -y = y$ ), but  $z \neq -z$ .

Applying Equation 2.7 to each of the 27 elements in  $\chi_{ijk}^{(2)}$ , one can determine whether the given tensor element is nonzero for a given combination of  $i, j$ , and  $k$ . For example, consider the tensor element for  $i = y, j = z$ , and  $k = z$ . Reversal of the  $y$ -axis is allowed due to the surface's  $C_{\infty}$  symmetry and gives

$$\chi_{yzz}^{(2)} = \chi_{-yzz}^{(2)} = -\chi_{yzz}^{(2)}. \quad (2.8)$$

The above equation is not satisfied unless  $\chi_{yzz}^{(2)} = 0$ . In contrast, the case where  $i = y, j = y$ , and  $k = z$  has a nonzero solution since reversal of the  $y$ -axis gives

$$\chi_{yyz}^{(2)} = \chi_{(-y)(-y)z}^{(2)} = - - \chi_{yyz}^{(2)} = \chi_{yyz}^{(2)}. \quad (2.9)$$

A thorough analysis of all 27 tensor elements identifies that 7 combinations are nonzero, and four are unique, as summarized in Table 2.1. If we define the  $xz$  plane as the plane of incidence, then  $s$ -polarized (resp.  $p$ -polarized) incident beams probe dipole elements along the  $y$  axis (resp.  $z$  and  $x$  axes). Selection of specific polarization geometries, conventionally written in order of decreasing frequency (i.e., sum frequency, visible, IR), allows VSF spectroscopy to measure specific tensor elements as summarized in Table 2.1).<sup>11</sup>

**Table 2.1.** Nonzero elements of  $\chi_{ijk}^{(2)}$  at an interface along the  $xy$  plane, along with the polarization combination which probes these elements, and the molecular orientation which is detected.

Nonzero $\chi_{ijk}^{(2)}$ elements	Polarization combination	Relation of measured vibrational dipoles to interfacial plane
$\chi_{yyz}^{(2)}$	<i>SSP</i>	<i>Perpendicular</i>
$\chi_{yzy}^{(2)}$	<i>SPS</i>	<i>Parallel</i>
$\chi_{zyy}^{(2)}$	<i>PSS</i>	<i>Parallel</i>
$\chi_{xzx}^{(2)}, \chi_{xxz}^{(2)}, \chi_{zxx}^{(2)}, \chi_{zzz}^{(2)}$	<i>PPP</i>	<i>Perpendicular and parallel</i>

The intensity of the sum frequency signal is proportional to the intensity of the incoming IR and visible beams, along with the square of the second order susceptibility,  $\chi^{(2)}$ :

$$I(\omega_{SF}) \propto |\chi^{(2)}|^2 I(\omega_{IR}) I(\omega_{vis}). \quad (2.10)$$

The second order susceptibility consists of the sum of a single nonresonant ( $\chi_{NR}^{(2)}$ ) and many resonant ( $\chi_R^{(2)}$ ) components:

$$\chi^{(2)} = \chi_{NR}^{(2)} + \sum_v \chi_{Rv}^{(2)}. \quad (2.11)$$

In dielectric media, the nonresonant component is very small and treated as a constant.<sup>14</sup> Each resonant component,  $\chi_R^{(2)}$ , depends upon the number density of molecules (N) and their frequency-dependent hyperpolarizability ( $\beta_v$ ):

$$\chi_R^{(2)} = \frac{N}{\epsilon_0} \langle \beta_v \rangle = \left( \frac{N}{\epsilon_0} \right) \frac{M_{\alpha\beta} A_\gamma}{\omega_v - \omega_{IR} + i\Gamma_v} \quad (2.12)$$

where  $M_{\alpha\beta}$  is the Raman transition moment,  $A_\gamma$  is the IR transition moment,  $\omega_v$  is the frequency of the vibrational mode,  $\omega_{IR}$  is the IR frequency, and  $\Gamma_v$  is the homogenous line width. The brackets around  $\langle \beta_v \rangle$  indicate that it is the orientational average of all contributing dipoles. Thus to be sum-frequency active, vibrational resonances must be both IR and Raman active and contain a net orientation. The greatest enhancement of sum frequency signal occurs when the IR beam is resonant with a vibrational mode on the molecule.

## Spectral fitting procedure

Since sum-frequency is a nonlinear process, interpretation of spectra is not as straightforward as for linear processes such as Raman and FTIR. The dependence of measured SFG spectra on the square of real and imaginary  $\chi_{ijk}^{(2)}$  terms means there is a mixing of vibrational resonances. In particular, overlapping vibrational modes can constructively or destructively interfere, causing unintuitive shifts in lineshape, peak width, and peak position. For this reason, it is helpful to mathematically fit spectra, which also gives credence to spectral interpretations. The fitting routine explained below was proposed by Bain in 1991,<sup>16</sup> and implemented by Moore in 2002.<sup>17</sup>

$$|\chi^{(2)}(\omega_{SF})|^2 = \left| \chi_{NR}^{(2)} e^{i\phi_{NR}} + \sum_v \int_{-\infty}^{\infty} \frac{A_v e^{i\phi_v} e^{-\left[\frac{\omega_L - \omega_v}{\Gamma_v}\right]^2}}{\omega_L - \omega_{IR} - i\Gamma_L} d\omega_L \right|^2 \quad (2.13)$$

Each peak is described by five parameters: amplitude ( $A$ ), phase ( $\phi$ ), Lorentzian linewidth ( $\Gamma_L$ ), frequency ( $\omega_v$ ), and Gaussian width ( $\Gamma_v$ ). Peak amplitude describes the intensity of the vibrational response and is allowed to fully vary during fitting. Initial guesses for peak frequency and Gaussian width are based on known literature parameters, and allowed to vary within a small window to represent peak-shifting and peak-broadening from the local bonding environment. Lorentzian linewidths are fixed based on vibrational decay lifetimes known in literature. The phase describes the “up-or-down” orientation of vibrational dipoles with relation to other detected vibrational dipoles, which can lead to constructive or destructive interferences. It is set to 0 or  $\pi$  based on the vibrational mode’s orientation relative to other vibrational modes.

Additionally, fitting takes into account a non-resonant contribution of constant amplitude,  $\chi_{NR}^{(2)}$ , and phase,  $\phi_{NR}$ . In some instances, extremely broad bands from delocalized vibrations of long-range coordinated D<sub>2</sub>O molecules at a charged interface give the appearance of nonresonant response in a specific spectral region of interest. To fit spectra within these regions, the O-D stretch signal is treated as a non-resonant response, despite having vibrational origins. This eases the fitting procedure for other peaks and allows the deduction of the orientation of interfacial water without extrapolating outside of the spectral window.

## Laser system and experimental setup

The laser system utilized for these projects was supplied by Ekspla, a subsidiary of Altos Photonics. The PL2251A is a picosecond saturable absorption semiconductor mode-locked Nd:YAG laser which generates 25 ps 1064 nm pulses at 50 Hz repetition rate. A schematic of the laser setup is shown in Figure 2.1. The 1064 nm fundamental beam is sent into a H500-SFG harmonics unit. Within this unit, the 1064 nm beam is split then split again. Two of the beams are frequency doubled to 532 nm, while the remaining 1064 nm beam is sent to the difference frequency generator within unit PG501-DFG1P. Of the two frequency-doubled 532 nm beams, one is used as the visible beam in experiments. On its way to the sample interface, this beam passes through an attenuator, delay stage, and half-wave plate which control the intensity, timing, and polarization, respectively. The other 532 nm beam enters an optical parametric generator and optical parametric amplifier whereupon it interacts with two BBO crystals to generate a tunable signal (680 – 1063 nm) and idler (1065 – 2300 nm). The idler recombines with the 1064 nm seed on a difference frequency generating AgGaS crystal to produce a 2.3 – 10  $\mu\text{m}$  (4300 – 1000  $\text{cm}^{-1}$ ) tunable IR beam. An uncertainty of 6  $\text{cm}^{-1}$  exists in all spectra due to the linewidth of the IR pulse. The polarization of the generated IR beam is selected with a periscope, which is typically the source of changes in path length between the visible and tunable IR beam. The delay stage within the visible line corrects for this and any other timing differences. The 532 nm visible beam used to generate sum frequency has an incident angle of 68 degrees and energy of 6  $\mu\text{J}$  per pulse. The IR beam has an incident angle of 76 degrees and a tunable wavelength of 2 – 10  $\mu\text{m}$ . The IR power varied from 66 – 143  $\mu\text{J}$  per pulse depending on the selected frequency. The incident angles are selected such that total internal reflection is achieved off the interface, which enhances the amount of generated sum frequency signal.<sup>12,18-21</sup> The direction of the generated sum frequency signal is at an angle between that of the reflected IR and visible beams.<sup>11</sup> Conservation of momentum dictates that the sum frequency signal is spatially much closer to the higher-frequency visible beam; in practice the difference is 1 – 2 degrees. A notch filter blocks reflected visible light, allowing the sum frequency signal to enter a monochromator and ultimately a photomultiplier tube for detection.

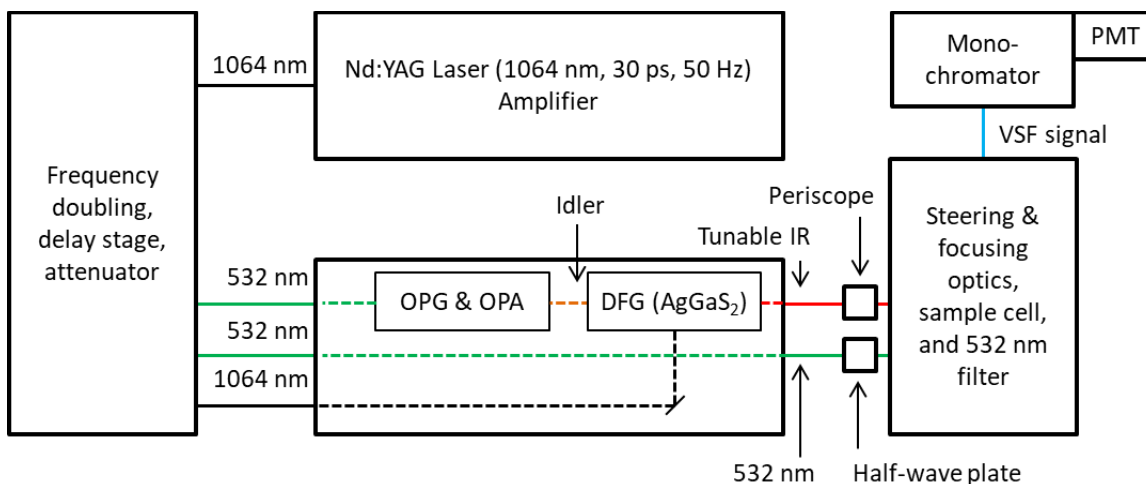


**Figure 2.1.** Schematic of the laser setup used for VSF spectroscopy experiments.

The trapezoidal sample cell represented in Figure 2.2 is made from a single machined block of Kel-F to allow for cleaning in sulfuric acid. Since the studies documented herein concern themselves with vibrational modes of water-soluble chemicals, it is impractical to transmit the IR beam through the aqueous medium, even discounting the significant IR absorbance of water. Instead, the experiment utilizes a “bottom-up” geometry whereby the visible and IR beams pass through a  $\text{CaF}_2$  window and an oil phase composed of the dense oil carbon tetrachloride.  $\text{CCl}_4$  is relatively transparent to IR and visible light at the frequencies of interest. The beams overlap in space and time at the interface, generating a sum frequency beam, which exits the cell through a quartz window. As mentioned above, selection of specific polarization schemes can probe vibrational modes with a specific orientation relative to the interface (See Table 2.1). Spectra shown in this dissertation are limited to SSP, SPS, and PPP polarization schemes, which probe perpendicular, parallel, and all changes in interfacial dipole moments, respectively.

As mentioned previously,  $\text{CCl}_4$  is *relatively* transparent to the IR frequency ranges of interest, however there are varying amounts of atmospheric and solvent absorbance bands which interfere with the IR intensity. Figure 2.3a shows the IR transmittance through  $\sim 1$  mm of  $\text{CCl}_4$  as measured by FTIR. As VSF signal is directly proportional to the intensity of the IR beam, any attenuation of incident beams will affect the final spectra. To account for lessened signal from  $\text{CCl}_4$  absorbance and any other sources, the sum frequency data collected for these experiments was divided by that obtained from the

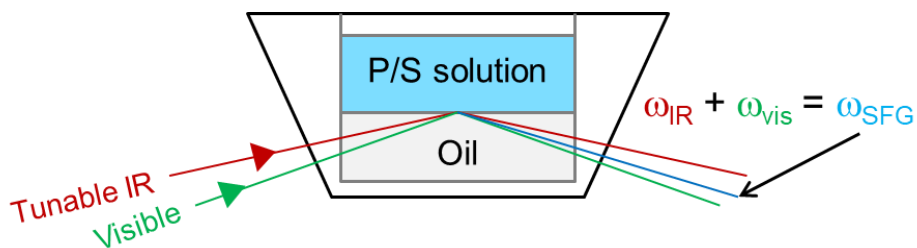


**Figure 2.2.** Schematic of the sample cell and “bottom-up” collection geometry used in VSF spectroscopy.

nonresonant response of a gold mirror suspended in  $\text{CCl}_4$  taken on the same day under identical conditions to the spectra of interest. Figure 2.3b shows the nonresonant response of a gold mirror suspended in the cell to simulate the oil/water interface (as depicted in Figure 2.4). The nonresonant response dips in the same regions that the  $\text{CCl}_4$  transmittance does, but has many other places of decreased signal that cannot be explained by the absorbance of  $\text{CCl}_4$ . These artifacts are successfully removed through normalization.

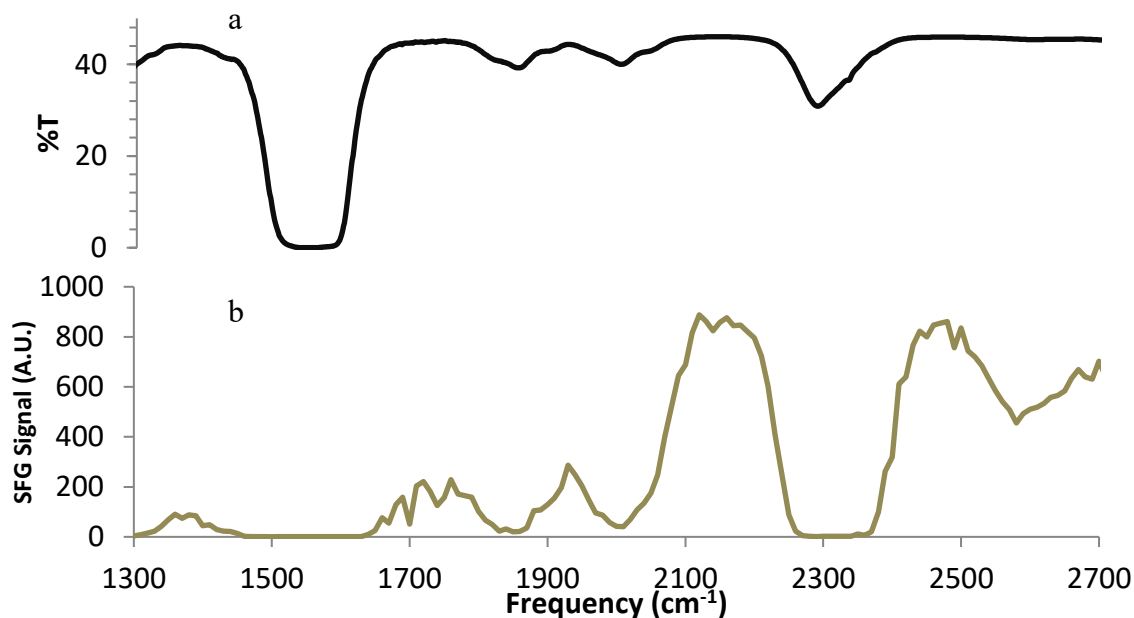


**Figure 2.3.** (a) IR % transmission through 1 mm  $\text{CCl}_4$  and (b) nonresonant SFG spectrum from gold taken in PPP polarization geometry.

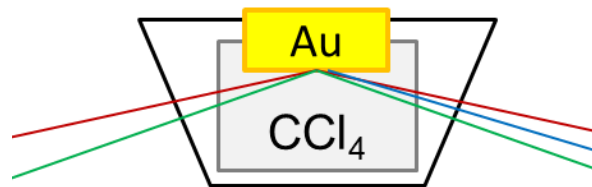


**Figure 2.4.** Schematic of the suspended gold mirror used for collecting nonresonant normalization.

### **Dynamic light scattering**

A Malvern Zetasizer Nano is used to measure the average size and polydispersity of bulk complexes using the technique of dynamic light scattering (DLS). This technique passes a 680 nm laser beam through to solution. Light is scattered off of bulk complexes with at least ~100 nm diameter. By monitoring the time dependence of the intensity of scattered light, the instrument can determine the average complex size. When oppositely charged components interact strongly *in bulk*, they tend to form larger complexes.

### **Zeta potential measurements**

The cationic surfactants and anionic polyelectrolytes of this study electrostatically interact to form charged P/S complexes, which can adsorb to the surface or remain solvated in bulk. The net charge of solvated complexes reflects the ratio of polymer to surfactant molecules within. Zeta potential measurements are performed on the same instrument as dynamic light scattering measurements (Malvern Zetasizer Nano) using a Malvern disposable folded capillary cell. By applying an alternating electric potential to the aqueous sample of interest, changes in the intensity of scattered light can be used to determine the charge of the shear plane surrounding P/S complexes solubilized in aqueous bulk. For each sample, at least three measurements were performed and the results averaged. These data are compared to interfacial phase measurements which can determine the sign and relative magnitude of the interfacial charge. Unaccounted-for charged components are assumed to be solubilized outside of bulk P/S complexes.

## UV-Vis turbidity measurements

When the zeta potential of measured complexes becomes low (approximately less than 10 mV in magnitude), electrostatic repulsion no longer prevents agglomeration of P/S complexes, and complexes tend to precipitate. The concentration region in which this occurs is known as the “two phase region” as the solution becomes visibly cloudy. Because cloudy solutions scatter so much light, DLS has difficulty determining accurate size within the two-phase region. A simpler technique is used to quantify the degree of solution turbidity. None of the components under study contain an absorbance in the visible region of the light spectrum, thus visible light is attenuated only through scattering by complexes of ~400 nm or greater. To these ends, a Perkin Elmer Lambda-1050 UV/Vis/NIR spectrophotometer is used to obtain the absorbance of the solutions from 450 – 460 nm, which quantifies the degree of precipitation and establishes the “two phase” region.

## Tensiometry

Thanks to a network of strong hydrogen bonds, the surface of water is held together by force known as “surface tension.” The interfacial adsorption of some molecules disrupts the hydrogen bond network and acts as a “bridge” between adjacent immiscible media (in this case CCl<sub>4</sub>), which lowers surface tension. Interfacial tension measurements are taken with a KSV Instruments Attension Theta Optical Tensiometer using the pendent drop method. A cuvette filled with CCl<sub>4</sub> is placed on the sample stage, where a hook-needle syringe containing the aqueous sample is inserted into the cuvette, as represented in Figure 2.5. A drop of solution is extruded into the immiscible oil phase. If the surface tension between the two fluids is high, the drop minimizes the surface area in contact with the oil, and takes on a more sphere-like shape. The instrument employs a camera which records the droplet silhouette over time. Droplet curvature is extracted from the images and fit to the Young-Laplace equation to calculate surface tension.<sup>22–24</sup>

Each day before samples were run, a neat CCl<sub>4</sub>/H<sub>2</sub>O interface is formed, and the surface tension taken to verify cleanliness by comparison to literature value for the neat CCl<sub>4</sub>/H<sub>2</sub>O interface: 44 mN/m.<sup>25,26</sup> Data collection is started immediately upon drop formation. Data are continuously acquired until sample equilibration or after 16 hours,

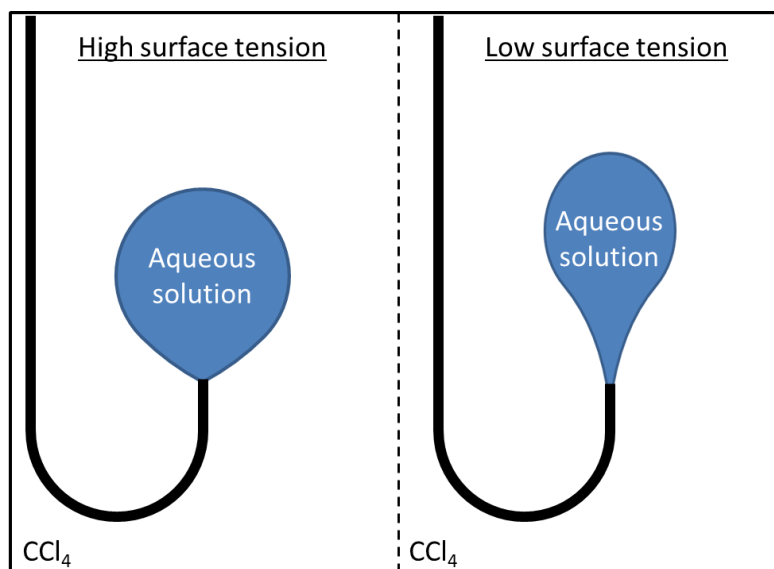


**Figure 2.5.** Example of a water droplet extruded from a hook-needle syringe into a CCl<sub>4</sub> solution to determine the surface tension.

whichever comes first. To inhibit the evaporation of CCl<sub>4</sub> from the cuvette, approximately 1 mL of water is deposited on top of the CCl<sub>4</sub> phase.

Since interfacial tensiometry measures any adsorption to the interface, it is a useful technique to run alongside VSF spectroscopy, which only detects *oriented* interfacial adsorption. There is an inverse relationship between total adsorption and interfacial tension, i.e., an increase in adsorption leads to a decrease in interfacial tension from the system's neat value. The overall magnitude of the change, called *surface pressure*, is a good measure of surface affinity, and surface pressure values are preferentially used instead of surface tension for the majority of this dissertation. Conversion to surface pressure is done by subtracting the sample's surface tension from the surface tension of that day's neat CCl<sub>4</sub>/H<sub>2</sub>O interface. At least three measurements on separate days were performed for each concentration and the results averaged.

### Sample preparation

Because of VSFS's extreme sensitivity to surface-active oils and detergents, a thorough cleaning procedure is employed. All water used for cleaning and experiments is purified with a Barnstead E-Pure Nanopurifier to 18.2 MΩ·cm of resistance. All glassware is soaked for at least 12 hours in concentrated sulfuric acid with added

oxidizing agent Nochromix, then soaked in purified water for at least 12 hours and copiously rinsed before drying overnight in a 140 °C oven. Daily confirmation of cleanliness is obtained by VSF or tensiometric assessment of the neat CCl<sub>4</sub>/H<sub>2</sub>O interface before proceeding to experiments.

P/S mixtures often have properties which rely on the interaction of surfactant molecules with charged polymer moieties, and thus the ratio of polymer to surfactant is an important system variable. Since an entire polymer “molecule” is composed of varying kilodaltons of attached monomer subunits, polymer “concentration” reported within this dissertation will be given with respect to individual monomer units. The system’s equimolar point is defined as the point at which the molar concentration of surfactant equals the molar concentration of polymer monomer units. Because P/S behavior can be heavily influenced by ionic strength, no buffer is used, and small amounts of NaOH (or NaOD) are used to adjust the stock solution pH (pD) when needed.

When large concentration gradients exist during mixing, P/S complexes can become trapped in kinetically metastable microstates.<sup>27-30</sup> To avoid this, equal volumes of polymer and surfactant are prepared separately at twice the desired concentration. Immediately before preparing the actual experiment both samples are combined and swirled vigorously for 30 seconds. All P/S samples are freshly prepared before experiments.

## Conclusions

The interfacial region of a system is difficult to study given its miniscule volume compared to the bulk. This chapter introduces surface-specific techniques which are relied upon in Chapter IV and V to determine the degree of surface adsorption in a system, along with the relative orientation and molecular environments of the adsorbed chemicals. Interfacial tensiometry is used to establish the total amount of adsorbate and the time dependence with which the adsorption occurs. Measurements of zeta potential are used to infer the ratio of polymer to surfactant in large soluble complexes. Dynamic light scattering measures the approximate size of solubilized complexes and UV-Vis absorption at 450 – 460 nm defines the “two-phase region” where precipitation occurs. Observations from the above techniques are used to aid in the interpretation of complex

vibrational information obtained from VSF spectroscopy, which measures the combined number density and net orientation of interfacial vibrational resonances. This will be put into practice throughout the next three chapters.

# CHAPTER III

## THE OIL/WATER INTERFACE UNDER THE EFFECTS OF SURFACTANTS

Although vibrational sum frequency (VSF) spectroscopy is a powerful analytical technique, there are several practical limitations to the interfacial information attained. Corroborating techniques are used to interpret spectral information, which were described in the previous chapter. This chapter relates surface tension trends to VSF spectral changes of a simple surfactant interface in preparation for later chapters. VSF spectra of the neat  $\text{CCl}_4/\text{H}_2\text{O}$  and  $\text{CCl}_4/\text{D}_2\text{O}$  interfaces are characterized. The behavior of surfactants DTAB and CTAB are described and characterized using tensiometry and VSF spectroscopy. Finally, it is explained how selective deuteration is useful for vibrational spectroscopies generally, and this study specifically.

### **The neat oil/water interface**

Hydrogen bonding at the neat oil/water interface imparts a surprising amount of structure to interfacial water molecules. When the vibrational dipoles of water contain a net orientation, they are detectable with VSF spectroscopy. The VSF spectrum for the neat  $\text{CCl}_4/\text{H}_2\text{O}$  interface is given in Figure 3.1 for a variety of polarization geometries (for more detail see Chapter II). Two main features define the spectra. There is a sharp peak at  $3665\text{ cm}^{-1}$  known as the “free OH” which arises from water molecules straddling the interface. Half the molecule is hydrogen bonding with the aqueous phase, while an uncoupled O-H oscillator protrudes into the oil phase.<sup>31</sup> The free OH mode is most pronounced in SSP because its dipole is orientated perpendicular to the interfacial plane. Greater intermolecular interactions tend to redshift and broaden vibrational modes. This can be seen for the “coordinated” O-H stretching modes from  $3000 - 3600\text{ cm}^{-1}$ .<sup>32-34</sup> Water molecules which gives signal in this region engage in two or more hydrogen bonds with neighboring water molecules. In general, water which participates in more hydrogen bonding gives signal at a lower frequency.<sup>35-37</sup> The left panel of Figure 3.2 shows a schematic representation of the neat oil/water interface. Water molecules with dangling

free OH oscillators are shown nearest to the oil phase, while water that is closer to the bulk is coordinated by a network of hydrogen bonds.

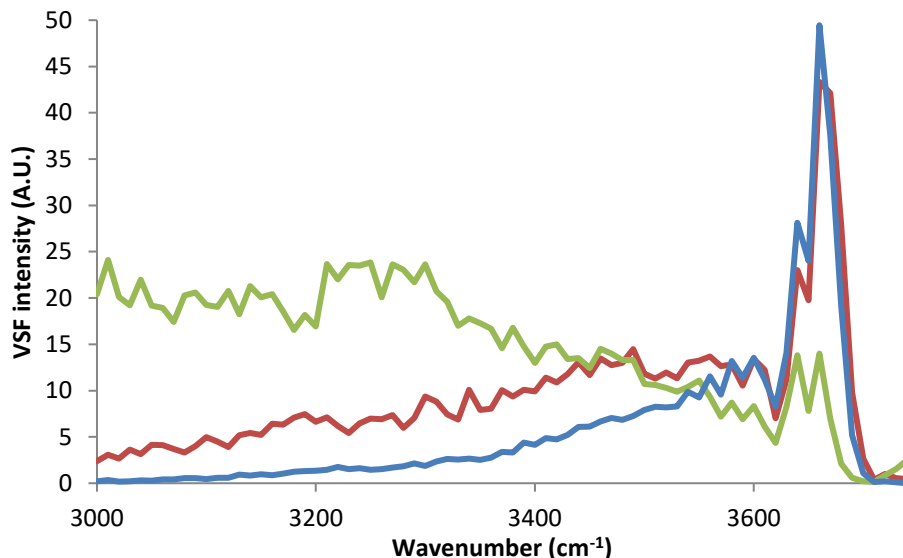


**Figure 3.1.** VSF spectra of the neat  $\text{CCl}_4/\text{H}_2\text{O}$  interface in the O-H stretching region. The red and green traces are in SSP and SPS polarization geometry, respectively. The blue trace is in PPP polarization geometry and has been scaled by a factor of 0.25.

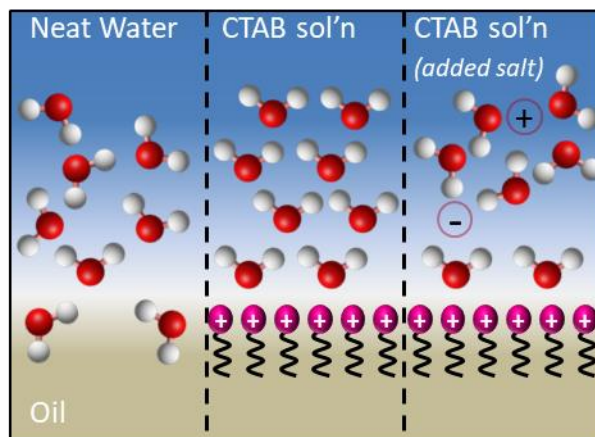


**Figure 3.2.** Schematic representation of various molecular environments at the oil/water interface.

When studying organic molecules, the most important region of the spectrum is usually the C-H stretch region between  $2800 - 3000 \text{ cm}^{-1}$ . Unfortunately, there is significant VSF intensity of O-H modes within this spectral region. For this reason,  $\text{D}_2\text{O}$  is often preferred to  $\text{H}_2\text{O}$  for VSF studies interested in C-H stretch modes, such as those

employed in Chapters IV and V.<sup>38</sup> Selective deuteration is a powerful tool for vibrational spectroscopies, as it changes resonance frequencies without greatly altering chemical characteristics. The neat  $\text{CCl}_4/\text{D}_2\text{O}$  interface is shown in SSP polarization in Figure 3.3. One can see the main two features from Figure 3.1 – a sharp signal at  $2720\text{ cm}^{-1}$  from the “free OD” stretch and a broad continuum of lower frequency modes – are preserved but redshifted. The spectrum is not taken lower than  $2450\text{ cm}^{-1}$  due to  $\text{CO}_2$  absorption of the IR beam, though the O-D stretching modes continue in this region. Importantly,  $\text{D}_2\text{O}$  does not give VSF signal above  $2750\text{ cm}^{-1}$ , leaving the C-H stretching region uncluttered.

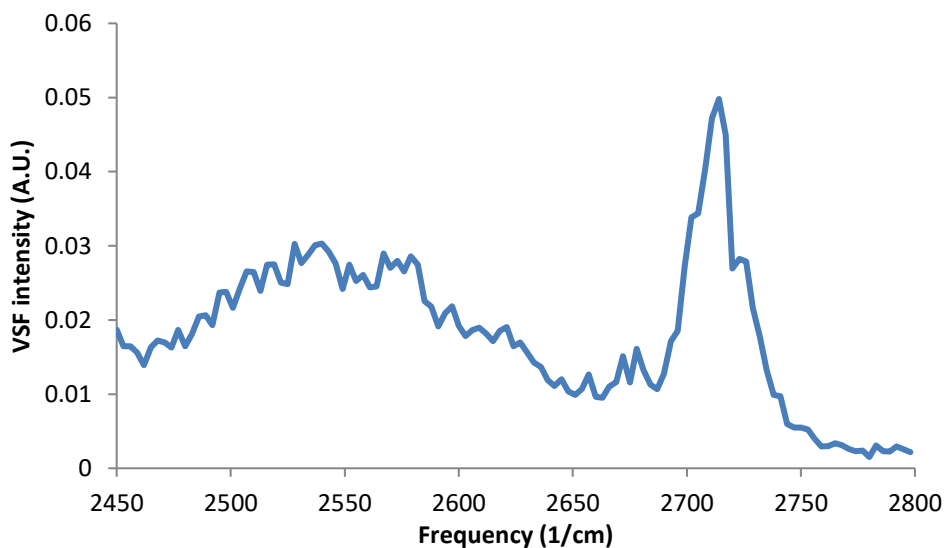


**Figure 3.3.** VSF spectra of the neat  $\text{CCl}_4/\text{D}_2\text{O}$  interface in the O-D stretching region in PPP polarization geometry.

### Surfactant adsorption to the oil/water interface

As mentioned in the introduction, there is a structure-function relationship between interfacial characteristics and the molecules which reside there. Amphiphilic molecules known as surfactants typically have water-soluble “heads” and oil-soluble “tails.” Surfactants are known to spontaneously form a strongly oriented monolayer at air/water,<sup>39</sup> oil/water,<sup>19,40</sup> and hydrophobic solid/water interfaces,<sup>41</sup> where the hydrophilic headgroups face the aqueous phase.<sup>40,42–45</sup> The two surfactants used in this study are dodecyltrimethylammonium bromide (DTAB) and cetrimonium bromide (CTAB); their structures are shown in Figure 3.4. Both share the same cationic quaternary amine

headgroup (thus the headgroup area is the same), but the length of their alkyl tail differs by 4 carbons. This makes CTAB more hydrophobic than DTAB, and consequently more surface active.<sup>45-47</sup> Important physical properties of DTAB and CTAB are given in Table 3.1. At high concentration, known as the critical micelle concentration (*cmc*), surfactants spontaneously assemble into micelles. Micelles are highly charged and thus remain solvated in bulk. A surfactant's aggregation number is the average number of surfactant molecules within each micelle. CTAB has a longer tail, which causes it to form micelles of a greater diameter, and subsequently has a higher aggregation number than DTAB.

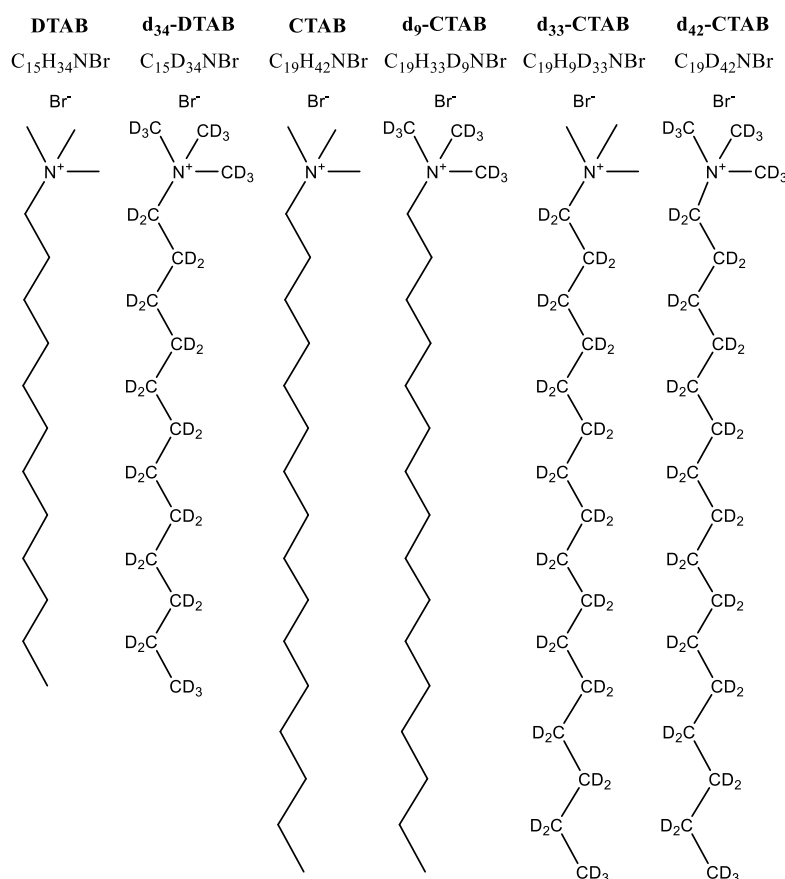


**Figure 3.4.** Molecular structures of DTAB, CTAB, and the deuterated analogues used within this dissertation.

**Table 3.1.** Physical characteristics of DTAB and CTAB.<sup>48</sup>

	DTAB	CTAB
Molecular mass	308.3 g/mol	364.5 g/mol
Critical micelle concentration	14 – 15 mM	0.92 – 1.0 mM
Aggregation number	51	70

As the concentration of a surfactant increases, interfacial adsorption also increases, lowering the system's surface tension as illustrated at the n-octane/H<sub>2</sub>O interface for DTAB and CTAB in Figures 3.5 and 3.6, respectively.\* The curve reaches a minimum at the *cmc* since the surface is saturated with a surfactant monolayer and additional surfactant spontaneously assembles into bulk micelles. The *cmc* for DTAB is higher than that of CTAB.

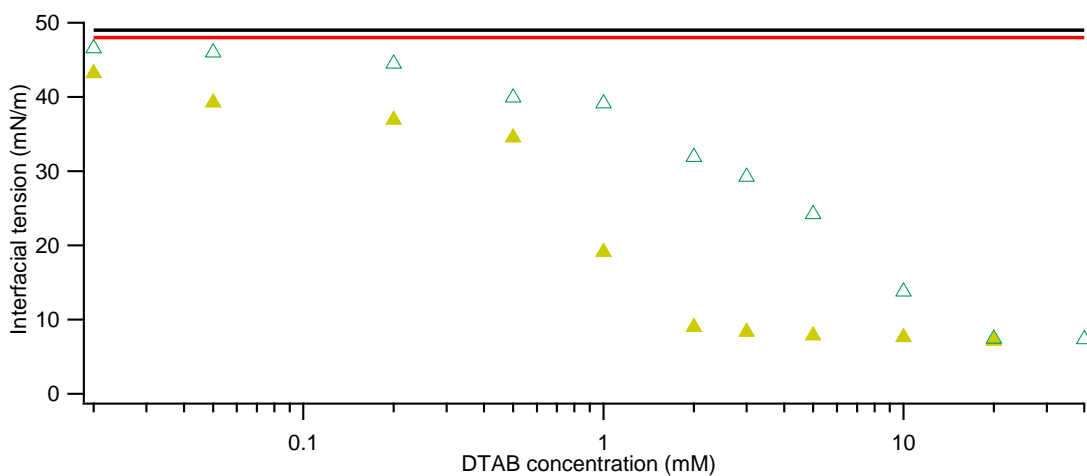


**Figure 3.5.** Dependence of n-octane/H<sub>2</sub>O surface tension on DTAB concentration (open triangles). The dependence is also shown under addition of 2 mM PSS (closed triangles). The black and red lines represent the neat n-octane/water surface tension and surface tension of 2 mM PSS without DTAB, respectively.

This dissertation focuses on the enhanced surface activity of polyelectrolyte/surfactant (P/S) combinations, which will be explored in great depth in Chapters IV and V. The surface tension isotherms shown in Figures 3.5 and 3.6 also include traces for the same surfactant systems under addition of 2.0 mM poly(styrene sulfonate) (PSS). P/S combinations are loosely grouped into two categories.<sup>49,50</sup> Synergic (or “Type 1”) systems lower surface tension below that of the surfactant at the same concentration due to the action of coadsorption. The DTAB/PSS system is one of the best-studied synergic P/S combinations. Anti-synergic (or “Type 2”) systems increase the

---

\* The unbranched alkane oil n-octane was used in the preliminary studies which would eventually become the project detailed in Chapter IV.

surface tension above that of the surfactant under the same concentration, most likely due to high solubility of the resultant P/S complexes, ultimately leading to interfacial

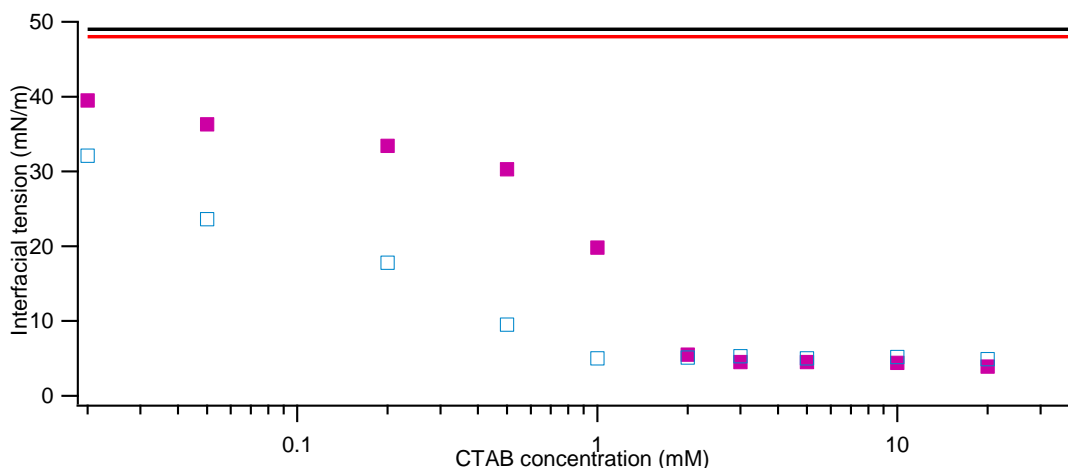


**Figure 3.6.** Dependence of n-octane/H<sub>2</sub>O surface tension on CTAB concentration (open squares). The dependence is also shown under addition of 2 mM PSS (closed squares). The black and red lines represent the neat n-octane/water surface tension and surface tension of 2 mM PSS without CTAB, respectively.

depletion. Curiously, CTAB/PSS is an anti-synergic system (Figure 3.6), even though CTAB is more surface active on its own than DTAB. The underlying reasons for this are not currently known.

Although P/S studies are relatively common, most of these studies characterize the interface over a variety of surfactant concentrations under a fixed amount of polyelectrolyte (e.g., Figures 3.5 and 3.6). However, the surface activity of these systems depends on polyelectrolyte concentration as well, even when the polyelectrolyte is not surface active on its own. This is illustrated in Figure 3.7 for the DTAB/PSS system at the n-octane/H<sub>2</sub>O interface. The differences in surface tension at low, intermediate, and high polyelectrolyte concentration arise from structural changes in the polyelectrolyte layer. This concept will be explored further in Chapter V for the PAA/CTAB system.

### Spectral characteristics of the surfactant interface

Surfactants will spontaneously adsorb to interfaces in an ordered monolayer as shown in the middle panel of Figure 3.2. The resultant VSF spectrum from a 15  $\mu$ M CTAB solution is shown in Figure 3.8a at the CCl<sub>4</sub>/H<sub>2</sub>O and CCl<sub>4</sub>/D<sub>2</sub>O interface. Note that these spectra were not normalized according to the normalization procedure in

Chapter II, as they were taken before such a procedure was developed and implemented. Thus, the low VSF intensity at  $\sim 1500\text{ cm}^{-1}$ ,  $\sim 1800\text{ cm}^{-1}$ ,  $\sim 2000\text{ cm}^{-1}$ , and  $\sim 2300\text{ cm}^{-1}$  are

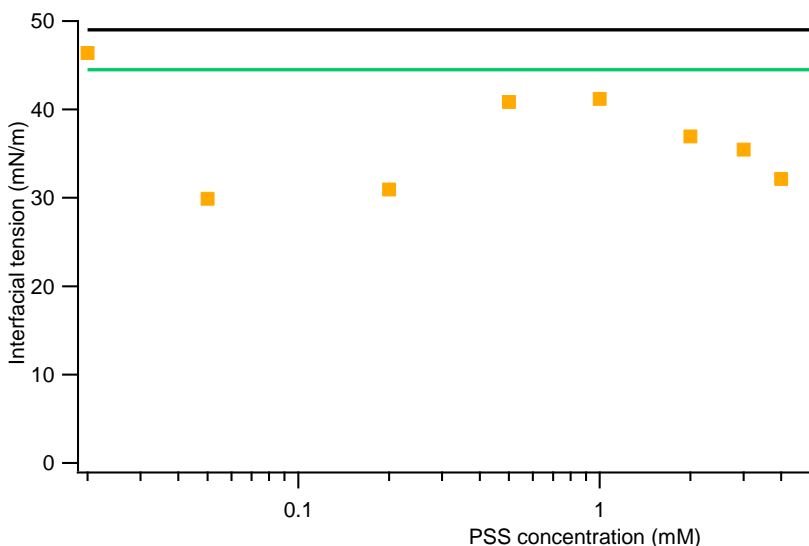


**Figure 3.7.** Dependence of n-octane/H<sub>2</sub>O surface tension on PSS concentration under fixed 0.2 mM DTAB. The black and green lines represent the surface tension of a neat octane/water and 0.2 mM DTAB interface.

artifacts introduced by absorbance of the IR beam. Regardless, the differences between the surfactant interface spectrum and that of the neat CCl<sub>4</sub>/water interface are clear. The  $3665\text{ cm}^{-1}$  free OH and  $2720\text{ cm}^{-1}$  free OD features have disappeared. This is because CTAB has covered the interface, and there are no bare areas within which an uncoupled OH (or OD) oscillator could protrude (see middle panel of Figure 3.2). Due to water's dipolar nature, a charged adsorbate has the greatest ability to enhance water's orientation. An interfacial electric field extends into the water phase on the order of the system's Debye length.<sup>51,52</sup> This increases the net orientation of VSF-active O-H oscillators, leading to a gigantic enhancement of VSF signal from coordinated water below  $3600\text{ cm}^{-1}$  in H<sub>2</sub>O (below  $2700\text{ cm}^{-1}$  in D<sub>2</sub>O) which dominate Figure 3.8a. The increase in overall orientation facilitates hydrogen bonding within interfacial water which increases coupling between clusters of water molecules.<sup>53</sup> Spectrally, this manifests as a broadening of the coordinated water signal which extends into very low frequencies.<sup>54-57</sup> Electrostatic screening of the interfacial charge can decrease the Debye length, as represented in the rightmost panel of Figure 3.2. Likewise, there is a decrease the VSF signal from coordinated water at high salt concentration, shown in Figure 3.9.

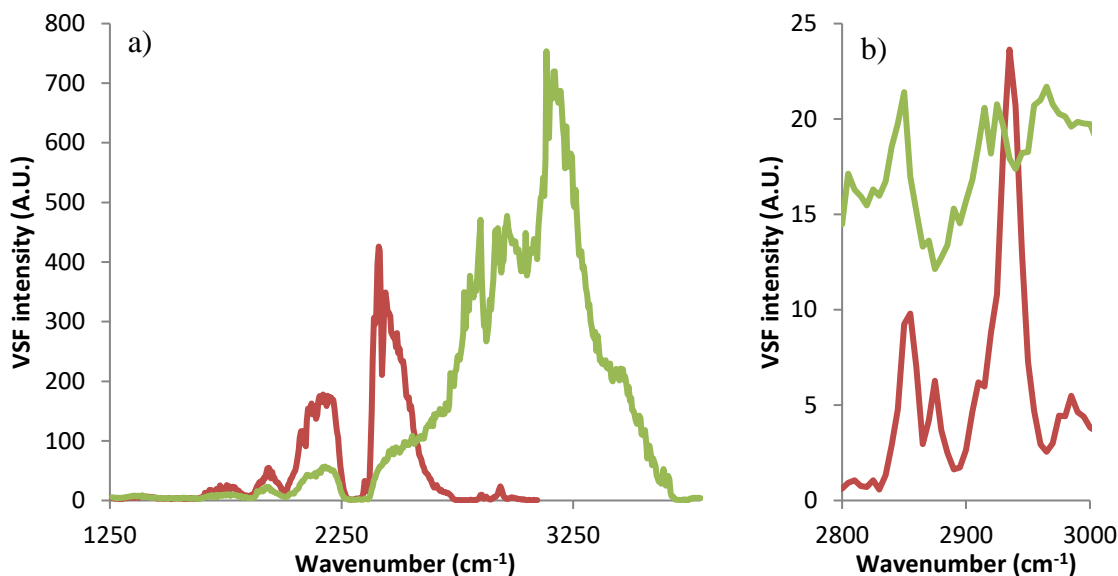


**Figure 3.8.** a) VSF spectra in the SSP polarization geometry of 15  $\mu\text{M}$  CTAB at the  $\text{CCl}_4/\text{H}_2\text{O}$  interface (green) and the  $\text{CCl}_4/\text{D}_2\text{O}$  interface (red). b) The same spectra, but zoomed in on the C-H region of 2800 – 3000  $\text{cm}^{-1}$ . In b) the green trace has been scaled by 0.05 due to its greatly higher intensity. These spectra were not normalized (see text).

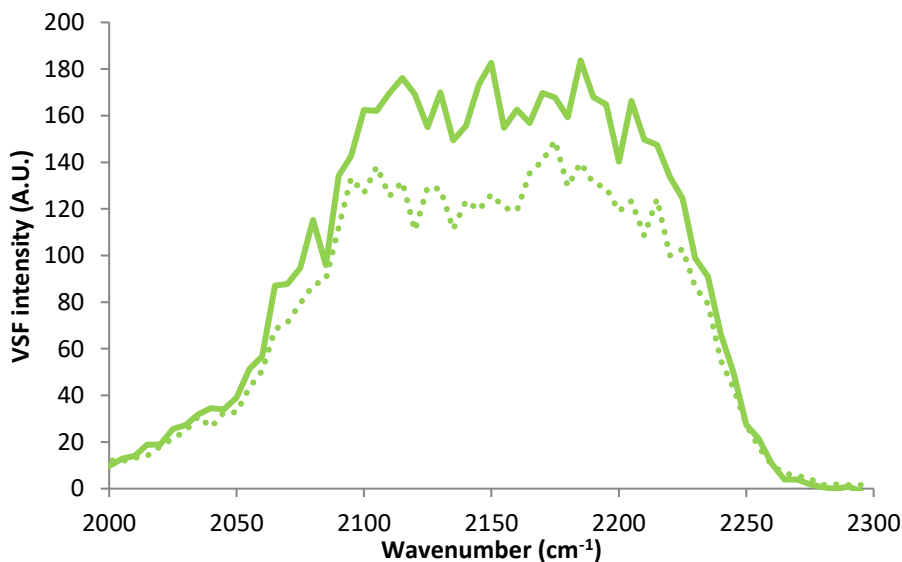


**Figure 3.9.** VSF spectra in the SSP polarization geometry of 15  $\mu\text{M}$  CTAB at the  $\text{CCl}_4/\text{H}_2\text{O}$  interface (solid line) and with added 2 mM NaCl (dotted line).

Surfactants like CTAB characteristically adsorb to the interface as a monolayer, which imparts a net orientation and leads to strong VSF signal. Figure 3.8b focuses on the C-H stretch of the 15  $\mu\text{M}$  CTAB spectra shown in  $\text{D}_2\text{O}$  and  $\text{H}_2\text{O}$ . When  $\text{D}_2\text{O}$  is used (red trace), there are no O-D stretch vibrations in this region of the spectrum and the C-H

stretch peaks of CTAB are easily visible. More precise spectra are explored in later chapters, but at this resolution one can discern the CH<sub>2</sub> symmetric stretch (~2850 cm<sup>-1</sup>), the CH<sub>3</sub> symmetric stretch (~2875 cm<sup>-1</sup>), the methylene Fermi resonance (~2914 cm<sup>-1</sup>) and the methyl Fermi resonance (~2940 cm<sup>-1</sup>). The green trace was taken in H<sub>2</sub>O where this region of the spectrum is overwhelmed by coordinated O-H signal. However, note that there are spectral features caused from constructive and destructive interferences between C-H modes and O-H modes. Two destructive interferences are observable as dips in VSF signal at 2875 cm<sup>-1</sup> and 2940 cm<sup>-1</sup>. In later chapters, interference between O-D and C-D modes will be used to determine the sign of the interfacial charge.

This dissertation studies mixtures of organic molecules as they adsorb to the oil/water interface. When two adsorbed molecules share similar vibrational signatures, they can both contribute to VSF amplitude at those shared frequencies, which makes spectral interpretation difficult. To deconvolute contributions from polymer and the surfactant C-H modes, deuterated d-DTAB and deuterated d-CTAB are preferred for the studies in this dissertation. The C-D stretch modes appear between 2000 – 2250 cm<sup>-1</sup> although this region often exhibits a high intensity of coordinated O-D or O-H signal, as shown in Figure 3.9. Like the C-H modes shown in Figure 3.8b, assignment of C-D peaks is difficult when significant overlapping bands contribute. A neutrally charged interface gives the lowest level of coordinated water signal (in later chapters the amplitude of the coordinated water signal is used to estimate the magnitude of interfacial charge). In Figure 3.10, coadsorption of cationic CTAB with anionic PAA results in a very low interfacial charge, which lowers the coordinated O-D signal such that C-D modes are clearly visible. The peak at ~2060 cm<sup>-1</sup> is assigned to the CD<sub>3</sub> symmetric stretch, the peak at ~2105 cm<sup>-1</sup> is assigned to the CD<sub>2</sub> symmetric stretch, the shoulder at ~2130 cm<sup>-1</sup> is assigned to the CD<sub>3</sub> Fermi resonance, the peak at ~2180 cm<sup>-1</sup> is assigned to the CD<sub>2</sub> Fermi resonance, and the peak at ~2220 cm<sup>-1</sup> is assigned to the CD<sub>3</sub> asymmetric stretch. In comparison, the undeuterated trace does not exhibit these modes, and instead shows a broad continuum of signal from low-frequency coordinated D<sub>2</sub>O vibrations.

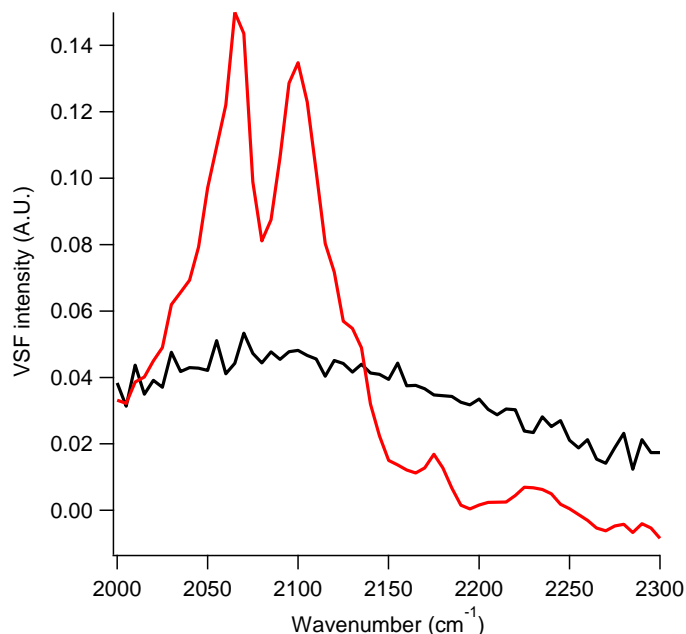


**Figure 3.10.** VSF spectra in the SSP polarization geometry of 15  $\mu\text{M}$  CTAB and 1 ppm PAA at the  $\text{CCl}_4/\text{H}_2\text{O}$  interface in the C-D stretch region. The black trace is undeuterated CTAB and the red trace is fully deuterated  $\text{d}_{42}$ -CTAB.

### Conclusions

This chapter acts as a tutorial to detail VSF spectra of simple interfaces. First, the neat  $\text{CCl}_4/\text{H}_2\text{O}$  and  $\text{CCl}_4/\text{D}_2\text{O}$  interfaces are shown to exhibit signal from two main types of interfacial water, one of which is aligned by participating in many hydrogen bonds, the other of which straddles the interfacial plane. The adsorption of a surfactant is shown to increase the former and decrease the latter type of interfacial water. VSF results are corroborated with oil/water tensiometry, where major trends of the surface tension isotherm are explained. It is shown how selective deuteration aids in the deconvolution of overlapping vibrational bands, specifically through the use of  $\text{D}_2\text{O}$  and a deuterated surfactant. This chapter introduces the practicalities of VSF spectroscopy, which is thoroughly employed for the DTAB/PSS interface in Chapter IV and the CTAB/PAA interface in Chapter V.

## CHAPTER IV

### STRUCTURAL DETAILS OF DTAB-INDUCED ADSORPTION AND DESORPTION OF A POLYELECTROLYTE/SURFACTANT LAYER AT THE OIL/WATER INTERFACE

The simple modification of air/water and oil/water through surfactant adsorption has long been exploited for industrial use, and the behavior of these surfactants is noteworthy in biological systems and environmental science. The addition of polyelectrolytes to a surfactant solution often results in coadsorption of both components, which has been proposed as a route to tailor interfaces for specific interactions as explained in Chapter I. The combination of sodium poly(styrene sulfonate) (PSS) and dodecyltrimethylammonium bromide (DTAB) is one of the best studied polymer/surfactant (P/S) combinations, due to the strong enhancement of interfacial activity compared to either component on its own. However, these studies are mostly limited to the air/water interface, and commonly the techniques used cannot differentiate the contribution of both components. It has been proposed in literature that within certain concentration ranges of this system, adsorption of one or more polymer layers occurs, though this has only been measured indirectly and never at oil/water interfaces. Many of the proposed applications of multilayer systems, such as emulsion stabilization and targeted drug deliver, take place at the oil/water interface. This chapter characterizes the coadsorption of PSS and DTAB to the oil/water interface with the specific aim of determining whether a secondary layer of PSS adsorbs. The technique of vibrational sum frequency (VSF) spectroscopy – along with selective deuteration – is employed to directly observe oriented vibrational modes of PSS. Ultimately, it was found that a secondary PSS layer does not adsorb at any DTAB concentration and no PSS adsorbs at a concentration above the system critical micelle concentration (*cmc*), in contrast to the aforementioned air/water studies. This work is in press as Schabes, B. K.; Hopkins, E. J.; and Richmond, G. L. **Molecular Interactions Leading to the Coadsorption of Surfactant Dodecyltrimethylammonium Bromide and Poly(Styrene Sulfonate) at the Oil/Water Interface.** *Langmuir*, 2019. DOI: [10.1021/acs.langmuir.9b00873](https://doi.org/10.1021/acs.langmuir.9b00873).<sup>58</sup> I

designed the study, did all the writing, and performed all experiments except for the zeta potential, dynamic light scattering, and UV/Vis absorption data, which were performed by undergraduate researcher Emma J. Hopkins.

## Introduction

Combinations of ionic surfactants with oppositely charged polyelectrolytes (PE) have seen many industrial applications due to their enhanced coadsorption at air/water and oil/water interfaces.<sup>3,49,50,59–64</sup> Given the breadth of available PE and surfactant chemistries their combinations lead to an equally large variety of tunable interfacial features including thickness, hydrophobicity, viscosity and other rheological properties.<sup>65</sup> However some applications require the specific interfacial control provided by the formation of P/S multilayers. For example, polymer layers can be applied to encapsulate oil-in-water emulsions, rendering them more chemically and physically stable.<sup>3</sup> These physicochemical modifications have been employed in the targeted delivery of lipophilic drugs solubilized in oil-core nanoemulsions.<sup>3,8,66,67</sup> A better understanding of P/S multilayer formation and adsorbate structure at the oil/water interface would allow more efficient development of medicine-containing emulsions which reach their targets effectively and exhibit few biochemical side-effects.

This chapter details the coadsorption of ionic surfactant DTAB and anionic polymer PSS at the oil/water interface. This combination is one of the most widely studied P/S systems at the air/water interface, and acts as a model for strongly interacting P/S combinations.<sup>68–71</sup> It is known that when the charge ratio of bulk P/S complexes nears unity, low-charge complexes coalesce and precipitate in what is referred to as the “two-phase” region.<sup>65,72,73</sup> At sufficiently high surfactant concentration P/S complexes are charged enough that precipitation does not occur and the system resorts back to “one-phase” behavior. Furthermore, it has been found previously that extreme concentration gradients during mixing – such as those created when a small volume of concentrated surfactant is added to a dilute mixture of PE – can lead to “kinetically trapped” P/S aggregates with long lifetimes.<sup>27–30</sup>

While there is general agreement that both DTAB and PSS coadsorb as a mixed monolayer at low DTAB concentrations,<sup>27,74–77</sup> the adsorption behavior of DTAB/PSS

within and above the two-phase region is under renewed scrutiny due to disagreements in adsorbate amount. Taylor's neutron reflectivity studies identified a 24 Å P/S monolayer at low DTAB concentration.<sup>77,78</sup> As the concentration was raised into the two-phase region the layer was found to thicken in ~20 Å steps, consistent with the formation of multiple interfacial layers, and this behavior continued well above the *cmc*. Taylor notes that neutron reflectivity is not sensitive enough to distinguish the structure of the P/S sublayer. He proposes either a PE strand sandwiched between a disordered surfactant bilayer, or "pearls" of surfactant micelles decorating a PE "string."<sup>77</sup> In the same system recent studies by Campbell *et al.* showed a gradual increase in surface tension in the two-phase region consistent with slow interfacial desorption of PSS.<sup>68,79</sup> Furthermore, a robust model based on mass action predicts complete depletion of interfacial PSS at a DTAB concentration above the *cmc*.<sup>71</sup> Given the differing interpretations of DTAB/PSS behavior at the air/water interface it is all the more important to explore this system at the oil/water interface. Although many techniques such as neutron reflectivity, ellipsometry, and Brewster's angle microscopy have been used to characterize P/S adsorption, they have difficulty decoupling contributions from multiple interfacial chemicals. As such, the current understanding of multilayer P/S adsorption at the molecular level has advanced little since Taylor *et al.* proposed possible sublayer structures in 2002.<sup>77</sup> While there is general agreement that the first PE layer adsorbs to the charged headgroups of a surfactant monolayer, the structure of the secondary layer remains largely unresolved. Knowledge of P/S structure at the oil/water interface is even sparser and has mainly been studied by interfacial tensiometry alone. To my knowledge there has been no attempt to detect the adsorption of multiple P/S layers at the planar oil/water interface.

In this chapter, VSF spectroscopy is used to non-invasively detect PSS's vibrational fingerprint and interfacial orientation to build a molecular picture of the interfacial P/S structure. This technique has been used extensively to study both polymer and surfactant interfacial adsorption.<sup>80-84</sup> However the application of VSF spectroscopy to P/S air/water interfaces is rare,<sup>85,86</sup> and similar studies at the oil/water interface are even more limited.<sup>87</sup>

The specific aim of the work described herein is to determine the structure of PSS involved in any interfacial multilayers. The molecular behavior of DTAB/PSS is largely

unknown at the oil/water interface. As mentioned above there is general agreement that a mixed P/S monolayer adsorbs at low DTAB concentration; the VSF response at this low DTAB concentration will be compared with spectra at higher concentrations, where any increases in layer thickness due to multilayer adsorption will manifest as changes to the intensity of the PSS signal. VSF spectroscopy is well suited to study this system, as analogues of Taylor's proposed sublayer structures have been previously characterized by the technique (e.g., symmetric lipid bilayers,<sup>88-90</sup> close-packed hexagonal liquid crystals,<sup>91</sup> and PE multilayers<sup>92</sup>). Within this study an established mixing procedure is followed to minimize the formation of these kinetically trapped aggregates, and the mixed systems are allowed at least 16 hours to reach a steady state before spectral measurements are performed. Along with VSF spectroscopy, this study uses zeta potential (ZP) measurements and interfacial tensiometry to relate spectroscopic changes to macroscopic trends, such as the inversion of P/S complex charge. This study lays the groundwork for examining P/S adsorption at the oil/water interface and calls into question current models of P/S layering behavior.

### Sample preparation

All chemicals were purchased in the highest purity available and were not purified further, with the exception of carbon tetrachloride (HPLC grade, 99.9%), which was doubly distilled before use. Sodium poly(styrene sulfonate) (PSS) was obtained from Sigma-Aldrich with average molecular weight of 70 kDa (Batch # 12105EJ). Dodecyltrimethylammonium bromide (DTAB) was purchased from Acros Organics at 99% purity. Deuterium oxide (99.9% D) was supplied by Cambridge Isotope Laboratories, Inc. and fully deuterated d<sub>34</sub>-DTAB (98.8% D) was obtained through CDN Isotopes. Chemical structures of PSS and DTAB are given in Figure 4.1.

For this study PSS concentration is fixed at 0.10 mM. Note that the PSS concentration is given with respect to the styrene sulfonate monomer. The concentration of DTAB varies between 0.03 mM and 15 mM. In the absence of polymer DTAB's *cmc* is 15 mM, but when mixed with 0.10 mM PSS, the PE induces micellation at a lower DTAB concentration, and the DTAB/PSS system has a *cmc* of 13 mM.<sup>77</sup> To avoid the formation of kinetically trapped P/S aggregates a careful mixing procedure is employed

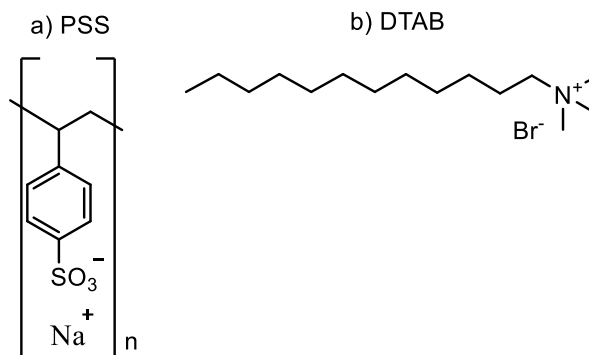


**Figure 4.1.** Molecular structures of a) sodium poly(styrene sulfonate) and b) dodecyltrimethylammonium bromide.

whereby equal volumes of PSS and DTAB are prepared alone then combined and swirled vigorously for 30 seconds before studies are performed. For VSF experiments ~10 mL of the mixed P/S solution is carefully deposited into the sample cell onto a layer of CCl<sub>4</sub> with a 5 mL adjustable pipette. The total surface area of the aqueous layer is ~36 cm<sup>2</sup>. The interface was allowed to equilibrate for at least 16 hours before spectra were taken.

When the DTAB/PSS complexes formed in bulk contain a low charge they will coalesce, which causes an increase in the size of the complexes,<sup>68,79</sup> as in other P/S systems.<sup>50</sup> If the diameter of the complexes is on the order of the wavelength of visible light the complexes will scatter the visible light and the solution will appear cloudy with precipitate. To quantify the degree of precipitation the solution UV/Vis absorbance at 450 nm was measured on a Perkin Elmer Lambda-1050 UV/Vis/NIR spectrophotometer. Because neither PSS nor DTAB has a chemical absorbance at this wavelength any increase in absorbance above that of water is due to scattering from large complexes suspended in the bulk.

### **DTAB induces adsorption of PSS**

The interaction of DTAB with PSS as investigated through various macroscopic measurements is reported in Figure 4.2 as a function of DTAB concentration. Figure 4.2a shows the CCl<sub>4</sub>/H<sub>2</sub>O surface pressure after 11 hours as a function of DTAB concentration. Data are shown with and without added 0.10 mM PSS. The surface pressure of 0.10 mM PSS (not shown) does not differ from that of the neat CCl<sub>4</sub>/H<sub>2</sub>O interface, confirming that PSS at this concentration is not surface active by itself. The

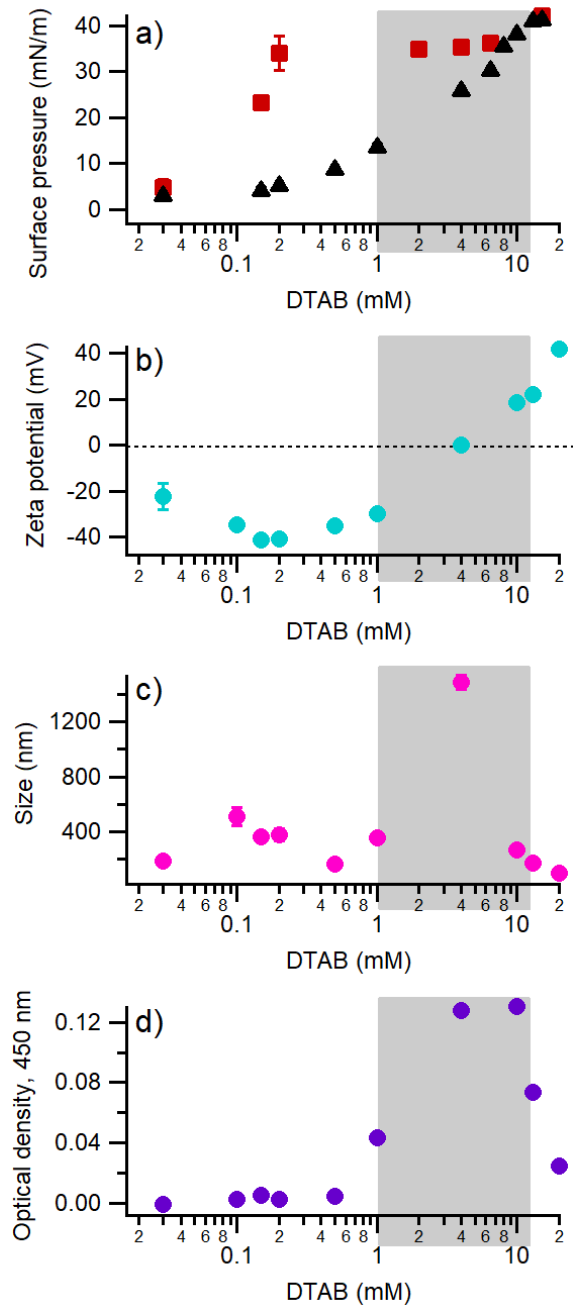


**Figure 4.2.** (a)  $\text{CCl}_4/\text{H}_2\text{O}$  surface pressure isotherm, (b) bulk zeta potential, (c) dynamic light scattering size, and (d) optical density at 450 nm for 0.10 mM PSS with variable DTAB concentration given on the bottom axis. In (a), the surface pressure of DTAB (black triangles) is shown alongside that of the DTAB/PSS system (red squares). The shaded area marks the “two-phase” region where DTAB/PSS mixtures precipitate. Error bars in a-c represent the standard deviation of averaged values.

surface pressure of DTAB solutions increases with DTAB concentration up to the *cmc* (Figure 4.2a, black triangles). In the presence of PSS, surface pressure increases steeply with DTAB concentration until 0.20 mM DTAB at which point the surface pressure reaches a plateau (Figure 4.2a, red squares), in accordance with many prior DTAB/PSS studies at the air/water interface.<sup>77,78,93-95</sup> Thus, the surface pressure of 6.5 mM DTAB/PSS is similar to that of 0.20 mM DTAB/PSS. The surface pressure for 15 mM DTAB is the same regardless of PSS addition.

ZP measurements of the dispersed P/S complex shear plane potential are shown in Figure 4.2b as a function of DTAB concentration. These complexes are negative below 4 mM DTAB, neutral at 4 mM and positively charged above 4 mM. The association in bulk between DTAB and PSS is evidenced by the dependence of P/S complex charge on DTAB concentration. The size of bulk complexes as measured with DLS are shown in Figure 4.2c. An increase in complex size is seen at 4 mM which coincides with the formation of neutral P/S complexes in bulk. Sufficiently low-charged P/S complexes are known to coalesce and precipitate which gives the solutions a cloudy appearance.<sup>72</sup> Optical density at 450 nm, shown in Figure 4.2d, is significantly raised above the baseline between 1 and 13 mM DTAB. This is known as the two-phase region and is represented by the grey boxes in Figure 4.2.

The aim of this study is to compare monolayer P/S adsorption at low DTAB concentration with possible multilayer adsorption at two higher DTAB concentrations. Figure 4.3 compares the time dependence of surface pressure data for these three DTAB concentrations in the absence (Figure 4.3a) and presence (Figure 4.3b) of PSS. Corresponding spectroscopic behavior is analyzed later with VSF spectroscopy. The surface pressure of DTAB in the absence of PSS shows little time dependence and stabilizes within two minutes for all concentrations. When mixed with 0.10 mM PSS (Figure 4.3b) the surface pressure curves of 0.20 mM (orange circles) and 6.5 mM DTAB (green triangles) display a gradual increase over ~8 hours before stabilizing, indicating PSS affects not only the final surface pressure but the time dependence as well. The 0.20 mM DTAB/PSS mixture shows a large enhancement in surface pressure compared to the trace without PSS, while the 6.5 mM DTAB/PSS mixture shows a moderate enhancement in surface pressure compared to the trace without PSS. The 15 mM

DTAB/PSS mixture shows the same time dependence and levels off at the same value as the solution without added polymer.

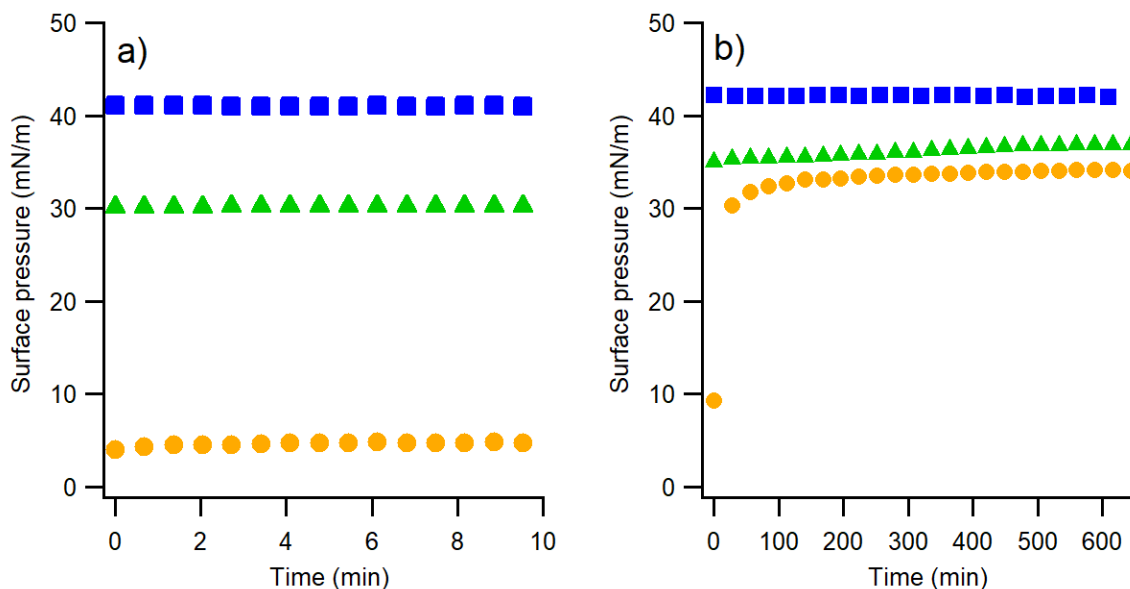


**Figure 4.3.** Dynamic  $\text{CCl}_4/\text{H}_2\text{O}$  surface pressure data for DTAB concentrations of 0.20 mM (orange circles), 6.5 mM (green triangles), and 15 mM DTAB (blue squares). (a) DTAB alone; (b) DTAB with 0.10 mM PSS. Further changes in surface pressure were not observed beyond the timescales reported here.

VSF spectroscopy is used to determine the presence and orientation of DTAB,  $\text{D}_2\text{O}$  and PSS at the  $\text{CCl}_4/\text{D}_2\text{O}$  interface. The VSF spectrum of 0.10 mM PSS (not shown) does not differ from that of the neat  $\text{CCl}_4/\text{D}_2\text{O}$  interface, confirming that PSS is not surface active by itself. After interface formation within the VSF sample cell, the DTAB/PSS system sat undisturbed for 16 hours before acquisition of spectral data. All spectra shown are taken with fixed 0.10 mM PSS and variable 0.20 mM, 6.5 mM, or 15 mM DTAB unless otherwise noted. Figure 4.4 shows the VSF response of h-DTAB/PSS at the  $\text{CCl}_4/\text{D}_2\text{O}$  interface in the O-D (Figure 4.4a) and C-H (Figure 4.4b) stretching regions. In Figure 4.4a the broad envelope of O-D stretching signal is highest for 15 mM DTAB/PSS (blue squares), intermediate for 0.20 mM DTAB/PSS (yellow circles) and lowest for 6.5 mM DTAB/PSS (green triangles). When next to a charged interface, water molecules will orient their dipole in response to the interfacial electric field, whereupon their stretching vibrations give enhanced VSF signal in response to the degree of charge.<sup>54–56,96,97</sup> There is also a known contribution on the VSF signal from a

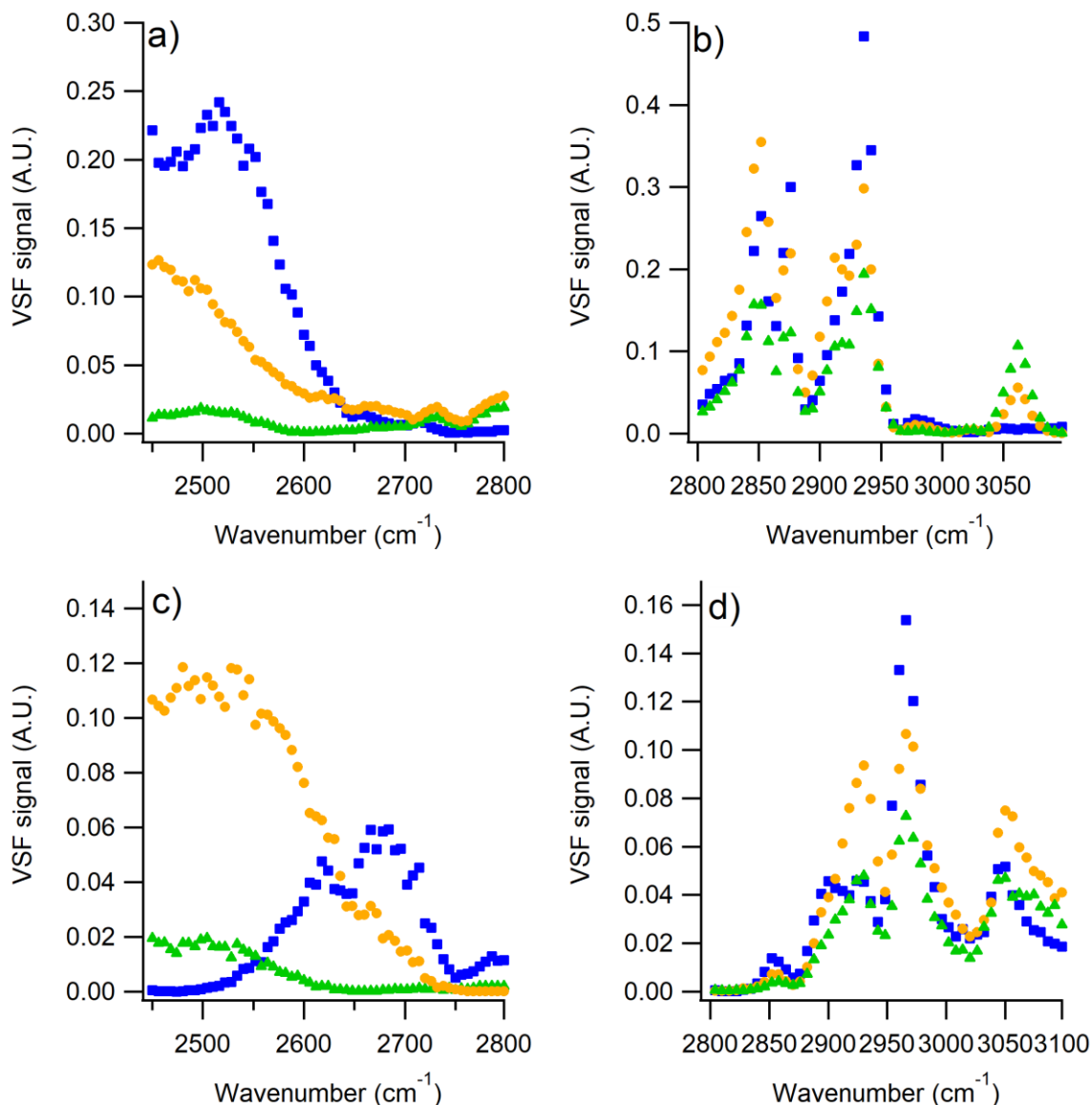


**Figure 4.4.** VSF spectra of h-DTAB/PSS at the  $\text{CCl}_4/\text{D}_2\text{O}$  interface in the (a & c) O-D stretching and (b & d) C-H stretching regions. Spectra are shown in SSP (a & b) and SPS (c & d) polarization geometries. The PSS concentration is fixed at 0.10 mM, while the h-DTAB concentration is 0.20 mM (yellow circles), 6.5 mM (green triangles), or 15 mM (blue squares).

mixing of the higher-order  $\chi^{(3)}$  with the detected VSF signal at high interfacial potentials.<sup>51,98</sup> The effect of the  $\chi^{(3)}$  contribution on the VSF spectrum of water was shown in recent publications by Ohno *et al.* to be most pronounced for frequencies between 3000 – 3200  $\text{cm}^{-1}$ .<sup>52,88</sup> In  $\text{D}_2\text{O}$  this would correspond to the region between ~2200 – 2370  $\text{cm}^{-1}$ .<sup>57</sup> Thus I believe that it is acceptable to use the intensity of  $\text{D}_2\text{O}$  signal from

2500 – 2650  $\text{cm}^{-1}$  to approximate the magnitude of the interfacial charge, and it is concluded from Figure 4.4a that 0.2 mM and 15 mM DTAB/PSS have a relatively high interfacial charge, while the 6.5 mM DTAB/PSS system has a low interfacial charge.

In Figure 4.4b a number of peaks arise from methyl, methylene, and phenyl C-H moieties. Distinguishing each C-H vibrational contribution is challenging as both PSS and h-DTAB contain methylene groups and exhibit many overlapping bands. For this reason, these spectra were not fit. Nevertheless, the signal at 2875  $\text{cm}^{-1}$  from the terminal  $\text{CH}_3$  groups is unique to h-DTAB and indicates that the methyl mode of interfacial DTAB has a net orientation perpendicular to the interface throughout the concentration series. Signal above 3000  $\text{cm}^{-1}$  comes from phenyl C-H modes unique to PSS.<sup>85,99</sup> The signal from the C-H phenyl groups is only seen for the 0.20 mM and the 6.5 mM DTAB/PSS systems, providing further evidence that PSS and DTAB coadsorb at these concentrations. Recall that the surface pressure of 15 mM DTAB is the same in the absence and presence of PSS (Figure 4.3). This observation along with the lack of intensity from the C-H phenyl modes and high interfacial charge for 15 mM PSS/DTAB in Figure 4.4a leads to the conclusion that PSS does not adsorb at 15 mM DTAB. This will be discussed further in the next section.

### **No PSS adsorbs above the system critical micelle concentration**

Figure 4.5 compares the VSF response of 15 mM h-DTAB with and without 0.10 mM PSS in the O-D and C-H stretching regions. Peak fitting parameters and assignments are given in Appendix A, Table A.1. Within experimental error the traces are identical. Prior studies predict the exclusion of interfacial PE at high surfactant concentration, but those concentrations are higher than the *cmc*.<sup>76,94,100,101</sup> At these same concentrations neutron reflectivity studies by Taylor *et al.* saw formation of a 47 Å “bilayer” of mixed DTAB and PSS at the air/water interface.<sup>78</sup> It is possible that a PE layer forms at the surface but is undetected by VSF spectroscopy due to a random or centrosymmetric net orientation. Furthermore, given the similarity between the two spectra of Figure 4.5, a hypothetical secondary layer would not affect the ordering of the DTAB monolayer nor bring additional ordered DTAB to the interface. I find this unlikely. Since 15 mM DTAB has nearly identical surface pressure (Figure 4.3) and

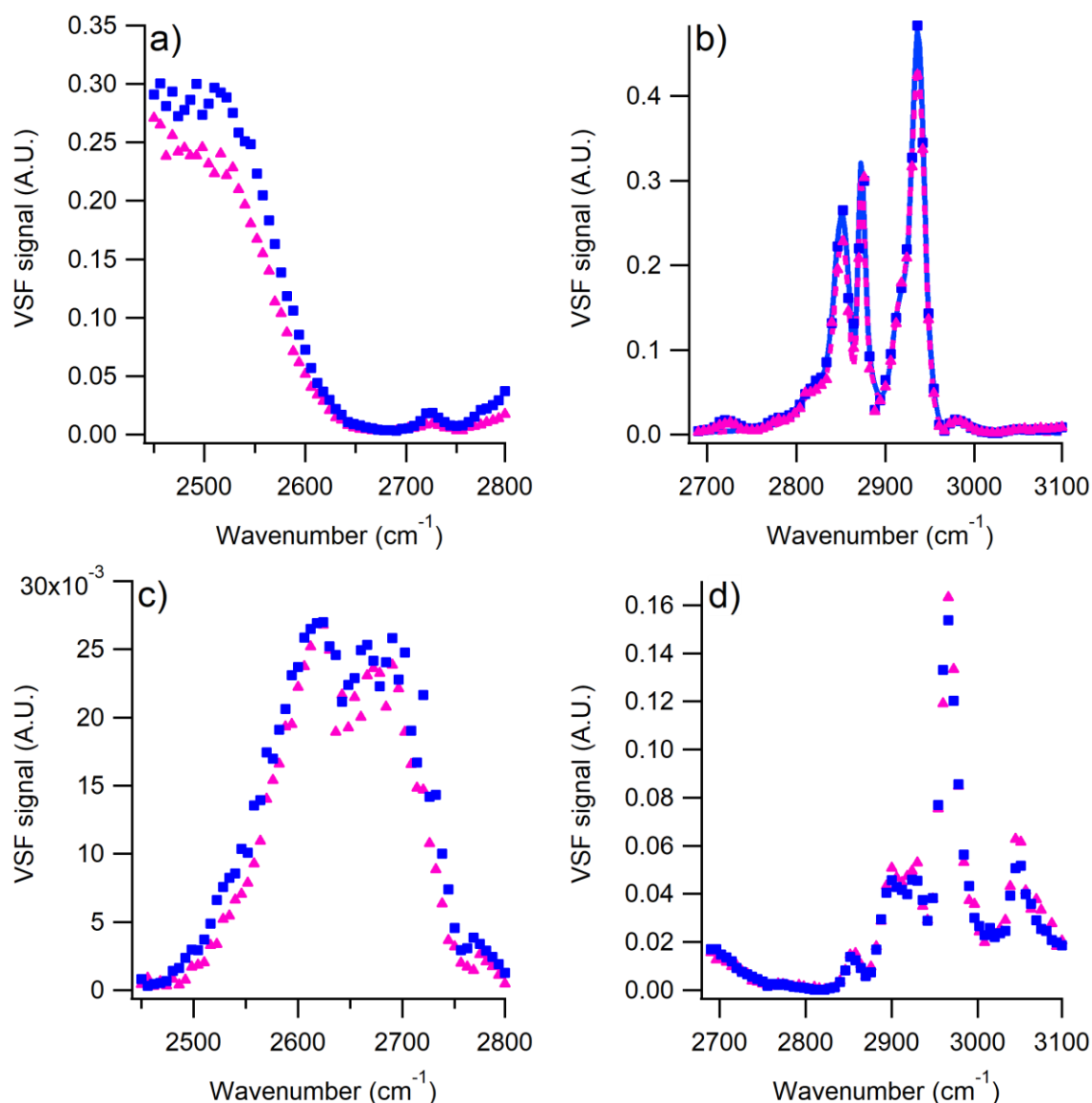


**Figure 4.5.** VSF spectra of 15 mM h-DTAB at the  $\text{CCl}_4/\text{D}_2\text{O}$  interface in the (a & c) O-D stretching and (b & d) C-H stretching regions without PSS (pink triangles) and with 0.10 mM PSS (blue squares). Spectra are shown in SSP (a & b) and SPS (c & d) polarization geometries. Lines are fits to the data (see Table A.1).

surface charge (as measured by O-D stretching signal in Figure 4.5a) regardless of 0.10 mM PSS addition, it is concluded that no PSS adsorption occurs when mixed with 15 mM DTAB. The structure of P/S complexes in bulk is understood to be a surfactant micelle encapsulated by PE.<sup>62,73</sup> It has been proposed by Bell *et al.* that PE uptake in solvated PE-micelle complexes competes with air/water PE adsorption in surface-active P/S complexes.<sup>102</sup> These results are consistent with this model, namely that the existence

of bulk DTAB micelles above the *cmc* would favor the formation of soluble PE-micelle complexes and prevent PSS adsorption.

### **Interfacial charge reversal within the two-phase region**

To better analyze PSS adsorption below the *cmc*, deuterated d-DTAB is used. C-D stretching vibrations are redshifted  $\sim 800\text{ cm}^{-1}$  from their hydrogenated counterparts.<sup>38</sup> Figure 4.6 shows the VSF response of d-DTAB/PSS in the C-D (Figures 4.6a and 4.6c) and C-H (Figures 4.6b and 4.6d) stretching regions. Five C-D modes are detected at all three d-DTAB concentrations in SSP (Figure 4.6a, see Table A.2 for peak fitting parameters and assignments). In this region spectral interference between the surfactant and D<sub>2</sub>O vibrational modes can be used to determine changes in the sign of the interfacial charge.<sup>85,87,103</sup> Close inspection of the  $2180\text{ cm}^{-1}$  CD<sub>3</sub> headgroup peak of Figure 4.6a shows that at 0.20 mM d-DTAB/PSS this mode *constructively* interferes with background O-D stretching modes, but the same mode *destructively* interferes at higher d-DTAB concentrations. I conclude that 0.2 mM DTAB/PSS has a significant negative interfacial charge, as opposed to the strong positive interfacial charge at 15 mM DTAB/PSS (blue squares). While the 6.5 mM DTAB/PSS (green triangles) interface also exhibits a destructive interference at  $2180\text{ cm}^{-1}$  indicative of a positive interfacial charge, the O-D signal for 6.5 mM is significantly lower than that of the other concentrations (Figure 4.4a). It is concluded that the interfacial charge at 6.5 mM DTAB/PSS is weakly positive, consistent with bulk ZP measurements showing a charge inversion point at 4 mM (Figure 4.2b). The fact that the sign and magnitude of the interfacial charge track closely with the bulk ZP measurements implies that the surface and bulk complexes below the *cmc* contain similar P/S ratios, an observation seen in prior P/S studies,<sup>79,86</sup> including one on the similar CTAB/PSS interface.<sup>85</sup>

Figure 4.6b shows the VSF response of d-DTAB/PSS in the C-H stretching region for the SSP polarization geometry. The use of deuterated d-DTAB means that all C-H signal arises from PSS. The traces for 0.20 mM and 6.5 mM d-DTAB/PSS give similar signal from  $2800 - 2950\text{ cm}^{-1}$  which corresponds to PSS backbone CH<sub>2</sub> modes.<sup>87,99</sup> However 6.5 mM d-DTAB/PSS has greater signal above  $3000\text{ cm}^{-1}$  which is assigned to phenyl ring C-H stretches.<sup>85,99</sup> At 15 mM d-DTAB/PSS a weak featureless spectral

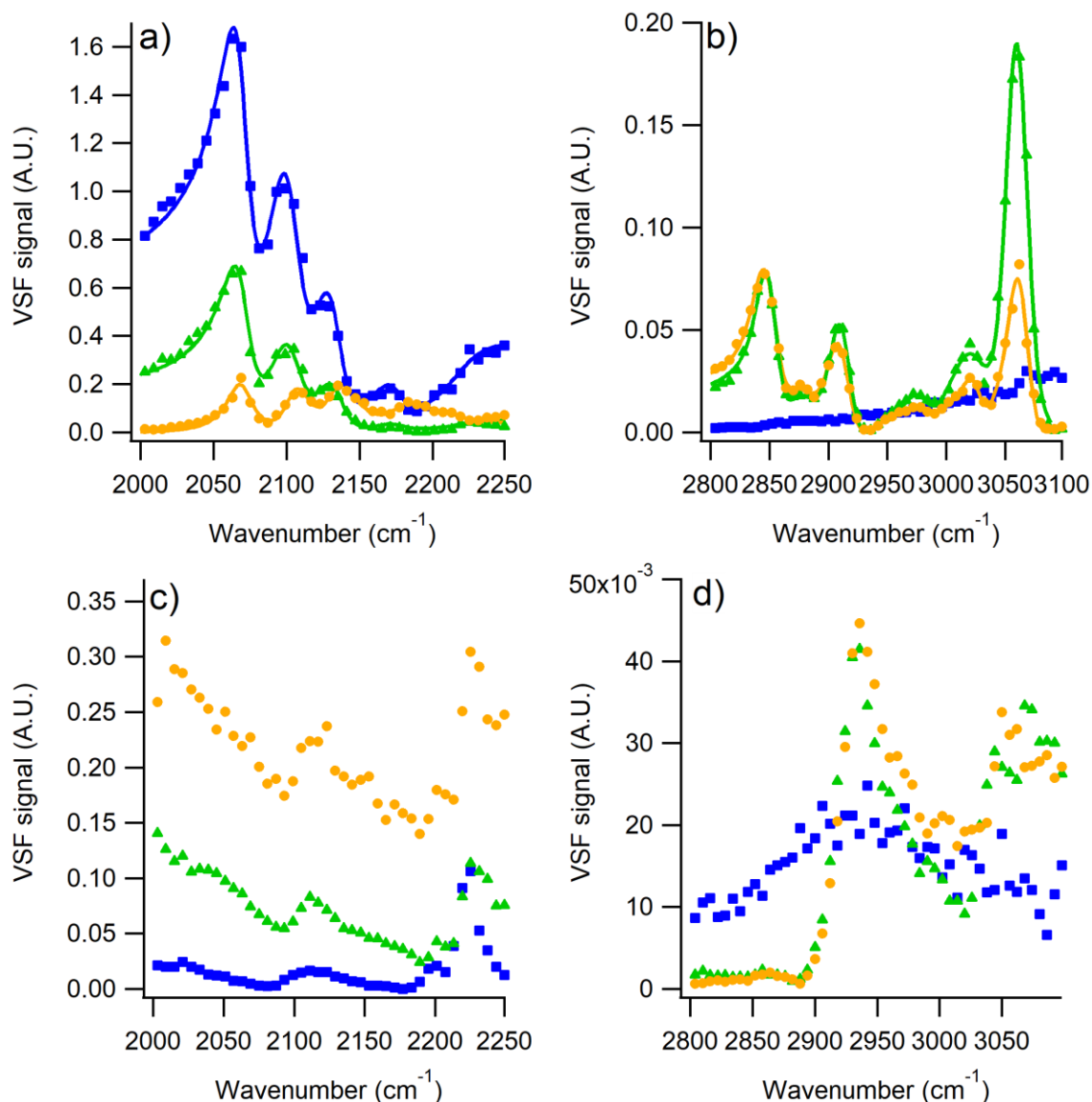


**Figure 4.6.** VSF spectra of d-DTAB/PSS at the  $\text{CCl}_4/\text{D}_2\text{O}$  interface in the (a & c) C-D stretching and (b & d) C-H stretching regions. Spectra are shown in SSP (a & b) and SPS (c & d) polarization geometries. The PSS concentration is fixed at 0.10 mM, while the d-DTAB concentration is 0.20 mM (yellow circles), 6.5 mM (green triangles), or 15 mM (blue squares). Lines are fits to the data (see Tables A.2 and A.3).

response that grows gradually with increased frequency is measured but no polymer C-H modes are detected. In the absence of PSS, DTAB solutions exhibits the same featureless response which increases with increasing DTAB concentration (not shown). This signal is attributed to O-H stretching modes of trace amounts of hydrogenated water molecules

aligned by the strong interfacial electric field. Nevertheless, the absence of C-H signal at 15 mM d-DTAB/PSS confirms that PSS does not adsorb at this concentration.

If a secondary layer of PSS were to adsorb, which was seen previously with 6.5 mM DTAB/PSS at the air/water interface,<sup>77,78</sup> I would expect either an increase in CH<sub>2</sub> signal, or, if the second layer of PSS had an orientation opposite that of the primary layer, lowered CH<sub>2</sub> signal caused by destructive interference. Since the signal at 2850 cm<sup>-1</sup> and 2910 cm<sup>-1</sup> is similar for both concentrations of d-DTAB it is concluded that there are similar amounts of adsorbed PSS at 0.20 mM and 6.5 mM DTAB. This conclusion is further corroborated by the similarity in the surface pressure values measured in Figure 4.2a. Increases in VSF signal, such as that exhibited at ~3050 cm<sup>-1</sup> by phenyl C-H modes of 6.5 mM d-DTAB/PSS (Figure 4.6b), arise from either an increased number density or increased orientation of vibrational modes at the interface. It is known that PSS and DTAB interact electrostatically through their charged groups.<sup>79</sup> Given that the charge ratio of the 6.5 mM DTAB/PSS interface is closer to unity than that of the negatively charged 0.2 mM DTAB/PSS interface, there is greater charge-complexation between DTAB and PSS at 6.5 mM DTAB/PSS. I conclude that the higher charge-complexation leads to an increase in orientation of PSS's charged sulfonate group perpendicular to the interface and hence increases the phenyl C-H signal. From these results it is concluded that the interfacial structure at both 0.2 mM and 6.5 mM DTAB/PSS is a monolayer of DTAB with PSS electrostatically bound to surfactant headgroups.

### Summary

The combination of DTAB and PSS has been studied at the oil/water interface and found to exhibit strong surface activity dependent upon DTAB concentration as summarized in Figure 4.7. At a low DTAB concentration a mixed monolayer of DTAB and extended PSS readily adsorbs to the oil/water interface. Both chemicals display significant molecular ordering of their vibrational dipoles perpendicular to the surface. The interfacial monolayer and bulk P/S complexes are measured to contain similar P/S ratios. As the concentration of DTAB is increased this ratio nears unity, and low-charge complexes coalesce and precipitate. The interfacial P/S monolayer is unaffected by the

bulk precipitation, and a greater packing of interfacial DTAB serves to enhance the perpendicular orientation of PSS's charged groups. At high DTAB concentration no vibrational modes of PSS are detected at the interface as confirmed through the use of deuterated surfactant. It is concluded that above the *cmc*, PSS preferentially combines with DTAB micelles to form non-adsorbing complexes of high positive charge. These results align well with a prior model that predicts interfacial depletion of PSS above the *cmc*,<sup>71</sup> however they contrast with multilayer formation seen in this system at the air/water interface.<sup>77,78</sup>

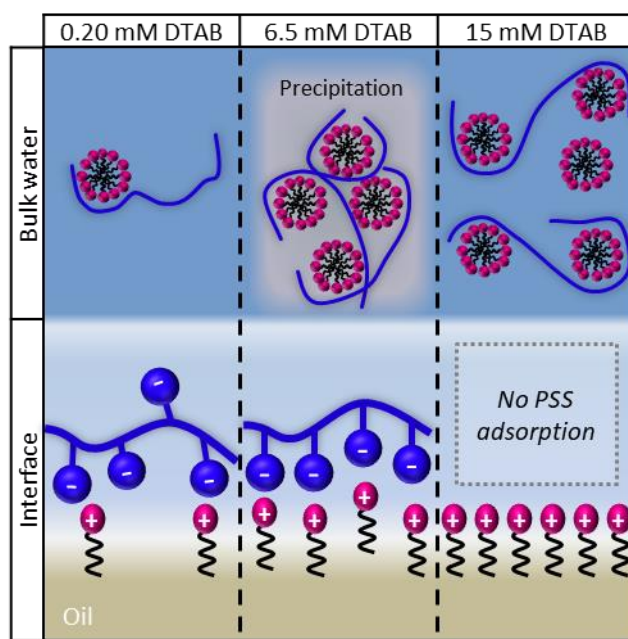


**Figure 4.7.** Cartoon representing adsorption of DTAB/PSS at the oil/water interface under increasing DTAB concentration.

## Conclusions

The strong interfacial coadsorption of oppositely charged P/S combinations has shown promise for industrial applications including oil remediation and emulsion stabilization. Multilayer formation in these systems has been pursued to allow for further control and stabilization of oil/water interfaces, such as for use in targeted drug delivery. Despite the importance of the molecular interactions which lead to enhanced coadsorption, only cursory tensiometry studies have previously been performed on P/S systems at the oil/water interface. This chapter combines surface tensiometry, zeta

potential analysis, and surface-specific vibrational spectroscopy to detail how PSS adsorption depends on DTAB concentration. While there is general agreement in the literature that both DTAB and PSS coadsorb as a mixed monolayer at low DTAB concentrations, questions remain about the adsorption behavior and structure at higher surfactant concentrations. This study finds that DTAB and PSS coadsorb as a mixed monolayer below the *cmc* with a P/S ratio similar to that measured in bulk complexes. In the region where precipitating complexes form in bulk, no thickening of the interfacial layer is seen. It is concluded that the amount of adsorbed PSS is the same as it is at lower DTAB concentrations, contrary to what has been seen at the air/water interface. Above the *cmc* all PSS remains solvated in bulk complexes and only DTAB adsorbs to the interface.

This chapter and the next chapter detail the importance of molecular-specific techniques when exploring the structure of coadsorbing P/S layers. At the concentrations studied, DTAB/PSS multilayering is not found at the oil/water interface and the PE does not adsorb at high DTAB concentration near the *cmc*. Exclusion of interfacial PE at high surfactant concentration is seen in the literature, although there is debate as to the specific surfactant concentration and timescales at which desorption occurs.<sup>76,94,100,101</sup> A previously published model predicts competition between the incorporation of polyelectrolyte in surface-active versus bulk-soluble complexes.<sup>102</sup> In this system, the formation of DTAB micelles above the *cmc* causes all PSS to be assimilated into non-adsorbing complexes, though further studies are needed to determine if sharp desorption occurs at the *cmc*. Systems which rely on P/S coadsorption would best avoid surfactant concentrations in excess of the system *cmc*. Further time-dependent studies are needed to determine if more complex interfacial structures are formed during the initial period of surface pressure increase, and to test the long-term stability of strongly interacting P/S systems. This chapter provides valuable structural information about interfacial P/S orientation and charge ratio for electrostatically interacting P/S combinations. The next chapter will explore how surfactants can engage in hydrophobic interactions with a partially charged polyelectrolyte.

## CHAPTER V

### MIXED SYSTEMS, MIXED FORCES: HYDROPHOBIC AND ELECTROSTATIC POLYELECTROLYTE/SURFACTANT INTERACTIONS LEAD TO ENHANCED COADSORPTION

As discussed in prior chapters, synergic polymer/surfactant (P/S) combinations have been proposed as a “silver bullet” to stabilize and modify air/water and oil/water interfaces for use in pharmaceuticals, oil remediation, and industrial applications. Because the strong P/S interactions occur through electrostatic attraction between oppositely charged components, strong polyelectrolytes are the focus of many P/S studies. For example, in the last chapter it was found that the principle binding between poly(styrene sulfonate) and dodecyltrimethylammonium bromide is electrostatic. However, hydrophobic interactions are known to contribute to P/S complexation, especially for polyelectrolytes with low fractional charge or low charge density. When polyelectrolytes contain an acid or base moiety, the fractional charge depends on solution pH, which in turn can affect the degree of P/S complexation and thus the surface activity (or in some cases, inactivity). Since many proposed P/S applications involve an aqueous phase, P/S behavior pH dependent polyelectrolytes cannot be ignored. This chapter explores the coadsorption of poly(acrylic acid) (PAA) and cationic cetrimonium bromide (CTAB), with the specific aim of deducing interfacial polyelectrolyte structure as it depends on PAA concentration. At the studied pH, PAA is ~30% charged, which causes system behavior to deviate from that of the prior chapter. At low PAA concentrations, it is found that hydrophobic effects dominate the coadsorption of both components, which leads to a modest increase in system surface activity. After a certain threshold PAA concentration is surpassed, electrostatic binding between PAA and CTAB dominates their interfacial behavior and leads to a drastic increase in coadsorption. Once the system’s P/S charge ratio reaches unity, no further PAA adsorbs and greater concentrations of PAA do not lead to greater adsorption. This work has previously been published as Schabes, B. K.; Altman, R. M.; Richmond, G. L. **Come Together:**

**Molecular Details into the Synergistic Effects of Polymer–Surfactant Adsorption at the Oil/Water Interface.** *J. Phys. Chem. B* **2018**, *122* (36), 8582–8590 DOI:

[10.1021/acs.jpcc.8b05432](https://doi.org/10.1021/acs.jpcc.8b05432).<sup>87</sup> I designed the study, did all the writing, and performed all experiments except for the zeta potential data, which were obtained by graduate student Rebecca M. Altman.

## Introduction

Surfactants are ubiquitous, the workhorse of many applications in the environment and our everyday lives including oil remediation and recovery,<sup>104</sup> pharmaceuticals,<sup>105</sup> personal-care products,<sup>106</sup> food science,<sup>107</sup> paints,<sup>108,109</sup> and lubricants.<sup>110</sup> Many of these uses involve modulation of an oil/water interface through surfactant assembly that lowers surface tension and stabilizes emulsions. To minimize the total detergent concentration needed, synergistic mixtures of polymers and surfactants are used concurrently to form P/S complexes, which dictate interfacial properties.<sup>50,106</sup> P/S synergy has been documented by methods such as interfacial tension, neutron scattering, and x-ray scattering.<sup>50,93,104,111–113</sup> It is known that when polymer and surfactant are oppositely charged, the resultant P/S systems have enhanced and unpredictable colloidal effects.<sup>50,59,65,93,107,111,114,115</sup> These effects rely on a fine interplay between many factors: the hydrophilic/lipophilic balance of the continuous phase, the aqueous solubility of the dispersed oil phase (Ostwald ripening), and the action of any emulsifiers.<sup>43</sup> Within a breadth of choices, combinations of polymer and surfactant can offer specific tunability to pH, ionic strength, temperature, and metal chelation.<sup>10,43,116</sup> Although there is increasing information about how polymers and surfactants behave individually at an oil/water interface,<sup>40,83,117,118</sup> less is known about the molecular factors allowing them to have an elevated interfacial impact when working in concert. A molecular-level understanding of their structure-function relationship at the oil/water interface will allow predictability of which system is best suited for a given application.

This chapter focuses on the molecular mechanism by which CTAB and PAA work synergistically at a CCl<sub>4</sub>/water interface (PAA and CTAB molecular structures are shown in Figure 5.1). PAA has been used industrially as a desiccant and emulsifier. PAA's simple structure makes it a model polymer for studies involving carboxylate

chelation and fractional polymer ionization. The interfacial activity of PAA at an oil/water interface exhibits pH-tunable behavior. Below pH 4.5, PAA forms an initial ordered polymer layer with subsequent disordered layers. Above pH 4.5, deprotonation of PAA's carboxylic acid groups causes it to remain fully solubilized in the aqueous bulk.<sup>82,83,119</sup> CTAB is well known to adsorb at an oil/water interface.<sup>42,120,121</sup> Interfacial studies of PAA/surfactant systems are rare, but the polyacid's interaction with surfactant in bulk solution has been studied more thoroughly with a variety of techniques and simulations.<sup>122–126</sup>

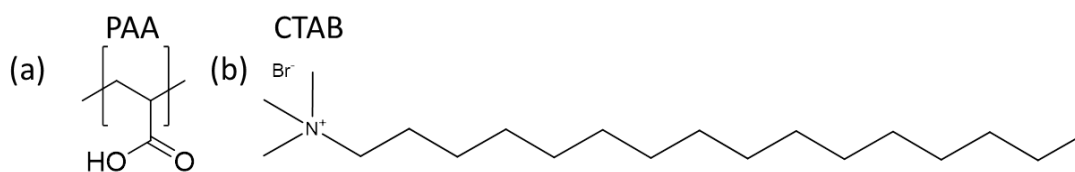


**Figure 5.1.** Molecular structures of (a) PAA and (b) CTAB.

Both CTAB and PAA concentration are kept in the dilute regime to avoid the polyelectrolyte overlap concentration.<sup>127</sup> CTAB concentration is fixed at 15  $\mu\text{M}$ , while PAA concentration is varied from 1.4  $\mu\text{M}$  to 4200  $\mu\text{M}$ . Note that polymer concentration is given with respect to individual monomer units. Because P/S behavior can be heavily influenced by ionic strength, no buffer is used, and small amounts of NaOH (or NaOD) are used to adjust the stock solutions to pH (pD) 5.5. The pH (pD) of the resultant diluted solutions are thus between pH (pD) 5.3 – 6.1, as shown in Figure 5.2 and summarized in Table 5.1. As pH increases, deprotonation of PAA's COOH groups causes the polymer to be more charged. In the pH range of this study, PAA is 10 – 26% ionized, according to Arnold's work (summarized in Appendix B).<sup>128</sup>

This chapter shows that for an interface initially populated with highly ordered CTAB, adsorption at low PAA concentration is driven by hydrophobic forces. These forces do not impart significant interfacial ordering of the polymer. With increasing PAA concentration up until charge neutralization at the iso-electric point, PAA co-adsorbs with the CTAB resulting in both polymer and surfactant showing a high degree of interfacial orientation. These results illustrate how both hydrophilic and lipophilic domains are important for macromolecule adsorption to the oil/water interface in the presence of surfactant.

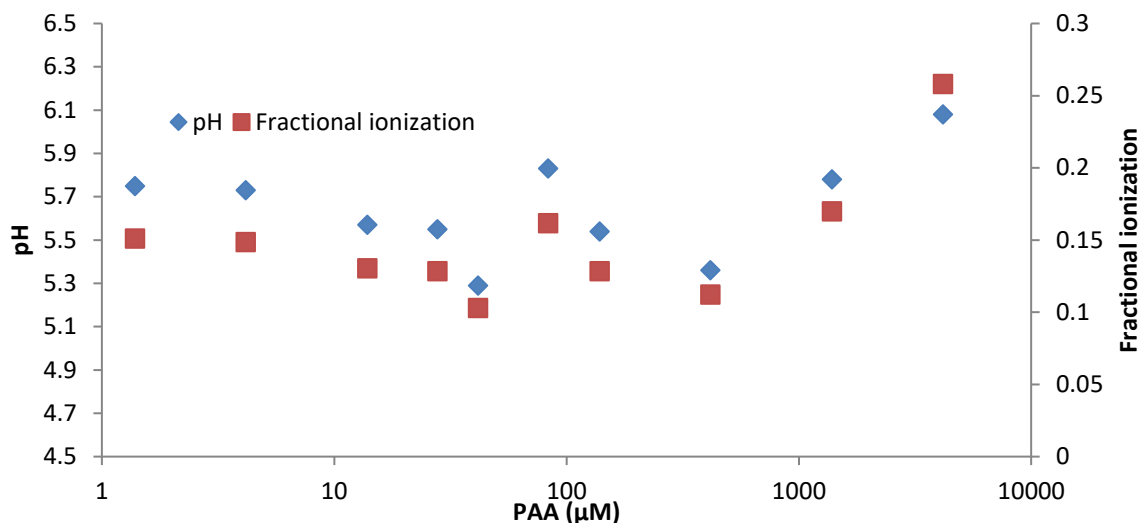


**Figure 5.2.** Solution pH (blue diamonds) and bulk PAA fractional ionization (red squares) for the PAA concentrations described in this chapter.

**Table 5.1.** Bulk data for the concentration range studied in Chapter V. The Na<sup>+</sup> comes from added NaOH or NaOD.

[PAA monomer] (μM)	[PAA] (ppm)	pH	Calculated fractional ionization	[Na <sup>+</sup> ] (μM)	[Na <sup>+</sup> ] + [Br <sup>-</sup> ] (μM, with CTAB)	Ratio PAA/CTAB	[COO <sup>-</sup> ]/[CTA <sup>+</sup> ]
0	0	5.77	-	0	15	0.00	0.00
1.4	0.1	5.75	0.15	0.4	15	0.09	0.01
4.2	0.3	5.73	0.15	1.2	16	0.28	0.04
14	1.0	5.57	0.13	3.9	19	0.93	0.12
28	2.0	5.55	0.13	7.7	23	1.9	0.24
42	3.0	5.29	0.10	11	26	2.8	0.29
83	6.0	5.83	0.16	22	37	5.6	0.90
139	10	5.54	0.13	44	59	9.3	1.2
417	30	5.36	0.11	107	122	28	3.1
1389	100	5.78	0.17	422	437	93	16
4167	300	6.08	0.26	1288	1303	278	72

### Zeta potential and surface pressure measurements

The results for zeta potential (ZP) measurements of bulk complex shear plane potentials as a function of PAA concentration with CTAB concentration held constant are shown in Figure 5.3a. Under fixed 15 μM CTAB, ZP becomes progressively more negative as PAA concentration increases. In contrast to the PSS/DTAB system described in Chapter IV, there is no concentration region where the bulk complexes have a net

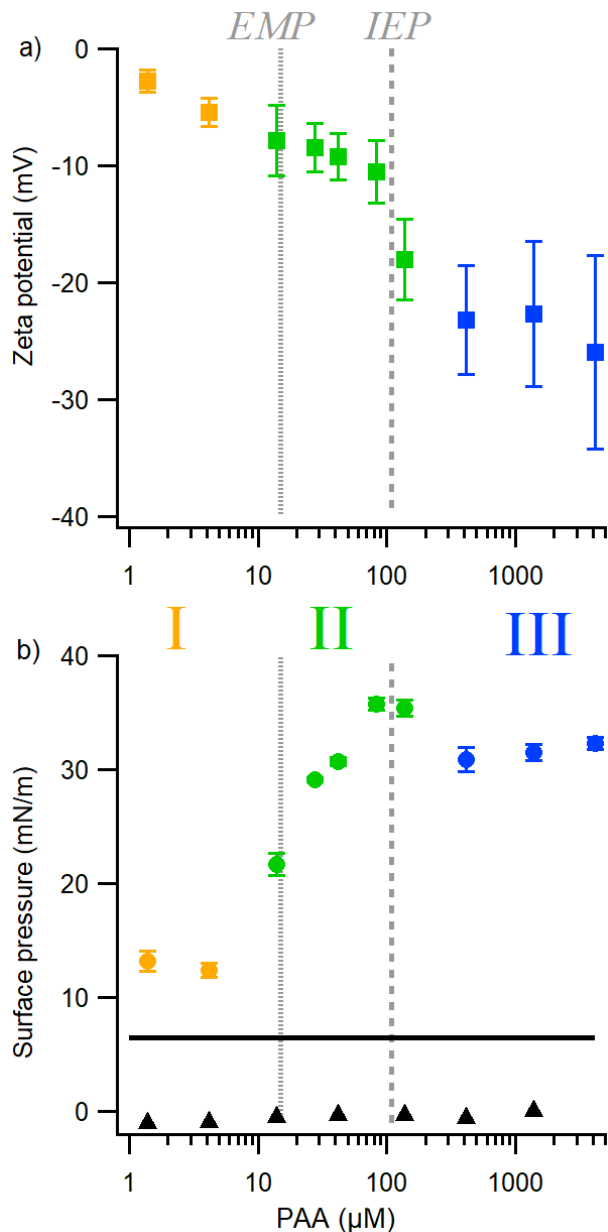


**Figure 5.3** (a) Bulk solution ZP and (b) surface pressure as a function of PAA concentration under fixed 15  $\mu\text{M}$  CTAB. Error bars represent the standard error of averaged measurements. Regimes are color-coded for clarity; orange, green, and blue points indicate regime I, II, and III, respectively. The dotted and dashed grey lines represent the concentration of PAA corresponding to the system's equipotential point (EMP) and isoelectric points (IEP), respectively. On the bottom figure, black triangles signify the surface pressure of a PAA solution without CTAB, and the black line signifies the surface pressure of a 15  $\mu\text{M}$  CTAB solution without polymer.

positive charge, even when the positively charged CTAB concentration is much higher than that of PAA monomers. I attribute this to a surface excess of CTAB, resulting in

bulk solution complexes with fewer CTAB molecules than deprotonated carboxylic acid moieties. Increasing the ratio of PAA to CTAB causes solution complexes to become more negative, as seen in similar systems.<sup>85,129</sup> Despite the low zeta potential values, there is no evidence of precipitation or colloidal instability at any concentration studied, as confirmed by measuring sample absorbance at 450 nm, shown in Figure 5.4.

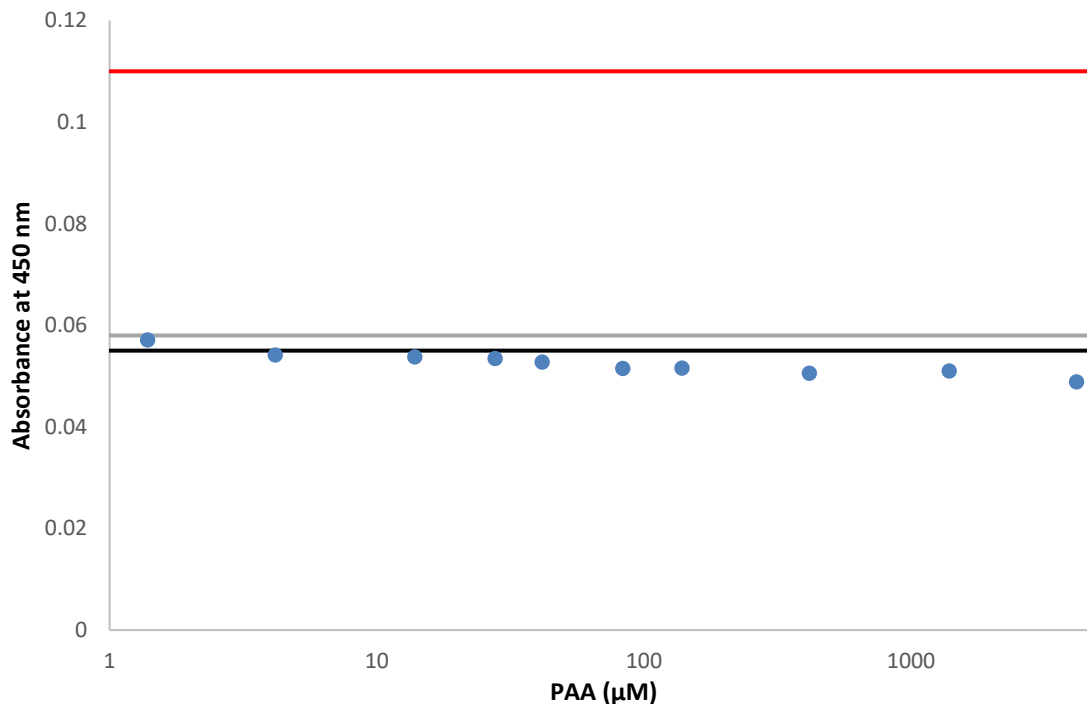


**Figure 5.4.** UV/Vis extinction data for PAA/CTAB solutions at 450 nm. CTAB concentration is fixed at 15  $\mu\text{M}$ , and PAA concentration varies as indicated on the bottom axis. The grey and black lines represent the absorbance of water and 15  $\mu\text{M}$  CTAB solutions used as a control, respectively. The red line is used for reference of a chemically similar solution with known colloidal instability: 100  $\mu\text{M}$  CTAB with 97  $\mu\text{M}$  poly(styrene sulfonate) exhibits UV-Vis absorbance of 0.11 at 450 nm. These data were taken 1 day after mixing to match the age of solutions used in spectroscopy, however, no changes were observed over 5 days, even after mechanical perturbation.

Surface pressure measurements were used to determine the interfacial activity of the PAA/CTAB system (Figure 5.3b). Dynamic surface tension data can be found in Figure 5.5 for representative P/S concentrations. All surfactant solutions exhibit a rapid surface tension decrease during the first 10 minutes (Figure 5.5a), and those with additional polymer continued a gradual surface tension decrease for many hours until

eventual equilibration (Figure 5.5b). PAA on its own is not interfacially active above pH 4.5,<sup>83,130</sup> and thus does not exert a surface pressure (Figure 5.3b, black triangles). These findings are corroborated spectroscopically, as pure PAA solutions give the same VSF spectra as the neat CCl<sub>4</sub>/D<sub>2</sub>O interface. In contrast, CTAB is very surface active and establishes a surface pressure of 6.4 mN/m at 15  $\mu$ M concentration (Figure 5.3b, black line). When PAA is combined with 15  $\mu$ M CTAB, there is interfacial synergy at all studied PAA concentrations as evidenced by the system's surface pressure exceeding that of 15  $\mu$ M CTAB. Even at low PAA concentrations, surface tensiometry shows that the PAA/CTAB system has heightened interfacial activity which continues to increase beyond the system's equimolar point (EMP, dotted grey line in Figure 5.3). The 35 mN/m maximum in surface pressure, seen at the system's isoelectric point (IEP, dashed grey line in Figure 5.3), is close to the 40 mN/m surface pressure exerted by a CTAB solution at its critical micelle concentration (950  $\mu$ M), despite this system having 60 times less CTAB. Zeta potential data show a sharp increase in the magnitude of the shear plane potential, indicating an increase in complex negative charge beyond the IEP at 110  $\mu$ M PAA (Figure 5.3a), which coincides with a maximum in surface pressure (Figure 5.3b). This is the point of surface saturation. Beyond 140  $\mu$ M PAA, additional polymer stays solubilized in the bulk, leading to a greater negative charge on bulk solution complexes. At PAA concentrations greater than 200  $\mu$ M, neither the average charge on the bulk solution complexes nor the surface pressure depends strongly on PAA concentration. It is concluded that charge-charge repulsion between solution-phase P/S complexes and free PAA prevents further accumulation of PAA in bulk complexes.

It is clear from Figure 5.3 that neither ZP nor surface pressure depends linearly on PAA concentration. The system's behavior can be roughly divided into three regimes of PAA concentration as prior work has seen in other P/S air/water systems.<sup>75,104,127</sup> The first regime is marked by modest surface pressure and slightly negative complexes in bulk solution. The second regime encompasses the EMP at 15  $\mu$ M and the IEP at approximately 110  $\mu$ M PAA. Below the IEP, surface pressure sharply increases while bulk complex charge remains relatively unchanged. Immediately after the IEP, zeta potential becomes more negative, while surface pressure is unchanged. The third regime, where PAA is in excess, shows little change in both surface pressure and ZP, despite a

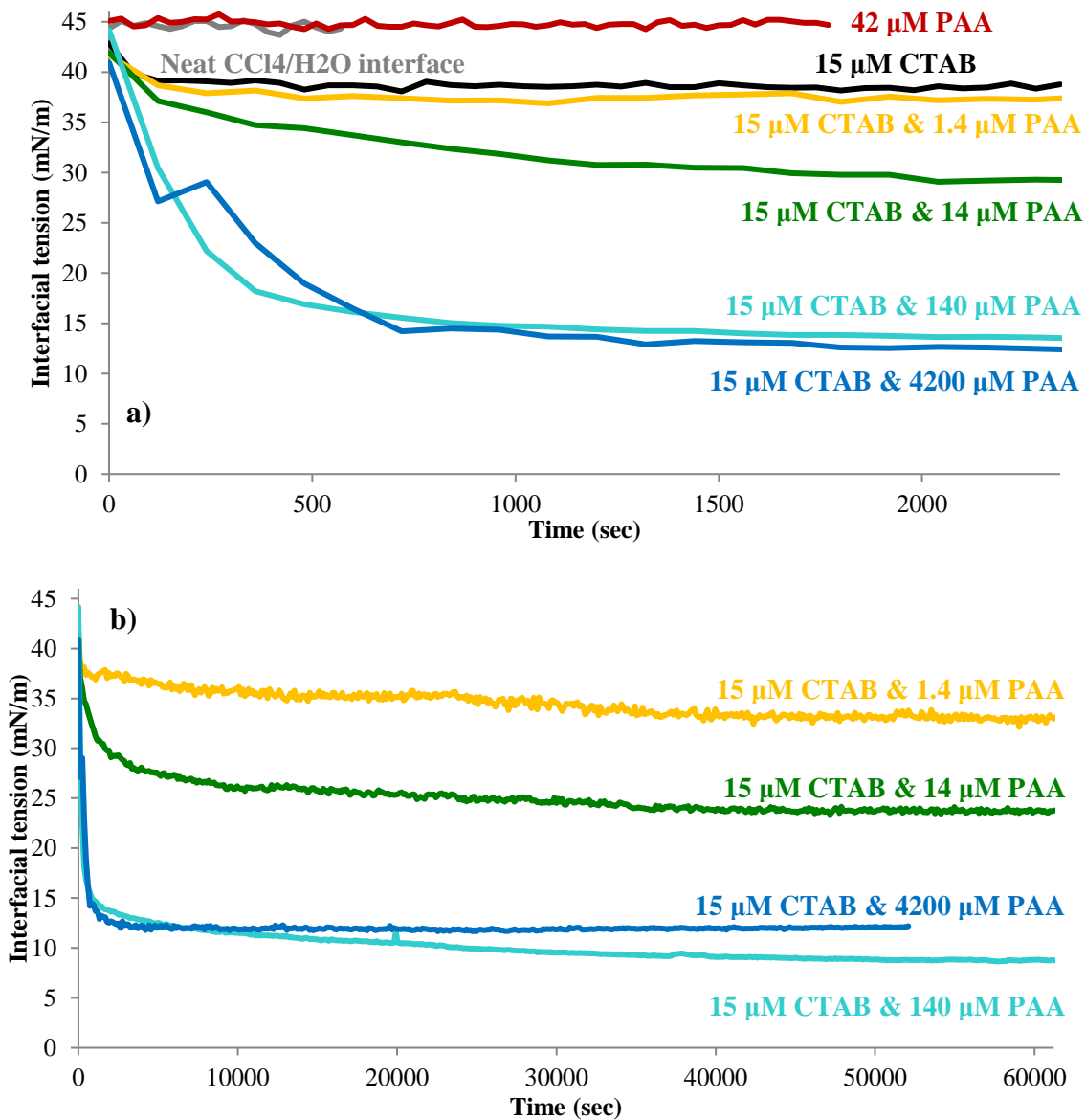


**Figure 5.5.** Dynamic surface tension for representative concentrations of CTAB and PAA. The first 2500 seconds of all samples are shown in a). PAA/CTAB mixtures have longer equilibration times, shown in b).

30-fold increase in polymer concentration. From these data it is clear that the system's interfacial activity depends on polymer concentration, and the structure-function relationship of that synergy is explored in the VSFS studies to follow.

## Vibrational sum frequency spectroscopy measurements

Vibrational spectra are taken in various spectral regions to determine the molecular structure of adsorbed polymer, surfactant, and interfacial water. The spectroscopic results relate structure to macroscopic trends observed through ZP measurements and surface tensiometry. All spectra shown have a fixed 15  $\mu\text{M}$  d-CTAB concentration, with varying 1.4 – 4200  $\mu\text{M}$  PAA concentrations. Figure 5.6a shows the VSF response for the C-D stretch modes of adsorbed d-CTAB whereas Figure 5.6b corresponds to the VSF response of the O-D stretch modes of interfacial  $\text{D}_2\text{O}$  molecules. The intermediate region from 2250 – 2450  $\text{cm}^{-1}$  was not measured due to  $\text{CO}_2$  absorption of the IR beam. The presence and oriented nature of the alkyl chains of d-CTAB at the interface is evidenced by C-D spectral features in Figure 5.6a. The O-D stretch modes in Figure 5.6b also indicate the orientation of water dipoles with a component normal to the interface. Due to extensive hydrogen bonding, the interfacial vibrations of  $\text{D}_2\text{O}$  are extremely broad,<sup>54–57</sup> and appear as a significant background in all spectral regions studied, especially the C-D region (Figure 5.6a). It is well established that increasing charge at an oil/water interface results in a larger number of aligned water molecules and consequently larger VSF signal. The intensity of the coordinated  $\text{D}_2\text{O}$  modes in Figure 5.6b therefore serves as a proxy for the magnitude of interfacial charge. Such is the case shown in Figure 5.6b with increasing PAA concentration where the interfacial charge is neutralized by greater surface partitioning of PAA. The lowered  $\text{D}_2\text{O}$  signal reveals clearer spectral features for the four C-D vibrational modes of d-CTAB: the  $\text{CD}_3$  symmetric stretch at 2073  $\text{cm}^{-1}$ , the  $\text{CD}_2$  symmetric stretch at 2105  $\text{cm}^{-1}$ , a Fermi resonance at 2134  $\text{cm}^{-1}$ , and the headgroup  $\text{CD}_3$  asymmetric stretch at 2180  $\text{cm}^{-1}$ .<sup>38</sup> The existence of these peaks indicates that the C-D modes of d-CTAB have a net orientation at the oil/water interface at all PAA concentrations studied.

The VSF spectra in Figure 5.7 show the vibrational features of PAA under the same fixed d-CTAB concentration as Figure 5.6. Because PAA is a weak polyacid, its carboxylic acid functional groups exist in equilibrium between protonated and deprotonated forms, each with a unique vibrational frequency. The spectra in Figure 5.7a is attributed to the carboxylate symmetric stretch at 1409  $\text{cm}^{-1}$  that arises from  $\text{COO}^-$  moieties. Because these moieties give signal in the SSP polarization geometry, they are

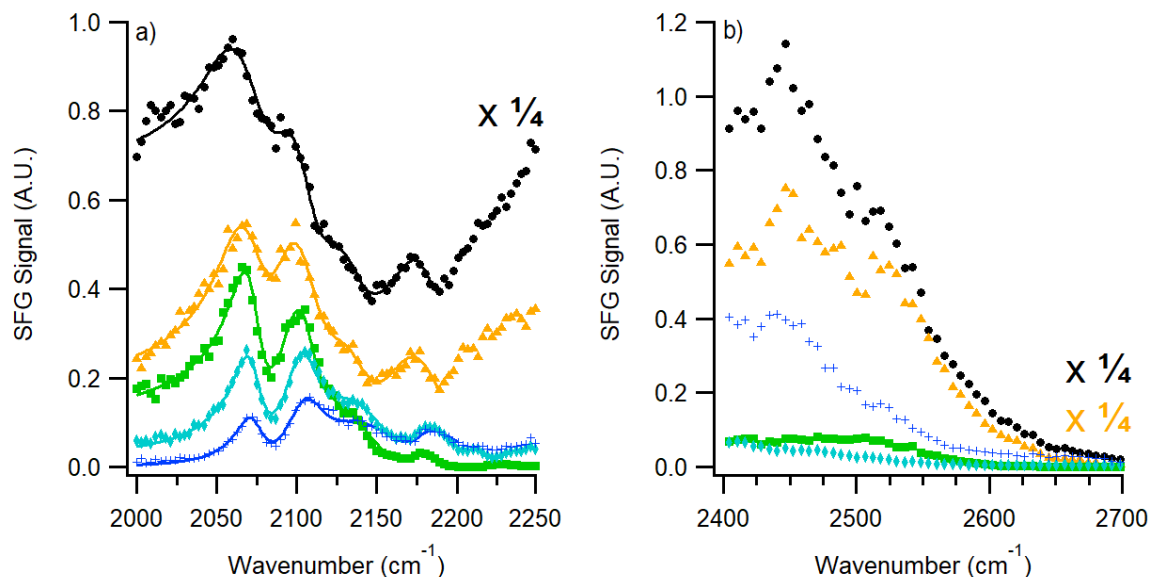


**Figure 5.6.** VSF spectra of PAA/d-CTAB surface complexes as a function of PAA concentration under fixed 15  $\mu\text{M}$  d-CTAB concentration showing (a) C-D modes of deuterated CTAB and (b) O-D modes of interfacial  $\text{D}_2\text{O}$ . PAA concentration was 0  $\mu\text{M}$  (black circles), 1.4  $\mu\text{M}$  (orange triangles), 14  $\mu\text{M}$  (green squares), 140  $\mu\text{M}$  (cyan diamonds), and 4200  $\mu\text{M}$  (blue crosses). Lines are fits to the data. Both 0  $\mu\text{M}$  PAA traces and the 1.4  $\mu\text{M}$  PAA trace of (b) have been scaled by a factor of 0.25 for clarity. See Table C.1c for fitting parameters.

not lying flat on the interface. Signal at 0  $\mu\text{M}$  PAA is attributed to low-frequency  $\text{D}_2\text{O}$  modes. IR absorbance by  $\text{CCl}_4$  at the edge of this spectral window can impart the appearance of a peak. Observable in Figure 5.7b are contributions from the symmetric stretch carbonyl modes of oriented COOH groups on PAA. Fits to the spectra (see Appendix C, Table C.1b) show two peaks at 1732  $\text{cm}^{-1}$  and 1743  $\text{cm}^{-1}$ , which are out of phase with one another. Alternatively, one well-solvated COOH mode at 1732  $\text{cm}^{-1}$  could be destructively interfering with low-frequency  $\text{D}_2\text{O}$  modes (discussed further below). Interfacial ordering of the C-H backbone modes of the polymer is evidenced by the strong and sharp signal from the  $\text{CH}_2$  symmetric stretch modes. Fitting routines place these peaks at 2852, 2900, 2933, and 2942  $\text{cm}^{-1}$ , corresponding respectively to the  $\text{CH}_2$  symmetric stretch, the  $\text{CH}_2$  Fermi resonance, the  $\text{CH}_3$  Fermi resonance, and the  $\text{CH}_3$  asymmetric stretch of methyl-terminated PAA chains (Table C.1d).<sup>83,85</sup> As in Figure 5.6, the coordinated  $\text{D}_2\text{O}$  modes act as a significant background in the carboxylate and carbonyl regions (Figures 5.7a & 5.7b), which is why signal is detected in both of those regions at 0  $\mu\text{M}$  PAA (black circles).

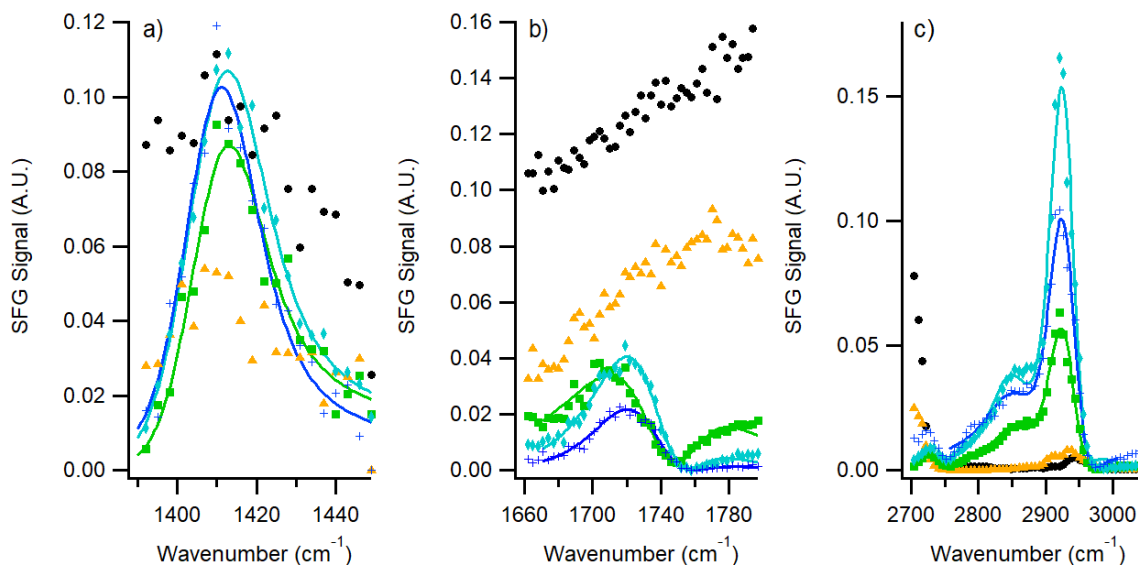


**Figure 5.7.** VSF spectra of PAA/d-CTAB surface complexes as a function of PAA concentration under fixed 15  $\mu\text{M}$  d-CTAB concentration showing vibrational residues unique to PAA in the (a) carboxylate, (b) carbonyl, and (c) C-H stretch regions. PAA concentration was 0  $\mu\text{M}$  (black circles), 1.4  $\mu\text{M}$  (orange triangles), 14  $\mu\text{M}$  (green squares), 140  $\mu\text{M}$  (cyan diamonds), and 4200  $\mu\text{M}$  (blue crosses). See Tables C.1a, C.1b, and C.1d for fitting parameters.

### Regime I: 1.4 $\mu\text{M}$ – 4.2 $\mu\text{M}$ PAA

In the first regime, where CTAB is in excess with increasing PAA, an increased surface pressure over that of 15  $\mu\text{M}$  CTAB alone indicates an increased level of adsorbate (Figure 5.3b). Spectrally, charge neutralization lowers the intensity of the coordinated  $\text{D}_2\text{O}$  modes in all spectral regions below 2700  $\text{cm}^{-1}$  – this change is most prominent in the  $\text{D}_2\text{O}$  region (Figure 5.6b). Careful observation of Figure 5.7c shows a slight increase in C-H signal over that of the 15  $\mu\text{M}$  CTAB solution. Additional regime I spectra run at 4.2  $\mu\text{M}$  PAA (not shown) have a similar level of C-H signal between 2900 and 2950  $\text{cm}^{-1}$ . Although it is tempting to ascribe this to the adsorbed PAA present at the interface, there is a lack of significant increase over the lone CTAB trace, as well as an incongruous peak shape between regime I and regime II C-H signal (yellow and green trace, respectively). Any VSF contribution from ordered PAA is negligible. Considering the absence of any other PAA vibrational features in the carbonyl and carboxylate regions, it is concluded that PAA present at the interface lacks net orientation in this regime. Increased charge screening at the interface could allow more efficient packing of

d-CTAB, leading to changes in signal near  $2950\text{ cm}^{-1}$ , which arise from the incomplete deuteration of d-CTAB. The most likely bulk structure of low ionization PAA proposed in the literature is a compact coil configuration.<sup>131,132</sup> I find this the most likely structure for interfacial PAA in regime I, where internal centrosymmetry of the coil forbids VSF signal. As demonstrated in the next section, when PAA and CTAB interact through their electrostatic dipoles, the PAA undergoes a structural change, leading to a VSF-active carboxylate mode with a frequency indicating close proximity to a cation (i.e., d-CTAB's quaternary amine headgroup). In the absence of such signal for this concentration, it is concluded that hydrophobic interactions attract PAA to interfacial CTAB, where it acts as a charge-screening polyion, yet the dipoles of the carboxylate or carbonyl modes do not adopt a net orientation perpendicular to the interface, and thus do not give VSF signal. For systems below 30% ionization, initial surfactant interaction is most likely through hydrophobic forces.<sup>115,133–137</sup>

### **Regime II: 14 $\mu\text{M}$ – 140 $\mu\text{M}$ PAA**

An increase in surface pressure near the EMP (Figure 5.3b) marks the beginning of the regime which contains the greatest P/S interfacial synergy. Signal from coordinated  $\text{D}_2\text{O}$  has greatly decreased (Figure 5.6b), indicating a much more neutral interface, and the carboxylate, carbonyl, and alkyl modes of PAA are visible spectrally (Figure 5.7). The carboxylate peak location resembles that seen in this lab's prior work where charge-coupling binds PAA to various metal ions.<sup>40,81,138–140</sup> These modes were only visible spectroscopically when PAA carboxylate modes were bound to a metal cation. It is concluded that similar electrostatic attraction between d-CTAB headgroups and PAA carboxylate uncoils interfacial PAA and orients the dipole moment of the carboxylate mode perpendicular to the surface. Signal from the uncharged carbonyl mode of PAA arises near  $1720\text{ cm}^{-1}$  (Figure 5.7b). A peak from the uncharged carbonyl mode of PAA at  $1732\text{ cm}^{-1}$  corresponds to hydrated COOH groups, indicating they are oriented towards the aqueous phase. A trough is visible near  $1750\text{ cm}^{-1}$  and signifies the carbonyl mode destructively interferes with a mode of higher-frequency: either less solvated carbonyl groups in an opposite orientation, or the broad response of interfacial  $\text{D}_2\text{O}$ . In the former case, the higher frequency mode at  $1743\text{ cm}^{-1}$  would correspond to COOH

groups in a more hydrophobic environment which includes  $\text{CCl}_4$  and also the alkyl chains of CTAB. In the latter case, carbonyl signal would only arise from modes pointing away from the oil phase. Prior work in this lab has favored the former methodology, where carbonyl signal represents two hydration states of the carbonyl functional group.<sup>80,141</sup> Additionally, the interference at  $\sim 1750\text{ cm}^{-1}$  is most pronounced for the  $14\text{ }\mu\text{M}$  and  $140\text{ }\mu\text{M}$  PAA traces. At these concentrations, coordinated  $\text{D}_2\text{O}$  signal measured in Figure 5.6b is at a minimum, so it is likewise expected to be minimal throughout the rest of the spectrum. Since the interference remains sharp at these concentrations, it is concluded that PAA carbonyl groups exist in two solvation environments, which point in opposite directions. Previous VSF studies of PAA adsorbed alone at this interface display only a single carbonyl mode at  $1730\text{ cm}^{-1}$  whereas identical studies with the more hydrophobic poly(methacrylic acid) show both the hydrated  $1730\text{ cm}^{-1}$  carbonyl peak and a second higher frequency peak which is also attributed to  $\text{COOH}$  moieties oriented in a more hydrophobic environment.<sup>32,139,142</sup>

At  $140\text{ }\mu\text{M}$  PAA, which is near the system's IEP, a maximum in surface pressure (Figure 5.6b) corresponds with a maximum of signal from PAA alkyl modes (Figure 5.7c). It is concluded that the majority of additional PAA in regime II goes to the interface, which explains why there is little change in ZP from  $14\text{ }\mu\text{M}$  to  $110\text{ }\mu\text{M}$  (Figure 5.3a). Additionally, the coordinated  $\text{D}_2\text{O}$  modes are at a minimum, showing PAA has neutralized the interfacial charge. Curiously, there is little change in the carboxylate and carbonyl peak intensity between  $14\text{ }\mu\text{M}$  and  $140\text{ }\mu\text{M}$  PAA (Figures 5.7a and 5.7b). At  $14\text{ }\mu\text{M}$  PAA, there is nearly a one-to-one molar ratio between total CTAB headgroups and PAA carboxyl moieties. This leads to a strong alignment of these modes perpendicular to the interface. As PAA concentration increases, additional PAA adsorbs interfacially, which increases both the surface pressure and the alkyl modes, but does not cause a subsequent increase in orientation of the carboxylate or carbonyl modes. Prior studies of only PAA at this interface show that an initial layer of ordered polymer is followed by subsequent disordered layers. Their adsorption is reflected by increased surface pressure, but they do not contribute any VSF signal in the carbonyl and carboxylate regions due to a lack of net orientation.<sup>82,83</sup>

A note should be made comparing the concentration-dependent behavior of the PAA/CTAB system with the PSS/DTAB system discussed in Chapter IV. In Chapter IV, the polyelectrolyte concentration was fixed while the surfactant concentration was allowed to vary. It was found that the orientation of the charged groups on PSS increased with increasing surfactant concentration, while the total amount of adsorbed PSS did not change (as intuited through CH<sub>2</sub> backbone signal in Figure 4.6). In the PAA/CTAB system described in this chapter, signal from charged groups does not increase with polymer concentration, but total adsorption does (as measured by CH<sub>2</sub> backbone signal in Figure 5.7 and surface pressure in Figure 5.3). While these are different systems, a preliminary comparison implies that a majority of the available polymer adsorbs to the interface regardless of the surfactant concentration. Conversely, the orientation of the polymer charge groups increases with increasing surfactant concentration, likely due to the electrostatic effects of charge complexation, as explored in Chapter IV.

In the second regime of the PAA/CTAB system, electrostatic interactions lead to the strongest interfacial synergy that starts at the EMP and continues until the point of charge neutralization at the IEP. Electrostatic attraction between PAA carboxylate groups and CTAB headgroups anchor sections of polymer to the surfactant monolayer. Because there are a finite number of CTAB headgroups available for charge-complexation, the number of oriented carboxylate groups at the interface reaches a maximum at the EMP. On oriented sections of the polymer, well-solvated COOH groups face the aqueous phase, while disordered loops of the PAA chain extrude into the aqueous bulk.

### **Regime III: 30 – 4200 $\mu$ M PAA**

After interfacial charge neutralization at the IEP, additional PAA is no longer electrostatically attracted to the interface and stays in solution, leading to a sharp increase in bulk PAA/CTAB ratio as reflected by ZP data (Figure 5.3a). Electrostatic repulsions in bulk solution likely prevent further colloidal accumulation of PAA, leading to an approximately -25 mV minimum in ZP. Beyond 140  $\mu$ M PAA, however, neither the surface pressure nor ZP shows significant dependence upon PAA concentration (Figure 5.3).

An increase in coordinated D<sub>2</sub>O signal (Figure 5.6b) reveals that the interface of the third regime is charged, but the sign of the charge cannot be directly measured. In VSFS, vibrational modes with similar frequencies but opposite phases can destructively interfere to take on the appearance of a “negative” peak. Close inspection of the 15 μM CTAB spectrum in the C-D region (Figure 5.6a, black trace) reveals such an interference between 2175 and 2200 cm<sup>-1</sup>. The 2180 cm<sup>-1</sup> CD<sub>3</sub> asymmetric stretch of d-CTAB headgroup is out-of-phase with the coordinated D<sub>2</sub>O background, but only when PAA concentration is below the IEP. At 140 and 4200 μM PAA (cyan and blue traces), the d-CTAB mode now *constructively* interferes with the D<sub>2</sub>O background, which has been confirmed by peak fitting. As it is highly unlikely that CTAB molecules have flipped their interfacial orientation, it is concluded that an inversion of interfacial charge between 14 μM and 140 μM PAA leads to the reversal of the direction of interfacial D<sub>2</sub>O dipoles. Charge inversion at an air/water interface was determined using a similar methodology by Saha.<sup>103</sup> If the charge inversion were due strictly to additional PAA adsorption, the surface pressure would be expected to increase, when in fact the opposite occurs (Figure 5.3b). Rather, an increase in the pH of the system (from 5.7 to 6.1, Figure 5.2) leads to an increase in the fractional ionization of PAA (from 14% to 25%). These like-charge repulsions disorder the PAA chains and discourage further PAA adsorption, leading to a drop in surface pressure (Figure 5.3b) and VSF signal in the carbonyl (Figure 5.7b) and alkyl regions (Figure 5.7c). The carboxylate mode (Figure 5.7a) does not change in amplitude, frequency, or linewidth throughout the second and third regimes, despite changes in pH, interfacial charge, and PAA concentration. While the rest of the interface is in flux, the strong electrostatic interaction between the PAA carboxylates and d-CTAB headgroups is insulated from change. Charged sections of the polymer which are not bound to d-CTAB are solvated and too randomly oriented to give VSF signal – a behavior seen in this polymer previously.<sup>80</sup> In the third regime, the interface is saturated by PAA. A pH increase deprotonates PAA, giving the planar interface a negative charge. While CTAB electrostatically anchors a number of carboxylate groups, charge-charge repulsions and increased polymer solubility draw the polymer into the aqueous phase. In this region, the interfacial structure is independent of polymer concentration, and excess polymer remains in solution.

## Summary

Throughout the studied concentration series, CTAB draws PAA to the interface through both hydrophobic and electrostatic interactions, as summarized in Figure 5.8. At low polymer concentration (regime I), interactions between CTAB and PAA hydrophobic domains cause disordered PAA to adsorb to the interface, likely in a coiled configuration. In this regime, interfacial positive charges outnumber negative interfacial charges. As polymer concentration increases to the EMP, the system enters regime II and charge coupling between CTAB and PAA carboxylate groups serves to uncoil PAA, orienting both the alkyl backbone and carboxyl functional groups. The CTAB headgroup strongly orients polymer COO<sup>-</sup> groups, which electrostatically bind to the CTAB monolayer. These electrostatic interactions bring additional PAA to the interface, and the subsequent charge-neutralization allows for greater interfacial packing of both components. Interfacial accumulation is greatest at the IEP; when PAA concentrations exceed this point, the system enters regime III. A slight pH increase deprotonates PAA, and the majority of interfacial charge is negative. This excess charge is localized on anionic polymer segments which extend into the aqueous phase, symbolized in Figure 5.8, likely as a solvated coil. Like-charge repulsions prevent further PAA adsorption, and may serve to introduce interfacial disorder. However, the strong electrostatic binding between carboxylate and CTAB headgroups serves to keep at least some polymer extended and oriented.

## Conclusions

The development and design of P/S combinations for use in emulsion stabilization, targeted drug delivery, and oil remediation requires an understanding of their molecular interactions and oil/water interfacial structure. Though numerous studies detail a molecular-level picture of interfacial polymers and surfactants separately, less is understood about the molecular interactions that lead to the interfacial cooperativity seen for P/S mixtures such as those examined here. It is found that the PAA and CTAB interact through both hydrophobic and electrostatic forces, dependent upon PAA concentration. When the CTAB concentration is greater than PAA, modest synergy occurs solely through hydrophobic interactions, and the polymer likely maintains the

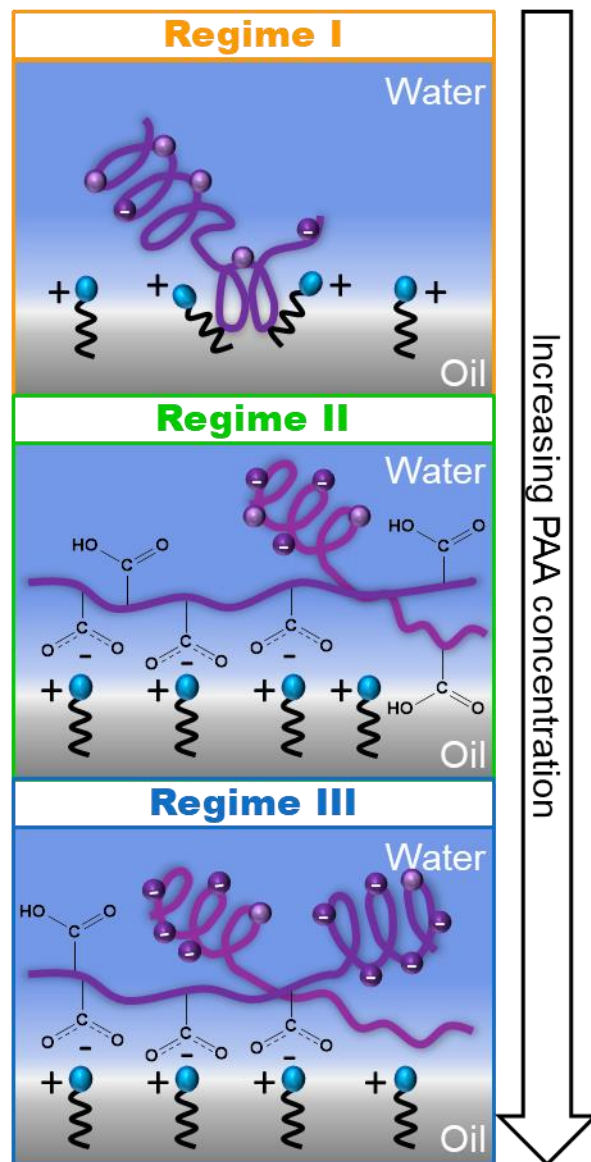


**Figure 5.8.** Cartoon representing the adsorption and assembly behavior of PAA and CTAB at the oil/water interface as a function of PAA concentration. Behavior was seen to divide into three “regimes” as described in the text. Counterions and solvent molecules have been omitted for clarity.

same structure as in bulk: a compact coil. At higher PAA concentrations, charge coupling between  $\text{COO}^-$  groups and CTAB’s cationic headgroup causes sections of PAA to change in structure and strongly adsorb in conjunction with the CTAB monolayer. The greatest interfacial accumulation of PAA comes when there is a one-to-one ratio between CTAB and charged carboxylate groups. Charge neutralization of the interface minimizes unfavorable charge-charge repulsions between components, leading to the highest co-

adsorption. After charge neutralization, additional PAA remains in bulk due to the lack of available electrostatic interactions.

While Chapter IV focused on the electrostatic interaction between PSS and DTAB, this chapter shows that hydrophobic effects are important for partially-charged polymers such as PAA. Structural observations made herein are relevant for efforts using polymers as emulsion stabilizers or interfacial templates. High P/S ratio leads to interfacial overcharging due to a slight pH change, but as in Chapter IV there is no evidence of multilayer formation at any concentration of polymer. Further interfacial layers would best interact with PAA's oriented carboxylic acid groups. These findings provide the much needed molecular details that have been lacking in previous studies of P/S systems at an oil/water interface, especially studies of polymers that are surface inactive on their own.

## CHAPTER VI

### CONCLUSIONS

Although the interface is miniscule compared to the overwhelming vastness of the bulk, some of the most important chemistry happens at that slim surface slice. The interfacial region between oil and liquid water is an especially important system in a wide number of fields, such as oil remediation, cosmetics, and food science. The addition of polyelectrolytes to a surfactant system can decrease the total amount of needed detergent, while furthermore enhancing interfacial functionality and increasing overall chemical stability. This could allow the design of robust oil-in-water emulsions and efficient oil remediation techniques. Unfortunately, due to the inaccessibility of the oil/water interface, polymer/surfactant (P/S) systems are nearly always studied at the air/water interface. This dissertation applies a surface-specific non-invasive spectroscopic technique to study the coadsorption of two model P/S combinations at the oil/water interface. The interfacial properties – especially the structuration of the polymer layer – are detailed, and it is found that both polyelectrolytes of interest are made readily surface active by addition of surfactant. The effects of concentration on P/S adsorption is a specific focus, aided by the vibrational specificity of our flagship technique.

Vibrational sum frequency (VSF) spectroscopy is a well-supported nonlinear spectroscopy frequently used to characterize single-component interfaces. Previously, it has been used to study interfacial water structuration, surfactant adsorption, and polymer layering. Because it is a vibrational spectroscopy, VSF can precisely detect and differentiate between multiple interfacial components in a variety of bonding environments, although applications on mixed P/S systems are still in their infancy. Due to its nonlinear nature, constructive and destructive interferences within spectra are used to determine the orientation of surface dipoles. Selective deuteration isolates spectral signatures from the polyelectrolyte, revealing information inaccessible to simpler techniques. Along with VSF spectroscopy, this dissertation employs a slew of complementary measurements to corroborate its spectral conclusions.

One of the most widely studied model P/S combinations is that of sodium poly(styrene sulfonate) (PSS) and dodecyltrimethylammonium bromide (DTAB).

Inexplicably, most prior studies of this P/S combination do not employ techniques capable of directly differentiating between adsorption of PSS and adsorption of DTAB. As such, unsubstantiated conclusions about PSS layering are common. Using VSF at three different concentrations of DTAB, I show that a similar amounts of polymer adsorb to the oil/water interface below the critical micelle concentration (*cmc*), and I find no evidence of multilayer formation within this region. Above the *cmc* there is no adsorption of PSS. This contrasts with prior studies showing thick multilayer formation at very high surfactant concentrations. It is proposed that soluble polymer/micelle complexes slowly form in many P/S systems, causing polymer and surfactant to migrate away from the interface. If this is the case, then the spontaneous formation of DTAB micelles at concentrations above its *cmc* hastens the interfacial depletion of polymer. Further time dependent VSF studies are needed to determine if this is the most probable mechanism of desorption.

The second system studied includes the hygroscopic poly(acrylic acid), which is frequently used as a model for environmentally important humic acids. This pH dependent polymer can be forced to the interface through metal ion chelation or under acidic conditions. Herein, I document how addition of surfactant cetrimonium bromide (CTAB) leads to an extreme enhancement of surface activity. In notable contrast to most previous studies, I show how interfacial charge and polyelectrolyte structure depend strongly on PAA concentration. At low concentration, surface synergy is modest and interfacial PAA remains tightly coiled. After increasing the PAA concentration, the highest synergy occurs when PAA uncoils and the charged groups of each species form strong electrostatic bonds with the surfactant. Eventually the interfacial charge is neutralized, which inhibits further PAA adsorption. Continued work modulating the PAA/CTAB interface would best focus on interacting with PAA's well-solvated carboxylic acid residues, or exploring the system's hydrophobic interactions through a pH study.

While the phenomenon of P/S interfacial synergy has been well-documented for decades, it is only recently that vibrationally-specific techniques been applied to their adsorption. It is my hope that continued analysis can answer remaining questions raised by my research. What happens to the polymer layer during the drastic increase in surface

area as the interface becomes spherical during emulsification? Within concentration regions where P/S complexes precipitate, is long-term surface stability feasible? Which polyacid adsorption regimes are most affected by pH changes? Can a unified theory predict P/S adsorbate amount based on polymer stiffness, charge, and concentration? At the forefront of P/S understanding at the oil/water interface are the VSF studies documented herein, where the use of a surface-specific vibrational spectroscopy reveals details that other techniques miss.

## APPENDIX A

### FITTING PARAMETERS FOR PSS/DTAB SPECTRA

**Table A.1.** Fitting parameters used for the fit to 15 mM DTAB/PSS experimental spectra shown in Figure 4.3b.

C-H region (Fig 3b)	[PSS] [h-DTAB]	0 mM 15 mM	0.10 mM 15 mM	Peak Assignment
<b>Peak 1</b>	Amplitude	0.153587	0.155298	
	Phase	0	0	
	Linewidth	2	2	
	Center	2827.45	2827.45	
	FWHM	19.713	19.7461	
<b>Peak 2</b>	Amplitude	0.536308	0.562667	CH <sub>2</sub> symmetric stretch
	Phase	0	0	
	Linewidth	2	2	
	Center	2852.39	2852.39	
	FWHM	10.2422	10.9613	
<b>Peak 3</b>	Amplitude	0.697242	0.681251	CH <sub>3</sub> symmetric stretch
	Phase	0	0	
	Linewidth	2	2	
	Center	2871.27	2871.27	
	FWHM	4.18623	4.23573	
<b>Peak 4</b>	Amplitude	0.525866	0.532663	CH <sub>2</sub> Fermi resonance
	Phase	3.14	3.14	
	Linewidth	2	2	
	Center	2913.65	2913.65	
	FWHM	7.43356	7.50369	
<b>Peak 5</b>	Amplitude	0.921836	0.929694	CH <sub>3</sub> Fermi resonance
	Phase	0	0	
	Linewidth	2	2	
	Center	2936.82	2936.82	
	FWHM	7.89286	7.21403	
<b>Peak 6</b>	Amplitude	0.0744874	0.0675237	Headgroup CH <sub>3</sub> asymmetric stretch, in-plane
	Phase	3.14	3.14	
	Linewidth	2	2	
	Center	2959.46	2959.46	
	FWHM	32.0219	6.67538	
<b>Peak 7</b>	Amplitude	0.144197	0.0872277	Headgroup CH <sub>3</sub> asymmetric stretch, out-of-plane
	Phase	0	0	
	Linewidth	2	2	
	Center	2973.84	2973.84	
	FWHM	15.2251	13.7197	
<b>Nonresonant contribution</b>	NR amp	0	0	
	NR phase	0	0	

**Table A.2.** Fitting parameters used for the fit to 15 mM d-DTAB/PSS experimental spectra shown in Figure 4.5a. The broad low-frequency signal from D<sub>2</sub>O vibrations is approximated as a nonresonant background.

C-D region (Fig 5a)	[PSS] [d-DTAB]	0.10 mM			Peak Assignment <sup>38,87</sup>
		0.20 mM	6.5 mM	15 mM	
<b>Peak 1</b>	Amplitude	3.5	3.2993	4.00792	CD <sub>3</sub> symmetric stretch
	Phase	0	0	0	
	Linewidth	11	11	11	
	Center	2069	2070.3	2070.3	
	FWHM	2.5	3	3	
<b>Peak 2</b>	Amplitude	2.23323	1.42452	2.04805	CD <sub>2</sub> symmetric stretch
	Phase	0	0	0	
	Linewidth	11	11	11	
	Center	2106.05	2104	2104	
	FWHM	3	5.86505	5.86505	
<b>Peak 3</b>	Amplitude	1.26579	1.46837	2.08218	Fermi resonance
	Phase	0	0	0	
	Linewidth	11	11	11	
	Center	2134	2132.69	2132.69	
	FWHM	4.80305	4.80305	4.80305	
<b>Peak 4</b>	Amplitude	0.6	0.264041	0.5	CD <sub>2</sub> Fermi symmetric stretch
	Phase	0	0	0	
	Linewidth	11	11	11	
	Center	2178.07	2176	2176	
	FWHM	5.35672	8	5	
<b>Peak 5</b>	Amplitude	2	0.534472	0.36756	CD <sub>3</sub> asymmetric stretch
	Phase	3.14159	3.14159	3.14159	
	Linewidth	11	11	11	
	Center	2222.93	2217	2217	
	FWHM	0.5	1	10	
<b>Nonresonant contribution</b>	NR amp	0.0982173	0.331927	0.692764	O-D stretch
	NR phase	3.14159	0	0	

**Table A.3.** Fitting parameters used for the fit to 15 mM d-DTAB/PSS spectra shown in Figure 4.5b.

C-H region (Fig 5b)	[PSS] [d-DTAB]	0.097 mM		Peak Assignment <sup>38,85</sup>
		0.20 mM	6.5 mM	
<b>Peak 1</b>	Amplitude	0.196911	0.207928	CH <sub>2</sub> symmetric stretch
	Phase	0	0	
	Linewidth	2	2	
	Center	2851.94	2852.82	
	FWHM	10.0055	10.0055	
<b>Peak 2</b>	Amplitude	0.0968791	0.0756952	CH <sub>3</sub> symmetric stretch, terminal methyl group of PSS chain
	Phase	0	0	
	Linewidth	2	2	
	Center	2878.24	2878.81	
	FWHM	18.0683	18.0683	
<b>Peak 3</b>	Amplitude	0.215688	0.238749	CH <sub>2</sub> Fermi resonance
	Phase	0	0	
	Linewidth	2	2	
	Center	2912.44	2913.55	
	FWHM	10.1938	10.1938	
<b>Peak 4</b>	Amplitude	0.0349212	0.0543373	CH <sub>3</sub> asymmetric stretch, terminal methyl group of PSS chain
	Phase	0	0	
	Linewidth	2	2	
	Center	2978.98	2980.8	
	FWHM	10.8433	10.8433	
<b>Peak 5</b>	Amplitude	0.0562828	0.114092	Aromatic C-H stretch
	Phase	0	0	
	Linewidth	2	2	
	Center	3026.21	3026.85	
	FWHM	17.3638	17.3638	
<b>Peak 6</b>	Amplitude	0.296344	0.522309	Aromatic C-H stretch
	Phase	0	0	
	Linewidth	2	2	
	Center	3064.31	3060.76	
	FWHM	10.5651	10.5651	
<b>Nonresonant contribution</b>	NR amp	0.111824	0.09	O-H stretch of trace HOD/H <sub>2</sub> O
	NR phase	0	0	

## APPENDIX B

### CALCULATION OF PAA FRACTIONAL IONIZATION

Calculating the percent ionization of simple acids and bases is done regularly in general chemistry classrooms all over the world using the well-known Henderson–Hasselbalch relationship. Unfortunately, calculating the fractional ionization of polyacids and polybases is far more complicated due to the close proximity of charged groups. In practice, the  $pK_a$  of poly(acrylic acid) (PAA) depends on PAA concentration and solution ionic strength, as will be explained in this appendix.

In 1957, R. Arnold used titrations of polymeric acids to empirically derive the relationship between fractional charge and pH,<sup>128</sup>

$$pH = pK_0 + m * f^{1/3} - \log\left(\frac{1-f}{f}\right) \quad (\text{A.1})$$

where  $pK_0$  refers to the dissociation constant of a single acid group in the uncharged molecule (i.e., the first proton to be lost from the polymer),  $f$  is the polymer fractional charge, and  $m$  is the slope of the line relating  $pK_0$  to the cube root of fractional ionization. Like  $pK_0$ ,  $m$  must be calculated empirically. Arnold reproduces the empirically derived values of  $pK_0$  and  $m$  from the thesis of a scientist named Samelson for various concentrations of PAA, reported here in Table A.1. In Chapter V, I use PAA concentrations from 0.0014 – 4.2  $mM_{\text{mono}}$ , which are within the range of the lowest two concentrations of Samelson’s data (Table A.1).

**Table A.1.**  $pK_0$  and  $m$  values reproduced from Samelson’s thesis as used by Arnold (see text).

Polymer concentration ( $mM_{\text{mono}}$ )	$pK_0$	$m$
0.871	4.25	4.09
4.36	4.13	3.75
7.81	4.02	3.58
17.4	3.82	3.55

To obtain the best approximations of  $pK_0$  and  $m$  for the PAA concentrations used in Chapter IV, Samelson’s data will be interpolated and extrapolated. The lowest three concentrations from Table A.1 were plotted in Figure A.1 and a line was fit describing how  $pK_0$  depends on PAA concentration:

$$pK_0 = -0.0331 * [PAA] + 4.2774. \quad (\text{A.2})$$

Equation A.2 was used to calculate  $pK_0$  for each of the concentrations used, as reported in Table A.2.

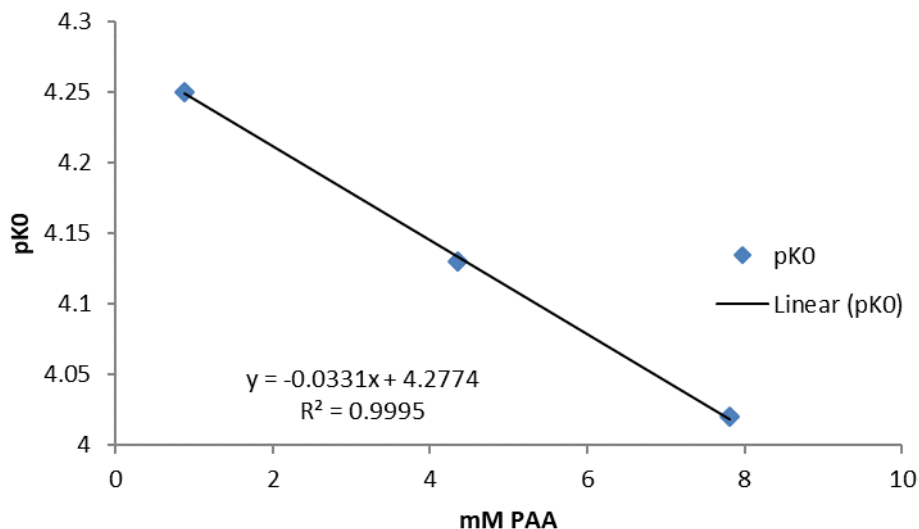


**Figure A.1.** The relationship between PAA concentration and  $pK_0$  for the lowest three concentrations reported in Table A.1.

**Table A.2.** Numerical solutions to PAA fractional ionization calculated using Equation A.1.

[PAA] (mM <sub>mono</sub> )	pH	$pK_0$	$m$	Fractional ionization
0	5.77	4.2774	4.1749	0.153347723
0.001388889	5.75	4.277354	4.174764722	0.150937764
0.004166667	5.73	4.277262	4.174494167	0.148569508
0.013888889	5.57	4.27694	4.173547222	0.130475969
0.027777778	5.55	4.276479	4.172194444	0.1284461
0.041666667	5.29	4.276019	4.170841667	0.102894333
0.083333333	5.83	4.274638	4.166783333	0.161698788
0.138888889	5.54	4.272796	4.161372222	0.128354307
0.416666667	5.36	4.263588	4.134316667	0.112267126
1.388888889	5.78	4.231361	4.039622222	0.169927065
4.166666667	6.08	4.139283	3.769066667	0.25801426

The relationship between  $m$  and PAA concentration shown in Figure A.2a is not linear, nor could it be fit comfortably with an exponential or logarithmic function. Because  $m$  depends on the cube root of the fractional charge, I should have used a third-

order polynomial. However, at the time these calculations were done, I used the line connecting the two lowest-concentration points of Table A.1:

$$m = -0.0974 * [PAA] + 4.1749. \quad (\text{A.3})$$

shown in Figure A.2b. Because the relationship between PAA concentration and  $m$  at the concentrations of interest (i.e., 0.0014 – 4.2 mM<sub>mono</sub>) is not highly curved, I believe it is a relatively safe assumption.

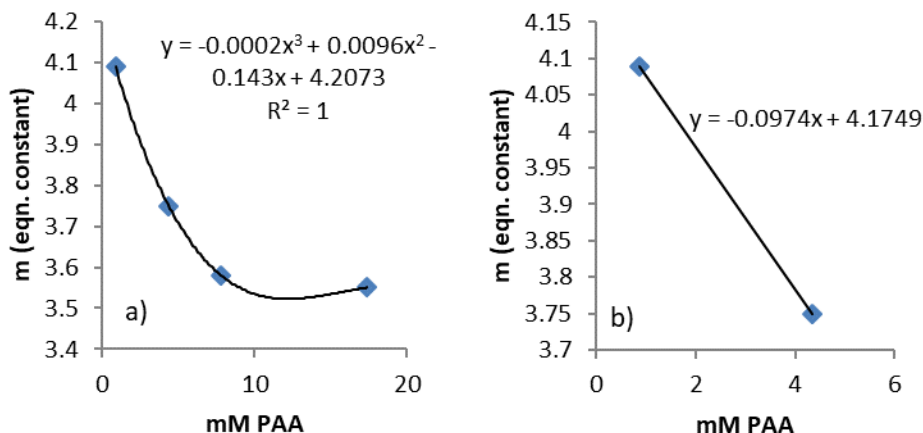


**Figure A.2.** The relationship between PAA concentration and  $m$  for PAA concentrations reported in Table A.1. In a) all concentrations are reported and fit to a third-order polynomial, while in b) the two concentrations used for interpolation are shown, along with the line they geometrically describe.

Equation A.3 was used to calculate  $m$  for the PAA concentrations of interest in Table A.2. These values, along with the measured solution pH, were put into Equation A.1 and a numerical solution for  $f$  was found using the website Wolfram|Alpha.<sup>143</sup> Fractional ionization values are reported in Figure 5.2 and Tables 5.1 and A.2.

## APPENDIX C

### FITTING PARAMETERS FOR PAA/CTAB SPECTRA

**Table C.1.** Fitting parameters used for fits to experimental spectra in Chapter V, all with 15  $\mu\text{M}$  d-CTAB. The  $\text{COO}^-$  region (a) is fit to one peak (Figure 5.7a), the  $\text{COOH}$  region (b) is fit to two peaks (Figure 5.7b), the C-D region (c) is fit to four peaks (Figure 5.6a), and the C-H region (d) is fit to four peaks (Figure 5.7c). In a – c, the broad low-frequency signal from  $\text{D}_2\text{O}$  vibrations is approximated as a nonresonant background.

a) $\text{COO}^-$ region		[PAA]	14 $\mu\text{M}$	140 $\mu\text{M}$	4200 $\mu\text{M}$
Peak 1	Amplitude		0.45856	0.503074	0.538078
	Phase		0	0	0
	Linewidth		5	5	5
	Center		1409	1409	1409
	FWHM		9.02838	9.81718	8.73215
Nonresonant contribution	Amplitude		0.07853	0.072987	0.046144
	Phase		3.14159	3.14159	3.14159

b) $\text{COOH}$ region		[PAA]	14 $\mu\text{M}$	140 $\mu\text{M}$	4200 $\mu\text{M}$
Peak 1	Amplitude		0.269634	0.352819	0.288496
	Phase		3.14159	3.14159	3.14159
	Linewidth		5	5	5
	Center		1732	1732	1732
	FWHM		55.0159	37.5275	33.2619
Peak 2	Amplitude		0.249177	0.464955	0.333523
	Phase		0	0	0
	Linewidth		5	5	5
	Center		1743	1743	1743
	FWHM		18.9063	17.1409	18.4119
Nonresonant contribution	Amplitude		0.249177	0.464955	0.333523
	Phase		0	0	0

**Table C.1. (continued).**

c) C-D region	[PAA]	0 $\mu\text{M}$	1.4 $\mu\text{M}$	14 $\mu\text{M}$	140 $\mu\text{M}$	4200 $\mu\text{M}$
Peak 1	Amplitude	0.518809	0.621887	2.97394	6.13607	5.44081
	Phase	0	0	0	0	0
	Linewidth	11	11	11	11	11
	Center	2073	2073	2073	2073	2073
	FWHM	14.6113	9.57934	2.13457	0.949172	0.847897
Peak 2	Amplitude	0.805822	0.83829	1.1808	1.11743	0.78805
	Phase	0	0	0	0	0
	Linewidth	11	11	11	11	11
	Center	2105	2105	2105	2105	2105
	FWHM	8.95979	11.2443	6.38715	5.69247	7.71354
Peak 3	Amplitude	0.432064	0.54671	0.457171	0.515417	0.347735
	Phase	0	0	0	0	0
	Linewidth	11	11	11	11	11
	Center	2134	2134	2134	2134	2134
	FWHM	12.5727	14.294	19.4849	22.8616	23.8023
Peak 4	Amplitude	0.975983	0.689617	1.34454	0.604481	0.481493
	Phase	0	0	0	0	0
	Linewidth	11	11	11	11	11
	Center	2180	2180	2180	2180	2180
	FWHM	2.20034	21.5374	1.30492	7.35035	5.7122
Nonresonant contribution	NR amp	1.08558	0.324633	0.270618	0.071594	0.042873
	NR phase	0	0	0	0	3.14159

**Table C.1. (continued).**

d) C-H region	[PAA]	14 $\mu$ M	140 $\mu$ M	4200 $\mu$ M
Peak 1	Amplitude	0.082601	0.182938	0.093172
	Phase	0	0	0
	Linewidth	10.5	10.5	10.5
	Center	2852	2852	2852
	FWHM	26.9311	29.9821	34.9642
Peak 2	Amplitude	0.097799	0.091314	0.116393
	Phase	0	0	0
	Linewidth	10.5	10.5	10.5
	Center	2900	2900	2900
	FWHM	71.2899	48.1379	122.477
Peak 3	Amplitude	0.622554	1.09603	0.965758
	Phase	0	0	0
	Linewidth	10.5	10.5	10.5
	Center	2933	2933	2933
	FWHM	26.6659	26.1373	25.6431
Peak 4	Amplitude	0.873687	1.42803	1.17452
	Phase	3.14159	3.14159	3.14159
	Linewidth	12	12	12
	Center	2942	2942	2942
	FWHM	19.1555	17.4171	21.1573
Nonresonant contribution	NR amp	0	0	0
	NR phase	0	0	0

## REFERENCES CITED

- (1) Jamtveit, B.; Meakin, P. Growth, Dissolution and Pattern Formation in Geosystems. In *Growth, Dissolution and Pattern Formation in Geosystems*; Jamtveit, B., Meakin, P., Eds.; Springer Netherlands: Dordrecht, 1999; pp 1–19. [https://doi.org/10.1007/978-94-015-9179-9\\_1](https://doi.org/10.1007/978-94-015-9179-9_1).
- (2) Overington, J. P.; Al-Lazikani, B.; Hopkins, A. L. How Many Drug Targets Are There? *Nat. Rev. Drug Discov.* **2006**, *5* (12), 993–996.
- (3) Szczepanowicz, K.; Bazylińska, U.; Pietkiewicz, J.; Szyk-Warszyńska, L.; Wilk, K. A.; Warszyński, P. Biocompatible Long-Sustained Release Oil-Core Polyelectrolyte Nanocarriers: From Controlling Physical State and Stability to Biological Impact. *Adv. Colloid Interface Sci.* **2015**, *222*, 678–691. <https://doi.org/10.1016/j.cis.2014.10.005>.
- (4) Powell, K. C.; Chauhan, A. Dynamic Interfacial Tension and Dilational Rheology of Dispersant Corexit 9500. *Colloids Surf. Physicochem. Eng. Asp.* **2016**, *497*, 352–361. <https://doi.org/10.1016/j.colsurfa.2016.03.009>.
- (5) Doshi, B.; Sillanpää, M.; Kalliola, S. A Review of Bio-Based Materials for Oil Spill Treatment. *Water Res.* **2018**, *135*, 262–277. <https://doi.org/10.1016/j.watres.2018.02.034>.
- (6) Paul, J. H.; Hollander, D.; Coble, P.; Daly, K. L.; Murasko, S.; English, D.; Basso, J.; Delaney, J.; McDaniel, L.; Kovach, C. W. Toxicity and Mutagenicity of Gulf of Mexico Waters During and After the Deepwater Horizon Oil Spill. *Environ. Sci. Technol.* **2013**, *47* (17), 9651–9659. <https://doi.org/10.1021/es401761h>.
- (7) Grigoriev, D. O.; Bukreeva, T.; Möhwald, H.; Shchukin, D. G. New Method for Fabrication of Loaded Micro- and Nanocontainers: Emulsion Encapsulation by Polyelectrolyte Layer-by-Layer Deposition on the Liquid Core. *Langmuir* **2008**, *24* (3), 999–1004. <https://doi.org/10.1021/la702873f>.
- (8) Guttoff, M.; Saberi, A. H.; McClements, D. J. Formation of Vitamin D Nanoemulsion-Based Delivery Systems by Spontaneous Emulsification: Factors Affecting Particle Size and Stability. *Food Chem.* **2015**, *171*, 117–122. <https://doi.org/10.1016/j.foodchem.2014.08.087>.
- (9) Kawakami, K.; Yoshikawa, T.; Moroto, Y.; Kanaoka, E.; Takahashi, K.; Nishihara, Y.; Masuda, K. Microemulsion Formulation for Enhanced Absorption of Poorly Soluble Drugs. *J. Controlled Release* **2002**, *81* (1), 65–74. [https://doi.org/10.1016/S0168-3659\(02\)00049-4](https://doi.org/10.1016/S0168-3659(02)00049-4).

- (10) Lochhead, R. Y.; Huisinga, L. R. A Brief Review of Polymer/Surfactant Interaction. *Cosmet. Toilet.* **2004**, *119* (2), 37–45.
- (11) Lambert, A. G.; Davies, P. B.; Neivandt, D. J. Implementing the Theory of Sum Frequency Generation Vibrational Spectroscopy: A Tutorial Review. *Appl. Spectrosc. Rev.* **2005**, *40* (2), 103–145. <https://doi.org/10.1081/ASR-200038326>.
- (12) Yang, Y. J.; Pizzolatto, R. L.; Messmer, M. C. Internal–External Reflection Sum-Frequency Generation Spectroscopy at an Interface. *J. Opt. Soc. Am. B* **2000**, *17* (4), 638. <https://doi.org/10.1364/JOSAB.17.000638>.
- (13) Shen, Y. R. Surface Properties Probed by Second-Harmonic and Sum-Frequency Generation. *Nature* **1989**, *337* (6207), 519–525. <https://doi.org/10.1038/337519a0>.
- (14) Miranda, P. B.; Shen, Y. R. Liquid Interfaces: A Study by Sum-Frequency Vibrational Spectroscopy. *J. Phys. Chem. B* **1999**, *103* (17), 3292–3307. <https://doi.org/10.1021/jp9843757>.
- (15) Shen, Y. R. Basic Theory of Surface Sum-Frequency Generation. *J. Phys. Chem. C* **2012**, *116* (29), 15505–15509. <https://doi.org/10.1021/jp305539v>.
- (16) Bain, C. D.; Davies, P. B.; Ong, T. Hui.; Ward, R. N.; Brown, M. A. Quantitative Analysis of Monolayer Composition by Sum-Frequency Vibrational Spectroscopy. *Langmuir* **1991**, *7* (8), 1563–1566. <https://doi.org/10.1021/la00056a003>.
- (17) Moore, F. G.; Becraft, K. A.; Richmond, G. L. Challenges in Interpreting Vibrational Sum Frequency Spectra: Deconvoluting Spectral Features as Demonstrated in the Calcium Fluoride—Water—Sodium Dodecylsulfate System. *Appl. Spectrosc.* **2002**, *56* (12), 1575–1578. <https://doi.org/10.1366/000370202321116048>.
- (18) Messmer, M. C.; Conboy, J. C.; Richmond, G. L. Resonant Sum Frequency Generation Studies of Surfactant Ordering at the Oil-Water Interface. In *Laser Techniques for Surface Science II*; International Society for Optics and Photonics, 1995; Vol. 2547, pp 135–142. <https://doi.org/10.1117/12.221500>.
- (19) Conboy, J. C.; Messmer, M. C.; Richmond, G. L. Investigation of Surfactant Conformation and Order at the Liquid–Liquid Interface by Total Internal Reflection Sum-Frequency Vibrational Spectroscopy. *J. Phys. Chem.* **1996**, *100* (18), 7617–7622. <https://doi.org/10.1021/jp953616x>.

- (20) Messmer, M. C.; Conboy, J. C.; Richmond, G. L. Observation of Molecular Ordering at the Liquid-Liquid Interface by Resonant Sum Frequency Generation. *J. Am. Chem. Soc.* **1995**, *117* (30), 8039–8040. <https://doi.org/10.1021/ja00135a032>.
- (21) Dick, B.; Gierulski, A.; Marowsky, G.; Reider, G. A. Determination of the Nonlinear Optical Susceptibility  $\chi(2)$  of Surface Layers by Sum and Difference Frequency Generation in Reflection and Transmission. *Appl. Phys. B* **1985**, *38* (2), 107–116. <https://doi.org/10.1007/BF00697449>.
- (22) Berry, J. D.; Neeson, M. J.; Dagastine, R. R.; Chan, D. Y. C.; Tabor, R. F. Measurement of Surface and Interfacial Tension Using Pendant Drop Tensiometry. *J. Colloid Interface Sci.* **2015**, *454*, 226–237. <https://doi.org/10.1016/j.jcis.2015.05.012>.
- (23) Jasinski, F.; Alkhatir, A.; Thickett, S. C.; Brinkhuis, R. H.; Zetterlund, P. B. Estimation of Copolymer/Water Interfacial Tensions Using Pendant Drop Tensiometry. *Langmuir* **2018**, *34* (23), 6835–6843. <https://doi.org/10.1021/acs.langmuir.8b00554>.
- (24) Stauffer, C. E. The Measurement of Surface Tension by the Pendant Drop Technique. *J. Phys. Chem.* **1965**, *69* (6), 1933–1938.
- (25) Apostoluk, W.; Drzymała, J. An Improved Estimation of Water–Organic Liquid Interfacial Tension Based on Linear Solvation Energy Relationship Approach. *J. Colloid Interface Sci.* **2003**, *262* (2), 483–488. [https://doi.org/10.1016/S0021-9797\(03\)00115-2](https://doi.org/10.1016/S0021-9797(03)00115-2).
- (26) Freitas, A. A.; Quina, F. H.; Carroll, F. A. Estimation of Water–Organic Interfacial Tensions. A Linear Free Energy Relationship Analysis of Interfacial Adhesion. *J. Phys. Chem. B* **1997**, *101* (38), 7488–7493. <https://doi.org/10.1021/jp970927u>.
- (27) Campbell, R. A.; Tummino, A.; Noskov, B. A.; Varga, I. Polyelectrolyte/Surfactant Films Spread from Neutral Aggregates. *Soft Matter* **2016**, *12* (24), 5304–5312. <https://doi.org/10.1039/C6SM00637J>.
- (28) Ábrahám, Á.; Kardos, A.; Mezei, A.; Campbell, R. A.; Varga, I. Effects of Ionic Strength on the Surface Tension and Nonequilibrium Interfacial Characteristics of Poly(Sodium Styrenesulfonate)/Dodecyltrimethylammonium Bromide Mixtures. *Langmuir* **2014**, *30* (17), 4970–4979. <https://doi.org/10.1021/la500637v>.
- (29) Campbell, R. A.; Yanez Arteta, M.; Angus-Smyth, A.; Nylander, T.; Noskov, B. A.; Varga, I. Direct Impact of Nonequilibrium Aggregates on the Structure and Morphology of Pdadmac/SDS Layers at the Air/Water Interface. *Langmuir* **2014**, *30* (29), 8664–8674. <https://doi.org/10.1021/la500621t>.

- (30) Campbell, R. A.; Yanez Arteta, M.; Angus-Smyth, A.; Nylander, T.; Varga, I. Effects of Bulk Colloidal Stability on Adsorption Layers of Poly(Diallyldimethylammonium Chloride)/Sodium Dodecyl Sulfate at the Air–Water Interface Studied by Neutron Reflectometry. *J. Phys. Chem. B* **2011**, *115* (51), 15202–15213. <https://doi.org/10.1021/jp2088803>.
- (31) Richmond, G. L. Molecular Bonding and Interactions at Aqueous Surfaces as Probed by Vibrational Sum Frequency Spectroscopy. *Chem. Rev.* **2002**, *102* (8), 2693–2724. <https://doi.org/10.1021/cr0006876>.
- (32) Gragson, D. E.; Richmond, G. L. Investigations of the Structure and Hydrogen Bonding of Water Molecules at Liquid Surfaces by Vibrational Sum Frequency Spectroscopy. *J. Phys. Chem. B* **1998**, *102* (20), 3847–3861.
- (33) Hore, D. K.; Walker, D. S.; Richmond, G. L. Water at Hydrophobic Surfaces: When Weaker Is Better. *J. Am. Chem. Soc.* **2008**, *130* (6), 1800–1801. <https://doi.org/10.1021/ja0755616>.
- (34) McFearin, C. L.; Richmond, G. L. The Role of Interfacial Molecular Structure in the Adsorption of Ions at the Liquid–Liquid Interface. *J. Phys. Chem. C* **2009**, *113* (50), 21162–21168. <https://doi.org/10.1021/jp906616c>.
- (35) Livingstone, R. A.; Nagata, Y.; Bonn, M.; Backus, E. H. G. Two Types of Water at the Water–Surfactant Interface Revealed by Time-Resolved Vibrational Spectroscopy. *J. Am. Chem. Soc.* **2015**, *137* (47), 14912–14919. <https://doi.org/10.1021/jacs.5b07845>.
- (36) Perakis, F.; Marco, L. D.; Shalit, A.; Tang, F.; Kann, Z. R.; Kühne, T. D.; Torre, R.; Bonn, M.; Nagata, Y. Vibrational Spectroscopy and Dynamics of Water. *Chem. Rev.* **2016**, *116* (13), 7590–7607. <https://doi.org/10.1021/acs.chemrev.5b00640>.
- (37) Gan, W.; Wu, D.; Zhang, Z.; Feng, R.; Wang, H. Polarization and Experimental Configuration Analyses of Sum Frequency Generation Vibrational Spectra, Structure, and Orientational Motion of the Air/Water Interface. *J. Chem. Phys.* **2006**, *124* (11), 114705. <https://doi.org/10.1063/1.2179794>.
- (38) Tyrode, E.; Hedberg, J. A Comparative Study of the CD and CH Stretching Spectral Regions of Typical Surfactants Systems Using VSFS: Orientation Analysis of the Terminal CH<sub>3</sub> and CD<sub>3</sub> Groups. *J. Phys. Chem. C* **2012**, *116* (1), 1080–1091. <https://doi.org/10.1021/jp210013g>.
- (39) Backus, E. H. G.; Bonn, D.; Cantin, S.; Roke, S.; Bonn, M. Laser-Heating-Induced Displacement of Surfactants on the Water Surface. *J. Phys. Chem. B* **2012**, *116* (9), 2703–2712. <https://doi.org/10.1021/jp2074545>.

- (40) Beaman, D. K.; Robertson, E. J.; Richmond, G. L. From Head to Tail: Structure, Solvation, and Hydrogen Bonding of Carboxylate Surfactants at the Organic–Water Interface. *J. Phys. Chem. C* **2011**, *115* (25), 12508–12516. <https://doi.org/10.1021/jp202061y>.
- (41) Seredyuk, V.; Alami, E.; Nydén, M.; Holmberg, K.; Peresytkin, A. V.; Menger, F. M. Adsorption of Zwitterionic Gemini Surfactants at the Air–Water and Solid–Water Interfaces. *Colloids Surf. Physicochem. Eng. Asp.* **2002**, *203* (1), 245–258. [https://doi.org/10.1016/S0927-7757\(01\)01106-2](https://doi.org/10.1016/S0927-7757(01)01106-2).
- (42) Knock, M. M.; Bell, G. R.; Hill, E. K.; Turner, H. J.; Bain, C. D. Sum-Frequency Spectroscopy of Surfactant Monolayers at the Oil–Water Interface. *J. Phys. Chem. B* **2003**, *107* (39), 10801–10814. <https://doi.org/10.1021/jp027047m>.
- (43) Birdi, K. S. *Handbook of Surface and Colloid Chemistry*; CRC Press: Boca Raton, 2009.
- (44) Salamah, A.; Phan, C. M.; Pham, H. G. Dynamic Adsorption of Cetyl Trimethyl Ammonium Bromide at Decane/Water Interface. *Colloids Surf. Physicochem. Eng. Asp.* **2015**, *484*, 313–317. <https://doi.org/10.1016/j.colsurfa.2015.08.010>.
- (45) Mucic, N.; Kovalchuk, N. M.; Pradines, V.; Javadi, A.; Aksenenko, E. V.; Krägel, J.; Miller, R. Dynamic Properties of CnTAB Adsorption Layers at the Water/Oil Interface. *Colloids Surf. Physicochem. Eng. Asp.* **2014**, *441*, 825–830. <https://doi.org/10.1016/j.colsurfa.2012.08.071>.
- (46) Schulze-Zachau, F.; Braunschweig, B. CnTAB/Polystyrene Sulfonate Mixtures at Air–Water Interfaces: Effects of Alkyl Chain Length on Surface Activity and Charging State. *Phys. Chem. Chem. Phys.* **2019**. <https://doi.org/10.1039/C9CP01107B>.
- (47) Trawińska, A.; Hallmann, E.; MŁdrzycka, K. The Effect of Alkyl Chain Length on Synergistic Effects in Micellization and Surface Tension Reduction in Nonionic Gemini (S-10) and Anionic Surfactants Mixtures. *Colloids Surf. Physicochem. Eng. Asp.* **2016**, *506*, 114–126. <https://doi.org/10.1016/j.colsurfa.2016.06.001>.
- (48) Pisárčik, M.; Devínsky, F.; Pupák, M. Determination of Micelle Aggregation Numbers of Alkyltrimethylammonium Bromide and Sodium Dodecyl Sulfate Surfactants Using Time-Resolved Fluorescence Quenching. *Open Chem.* **2015**, *13* (1). <https://doi.org/10.1515/chem-2015-0103>.
- (49) Taylor, D. J. F.; Thomas, R. K.; Penfold, J. Polymer/Surfactant Interactions at the Air/Water Interface. *Adv. Colloid Interface Sci.* **2007**, *132* (2), 69–110. <https://doi.org/10.1016/j.cis.2007.01.002>.

- (50) Bain, C. D.; Claesson, P. M.; Langevin, D.; Meszaros, R.; Nylander, T.; Stubenrauch, C.; Titmuss, S.; von Klitzing, R. Complexes of Surfactants with Oppositely Charged Polymers at Surfaces and in Bulk. *Adv. Colloid Interface Sci.* **2010**, *155* (1–2), 32–49. <https://doi.org/10.1016/j.cis.2010.01.007>.
- (51) Ohno, P. E.; Wang, H.; Geiger, F. M. Second-Order Spectral Lineshapes from Charged Interfaces. *Nat. Commun.* **2017**, *8* (1). <https://doi.org/10.1038/s41467-017-01088-0>.
- (52) Ohno, P. E.; Wang, H.; Paesani, F.; Skinner, J. L.; Geiger, F. M. Second-Order Vibrational Lineshapes from the Air/Water Interface. *J. Phys. Chem. A* **2018**, *122* (18), 4457–4464. <https://doi.org/10.1021/acs.jpca.8b02802>.
- (53) Ramasesha, K.; De Marco, L.; Mandal, A.; Tokmakoff, A. Water Vibrations Have Strongly Mixed Intra- and Intermolecular Character. *Nat. Chem.* **2013**, *5* (11), 935–940. <https://doi.org/10.1038/nchem.1757>.
- (54) Shen, Y. R.; Ostroverkhov, V. Sum-Frequency Vibrational Spectroscopy on Water Interfaces: Polar Orientation of Water Molecules at Interfaces. *Chem. Rev.* **2006**, *106* (4), 1140–1154. <https://doi.org/10.1021/cr040377d>.
- (55) Song, S.-H.; Koelsch, P.; Weidner, T.; Wagner, M. S.; Castner, D. G. Sodium Dodecyl Sulfate Adsorption onto Positively Charged Surfaces: Monolayer Formation With Opposing Headgroup Orientations. *Langmuir* **2013**, *29* (41), 12710–12719. <https://doi.org/10.1021/la401119p>.
- (56) Strazdaite, S.; Versluis, J.; Backus, E. H. G.; Bakker, H. J. Enhanced Ordering of Water at Hydrophobic Surfaces. *J. Chem. Phys.* **2014**, *140* (5), 054711. <https://doi.org/10.1063/1.4863558>.
- (57) De Marco, L.; Carpenter, W.; Liu, H.; Biswas, R.; Bowman, J. M.; Tokmakoff, A. Differences in the Vibrational Dynamics of H<sub>2</sub>O and D<sub>2</sub>O: Observation of Symmetric and Antisymmetric Stretching Vibrations in Heavy Water. *J. Phys. Chem. Lett.* **2016**, *7* (10), 1769–1774. <https://doi.org/10.1021/acs.jpcclett.6b00668>.
- (58) Schabes, B. K.; Hopkins, E. J.; Richmond, G. L. Molecular Interactions Leading to the Coadsorption of Surfactant Dodecyltrimethylammonium Bromide and Poly(Styrene Sulfonate) at the Oil/Water Interface. *Langmuir* **2019**, <https://doi.org/10.1021/acs.langmuir.9b00873>.
- (59) Chiappisi, L.; Hoffmann, I.; Gradzielski, M. Complexes of Oppositely Charged Polyelectrolytes and Surfactants – Recent Developments in the Field of Biologically Derived Polyelectrolytes. *Soft Matter* **2013**, *9* (15), 3896. <https://doi.org/10.1039/c3sm27698h>.

- (60) Aidarova, S.; Sharipova, A.; Krägel, J.; Miller, R. Polyelectrolyte/Surfactant Mixtures in the Bulk and at Water/Oil Interfaces. *Adv. Colloid Interface Sci.* **2014**, *205*, 87–93. <https://doi.org/10.1016/j.cis.2013.10.007>.
- (61) Braun, L.; Uhlig, M.; von Klitzing, R.; Campbell, R. A. Polymers and Surfactants at Fluid Interfaces Studied with Specular Neutron Reflectometry. *Adv. Colloid Interface Sci.* **2017**, *247* (Supplement C), 130–148. <https://doi.org/10.1016/j.cis.2017.07.005>.
- (62) Gradzielski, M.; Hoffmann, I. Polyelectrolyte-Surfactant Complexes (PESCs) Composed of Oppositely Charged Components. *Curr. Opin. Colloid Interface Sci.* **2018**, *35*, 124–141. <https://doi.org/10.1016/j.cocis.2018.01.017>.
- (63) Fauser, H.; von Klitzing, R. Effect of Polyelectrolytes on (de) Stability of Liquid Foam Films. *Soft Matter* **2014**, *10* (36), 6903–6916.
- (64) Bureiko, A.; Trybala, A.; Kovalchuk, N.; Starov, V. Current Applications of Foams Formed from Mixed Surfactant–Polymer Solutions. *Adv. Colloid Interface Sci.* **2015**, *222*, 670–677. <https://doi.org/10.1016/j.cis.2014.10.001>.
- (65) Piculell, L. Understanding and Exploiting the Phase Behavior of Mixtures of Oppositely Charged Polymers and Surfactants in Water. *Langmuir* **2013**, *29* (33), 10313–10329. <https://doi.org/10.1021/la401026j>.
- (66) Bazylińska, U.; Skrzela, R.; Szczepanowicz, K.; Warszyński, P.; Wilk, K. A. Novel Approach to Long Sustained Multilayer Nanocapsules: Influence of Surfactant Head Groups and Polyelectrolyte Layer Number on the Release of Hydrophobic Compounds. *Soft Matter* **2011**, *7* (13), 6113–6124. <https://doi.org/10.1039/C1SM05395G>.
- (67) Anton, N.; Benoit, J.-P.; Saulnier, P. Design and Production of Nanoparticles Formulated from Nano-Emulsion Templates—A Review. *J. Controlled Release* **2008**, *128* (3), 185–199. <https://doi.org/10.1016/j.jconrel.2008.02.007>.
- (68) Varga, I.; Campbell, R. A. General Physical Description of the Behavior of Oppositely Charged Polyelectrolyte/Surfactant Mixtures at the Air/Water Interface. *Langmuir* **2017**, *33* (23), 5915–5924. <https://doi.org/10.1021/acs.langmuir.7b01288>.
- (69) Thomas, R. K.; Penfold, J. Thermodynamics of the Air–Water Interface of Mixtures of Surfactants with Polyelectrolytes, Oligoelectrolytes, and Multivalent Metal Electrolytes. *J. Phys. Chem. B* **2018**, *122* (51), 12411–12427. <https://doi.org/10.1021/acs.jpcc.8b10350>.

- (70) Bahramian, A.; Thomas, R. K.; Penfold, J. The Adsorption Behavior of Ionic Surfactants and Their Mixtures with Nonionic Polymers and with Polyelectrolytes of Opposite Charge at the Air–Water Interface. *J. Phys. Chem. B* **2014**, *118* (10), 2769–2783. <https://doi.org/10.1021/jp500672f>.
- (71) Bell, C. G.; Breward, C. J. W.; Howell, P. D.; Penfold, J.; Thomas, R. K. A Theoretical Analysis of the Surface Tension Profiles of Strongly Interacting Polymer–Surfactant Systems. *J. Colloid Interface Sci.* **2010**, *350* (2), 486–493. <https://doi.org/10.1016/j.jcis.2010.07.020>.
- (72) Campbell, R. A.; Angus-Smyth, A.; Yanez Arteta, M.; Tonigold, K.; Nylander, T.; Varga, I. New Perspective on the Cliff Edge Peak in the Surface Tension of Oppositely Charged Polyelectrolyte/Surfactant Mixtures. *J. Phys. Chem. Lett.* **2010**, *1* (20), 3021–3026. <https://doi.org/10.1021/jz101179f>.
- (73) Kogej, K. Association and Structure Formation in Oppositely Charged Polyelectrolyte–Surfactant Mixtures. *Adv. Colloid Interface Sci.* **2010**, *158* (1–2), 68–83. <https://doi.org/10.1016/j.cis.2009.04.003>.
- (74) Asnacios, A.; Langevin, D.; Argillier, J. F. Mixed Monolayers of Cationic Surfactants and Anionic Polymers at the Air–Water Interface: Surface Tension and Ellipsometry Studies. *Eur. Phys. J. B - Condens. Matter Complex Syst.* **2013**, *5* (4–6), 905–911. <https://doi.org/10.1007/s100510050516>.
- (75) Kristen, N.; Vüllings, A.; Laschewsky, A.; Miller, R.; von Klitzing, R. Foam Films from Oppositely Charged Polyelectrolyte/Surfactant Mixtures: Effect of Polyelectrolyte and Surfactant Hydrophobicity on Film Stability. *Langmuir* **2010**, *26* (12), 9321–9327. <https://doi.org/10.1021/la1002463>.
- (76) Monteux, C.; Fuller, G. G.; Bergeron, V. Shear and Dilational Surface Rheology of Oppositely Charged Polyelectrolyte/Surfactant Microgels Adsorbed at the Air–Water Interface. Influence on Foam Stability. *J. Phys. Chem. B* **2004**, *108* (42), 16473–16482. <https://doi.org/10.1021/jp047462+>.
- (77) Taylor, D. J. F.; Thomas, R. K.; Penfold, J. The Adsorption of Oppositely Charged Polyelectrolyte/Surfactant Mixtures: Neutron Reflection from Dodecyl Trimethylammonium Bromide and Sodium Poly(Styrene Sulfonate) at the Air/Water Interface. *Langmuir* **2002**, *18* (12), 4748–4757. <https://doi.org/10.1021/la011716q>.
- (78) Taylor, D. J. F.; Thomas, R. K.; Li, P. X.; Penfold, J. Adsorption of Oppositely Charged Polyelectrolyte/Surfactant Mixtures. Neutron Reflection from Alkyl Trimethylammonium Bromides and Sodium Poly(Styrenesulfonate) at the Air/Water Interface: The Effect of Surfactant Chain Length. *Langmuir* **2003**, *19* (9), 3712–3719. <https://doi.org/10.1021/la020709e>.

- (79) Tummino, A.; Toscano, J.; Sebastiani, F.; Noskov, B. A.; Varga, I.; Campbell, R. A. Effects of Aggregate Charge and Subphase Ionic Strength on the Properties of Spread Polyelectrolyte/Surfactant Films at the Air/Water Interface under Static and Dynamic Conditions. *Langmuir* **2018**. <https://doi.org/10.1021/acs.langmuir.7b03960>.
- (80) Robertson, E. J.; Richmond, G. L. Chunks of Charge: Effects at Play in the Assembly of Macromolecules at Fluid Surfaces. *Langmuir* **2013**, *29* (35), 10980–10989. <https://doi.org/10.1021/la4021096>.
- (81) Robertson, E. J.; Richmond, G. L. Molecular Insights in the Structure and Layered Assembly of Polyelectrolytes at the Oil/Water Interface. *J. Phys. Chem. C* **2014**, *118* (49), 28331–28343. <https://doi.org/10.1021/jp5068022>.
- (82) Beaman, D. K.; Robertson, E. J.; Richmond, G. L. Ordered Polyelectrolyte Assembly at the Oil-Water Interface. *Proc. Natl. Acad. Sci.* **2012**, *109* (9), 3226–3231. <https://doi.org/10.1073/pnas.1200244109>.
- (83) Beaman, D. K.; Robertson, E. J.; Richmond, G. L. Unique Assembly of Charged Polymers at the Oil–Water Interface. *Langmuir* **2011**, *27* (6), 2104–2106. <https://doi.org/10.1021/la104390u>.
- (84) Robertson, E. J.; Battigelli, A.; Proulx, C.; Mannige, R. V.; Haxton, T. K.; Yun, L.; Whitelam, S.; Zuckermann, R. N. Design, Synthesis, Assembly, and Engineering of Peptoid Nanosheets. *Acc. Chem. Res.* **2016**, *49* (3), 379–389. <https://doi.org/10.1021/acs.accounts.5b00439>.
- (85) Schulze-Zachau, F.; Braunschweig, B. Structure of Polystyrenesulfonate/Surfactant Mixtures at Air–Water Interfaces and Their Role as Building Blocks for Macroscopic Foam. *Langmuir* **2017**, *33* (14), 3499–3508. <https://doi.org/10.1021/acs.langmuir.7b00400>.
- (86) Hu, D.; Chou, K. C. Re-Evaluating the Surface Tension Analysis of Polyelectrolyte-Surfactant Mixtures Using Phase-Sensitive Sum Frequency Generation Spectroscopy. *J. Am. Chem. Soc.* **2014**, *136* (43), 15114–15117. <https://doi.org/10.1021/ja5049175>.
- (87) Schabes, B. K.; Altman, R. M.; Richmond, G. L. Come Together: Molecular Details into the Synergistic Effects of Polymer–Surfactant Adsorption at the Oil/Water Interface. *J. Phys. Chem. B* **2018**, *122* (36), 8582–8590. <https://doi.org/10.1021/acs.jpcc.8b05432>.
- (88) Dogangun, M.; Ohno, P. E.; Liang, D.; McGeachy, A. C.; Be, A. G.; Dalchand, N.; Li, T.; Cui, Q.; Geiger, F. Hydrogen Bond Networks Near Supported Lipid Bilayers from Vibrational Sum Frequency Generation Experiments and Atomistic Simulations. **2018**. <https://doi.org/10.26434/chemrxiv.5946556.v2>.

- (89) Yesudas, F.; Mero, M.; Kneipp, J.; Heiner, Z. Vibrational Sum-Frequency Generation Spectroscopy of Lipid Bilayers at Repetition Rates up to 100 KHz. *J. Chem. Phys.* **2018**, *148* (10), 104702. <https://doi.org/10.1063/1.5016629>.
- (90) Wu, H.-L.; Tong, Y.; Peng, Q.; Li, N.; Ye, S. Phase Transition Behaviors of the Supported DPPC Bilayer Investigated by Sum Frequency Generation (SFG) Vibrational Spectroscopy and Atomic Force Microscopy (AFM). *Phys Chem Chem Phys* **2016**, *18* (3), 1411–1421. <https://doi.org/10.1039/C5CP04960A>.
- (91) Araoka, F.; Miyajima, D.; Aida, T.; Isoda, M.; Takezoe, H.; Oh-e, M. Liquid Crystal for Paintable Ferroelectrics. *SPIE Newsroom* **2014**. <https://doi.org/10.1117/2.1201407.005536>.
- (92) Gustafsson, E.; Hedberg, J.; Larsson, P. A.; Wågberg, L.; Johnson, C. M. Vibrational Sum Frequency Spectroscopy on Polyelectrolyte Multilayers: Effect of Molecular Surface Structure on Macroscopic Wetting Properties. *Langmuir* **2015**, *31* (15), 4435–4442. <https://doi.org/10.1021/la5046207>.
- (93) Monteux, C.; Llauro, M.-F.; Baigl, D.; Williams, C. E.; Anthony, O.; Bergeron, V. Interfacial Microgels Formed by Oppositely Charged Polyelectrolytes and Surfactants. 1. Influence of Polyelectrolyte Molecular Weight. *Langmuir* **2004**, *20* (13), 5358–5366. <https://doi.org/10.1021/la0497853>.
- (94) Monteux, C.; Williams, C. E.; Meunier, J.; Anthony, O.; Bergeron, V. Adsorption of Oppositely Charged Polyelectrolyte/Surfactant Complexes at the Air/Water Interface: Formation of Interfacial Gels. *Langmuir* **2004**, *20* (1), 57–63. <https://doi.org/10.1021/la0347861>.
- (95) Taylor, D. J. F.; Thomas, R. K.; Hines, J. D.; Humphreys, K.; Penfold, J. The Adsorption of Oppositely Charged Polyelectrolyte/Surfactant Mixtures at the Air/Water Interface: Neutron Reflection from Dodecyl Trimethylammonium Bromide/Sodium Poly(Styrene Sulfonate) and Sodium Dodecyl Sulfate/Poly(Vinyl Pyridinium Chloride). *Langmuir* **2002**, *18* (25), 9783–9791. <https://doi.org/10.1021/la020503d>.
- (96) Ge, A.; Peng, Q.; Qiao, L.; Yepuri, N. R.; Darwish, T. A.; Matsusaki, M.; Akashi, M.; Ye, S. Molecular Orientation of Organic Thin Films on Dielectric Solid Substrates: A Phase-Sensitive Vibrational SFG Study. *Phys. Chem. Chem. Phys.* **2015**, *17* (27), 18072–18078. <https://doi.org/10.1039/C5CP02702K>.
- (97) Ge, A.; Matsusaki, M.; Qiao, L.; Akashi, M.; Ye, S. Salt Effects on Surface Structures of Polyelectrolyte Multilayers (PEMs) Investigated by Vibrational Sum Frequency Generation (SFG) Spectroscopy. *Langmuir* **2016**, *32* (16), 3803–3810. <https://doi.org/10.1021/acs.langmuir.5b04765>.

- (98) Wen, Y.-C.; Zha, S.; Liu, X.; Yang, S.; Guo, P.; Shi, G.; Fang, H.; Shen, Y. R.; Tian, C. Unveiling Microscopic Structures of Charged Water Interfaces by Surface-Specific Vibrational Spectroscopy. *Phys. Rev. Lett.* **2016**, *116* (1). <https://doi.org/10.1103/PhysRevLett.116.016101>.
- (99) Socrates, G. *Infrared and Raman Characteristic Group Frequencies: Tables and Charts.*; John Wiley & Sons: West Sussex, 2007.
- (100) Regismond, S. T. A.; Gracie, K. D.; Winnik, F. M.; Goddard, E. D. Polymer/Surfactant Complexes at the Air/Water Interface Detected by a Simple Measure of Surface Viscoelasticity. *Langmuir* **1997**, *13* (21), 5558–5562. <https://doi.org/10.1021/la9702289>.
- (101) Winnik, F. M.; Regismond, S. T. A. Fluorescence Methods in the Study of the Interactions of Surfactants with Polymers. *Colloids Surf. Physicochem. Eng. Asp.* **1996**, *118* (1), 1–39. [https://doi.org/10.1016/0927-7757\(96\)03733-8](https://doi.org/10.1016/0927-7757(96)03733-8).
- (102) Bell, C. G.; Breward, C. J. W.; Howell, P. D.; Penfold, J.; Thomas, R. K. Macroscopic Modeling of the Surface Tension of Polymer–Surfactant Systems. *Langmuir* **2007**, *23* (11), 6042–6052. <https://doi.org/10.1021/la063714h>.
- (103) Saha, A.; Upadhyaya, H. P.; Kumar, A.; Choudhury, S.; Naik, P. D. Sum-Frequency Generation Spectroscopy of an Adsorbed Monolayer of Mixed Surfactants at an Air–Water Interface. *J. Phys. Chem. C* **2014**, *118* (6), 3145–3155. <https://doi.org/10.1021/jp411641z>.
- (104) Kristen, N.; Simulescu, V.; Vüllings, A.; Laschewsky, A.; Miller, R.; von Klitzing, R. No Charge Reversal at Foam Film Surfaces after Addition of Oppositely Charged Polyelectrolytes? *J. Phys. Chem. B* **2009**, *113* (23), 7986–7990. <https://doi.org/10.1021/jp902369d>.
- (105) Tucker, I. M.; Petkov, J. T.; Jones, C.; Penfold, J.; Thomas, R. K.; Rogers, S. E.; Terry, A. E.; Heenan, R. K.; Grillo, I. Adsorption of Polymer–Surfactant Mixtures at the Oil–Water Interface. *Langmuir* **2012**, *28* (42), 14974–14982. <https://doi.org/10.1021/la303563j>.
- (106) Petkova, R.; Tcholakova, S.; Denkov, N. D. Foaming and Foam Stability for Mixed Polymer–Surfactant Solutions: Effects of Surfactant Type and Polymer Charge. *Langmuir* **2012**, *28* (11), 4996–5009. <https://doi.org/10.1021/la3003096>.
- (107) Dias, R.; Mel'nikov, S.; Lindman, B.; Miguel, M. G. DNA Phase Behavior in the Presence of Oppositely Charged Surfactants. *Langmuir* **2000**, *16* (24), 9577–9583. <https://doi.org/10.1021/la000640f>.

- (108) Butler, L. N.; Fellows, C. M.; Gilbert, R. G. Effect of Surfactants Used for Binder Synthesis on the Properties of Latex Paints. *Prog. Org. Coat.* **2005**, *53* (2), 112–118. <https://doi.org/10.1016/j.porgcoat.2005.02.001>.
- (109) Hagan, E. W. S.; Charalambides, M. N.; Young, C. R. T.; Learner, T. J. S.; Hackney, S. Viscoelastic Properties of Latex Paint Films in Tension: Influence of the Inorganic Phase and Surfactants. *Prog. Org. Coat.* **2010**, *69* (1), 73–81. <https://doi.org/10.1016/j.porgcoat.2010.05.008>.
- (110) Gupta, A.; Eral, H. B.; Hatton, T. A.; Doyle, P. S. Nanoemulsions: Formation, Properties and Applications. *Soft Matter* **2016**, *12* (11), 2826–2841. <https://doi.org/10.1039/C5SM02958A>.
- (111) Monteux, C.; Williams, C. E.; Bergeron, V. Interfacial Microgels Formed by Oppositely Charged Polyelectrolytes and Surfactants. Part 2. Influence of Surfactant Chain Length and Surfactant/Polymer Ratio. *Langmuir* **2004**, *20* (13), 5367–5374. <https://doi.org/10.1021/la049784a>.
- (112) Stamkulov, N. Sh.; Mussabekov, K. B.; Aidarova, S. B.; Luckham, P. F. Stabilisation of Emulsions by Using a Combination of an Oil Soluble Ionic Surfactant and Water Soluble Polyelectrolytes. I: Emulsion Stabilisation and Interfacial Tension Measurements. *Colloids Surf. Physicochem. Eng. Asp.* **2009**, *335* (1–3), 103–106. <https://doi.org/10.1016/j.colsurfa.2008.10.051>.
- (113) Griffiths, P. C.; Paul, A.; Fallis, I. A.; Wellappili, C.; Murphy, D. M.; Jenkins, R.; Waters, S. J.; Nilmini, R.; Heenan, R. K.; King, S. M. Derivatizing Weak Polyelectrolytes—Solution Properties, Self-Aggregation, and Association with Anionic Surfaces of Hydrophobically Modified Poly(Ethylene Imine). *J. Colloid Interface Sci.* **2007**, *314* (2), 460–469. <https://doi.org/10.1016/j.jcis.2007.05.082>.
- (114) Argillier, J. F.; Zeilinger, S.; Roche, P. Enhancement of Aqueous Emulsion and Foam Stability with Oppositely Charged Surfactant/Polyelectrolyte Mixed Systems. *Oil Gas Sci. Technol. - Rev. IFP* **2009**, *64* (5), 597–605. <https://doi.org/10.2516/ogst/2009043>.
- (115) Kogej, K. Association and Structure Formation in Oppositely Charged Polyelectrolyte–Surfactant Mixtures. *Adv. Colloid Interface Sci.* **2010**, *158* (1), 68–83. <https://doi.org/10.1016/j.cis.2009.04.003>.
- (116) Iatridi, Z.; Bokias, G. Formation of Ternary Poly(Acrylic Acid)–Surfactant–Cu<sup>2+</sup> Complexes in Aqueous Solution: Quenching of Pyrene Fluorescence and PH-Controlled “On–Off” Emitting Properties. *Langmuir* **2008**, *24* (20), 11506–11513. <https://doi.org/10.1021/la8019793>.

- (117) Moore, F. G.; Richmond, G. L. Integration or Segregation: How Do Molecules Behave at Oil/Water Interfaces? *Acc. Chem. Res.* **2008**, *41* (6), 739–748. <https://doi.org/10.1021/ar7002732>.
- (118) Watry, M. R.; Richmond, G. L. Comparison of the Adsorption of Linear Alkanesulfonate and Linear Alkylbenzenesulfonate Surfactants at Liquid Interfaces. *J. Am. Chem. Soc.* **2000**, *122* (5), 875–883. <https://doi.org/10.1021/ja9917666>.
- (119) Swift, T.; Swanson, L.; Geoghegan, M.; Rimmer, S. The PH-Responsive Behaviour of Poly(Acrylic Acid) in Aqueous Solution Is Dependent on Molar Mass. *Soft Matter* **2016**, *12* (9), 2542–2549. <https://doi.org/10.1039/C5SM02693H>.
- (120) Deshiikan, S. R.; Bush, D.; Eschenazi, E.; Papadopoulos, K. D. SDS, Brij58 and CTAB at the Dodecane-Water Interface. *Colloids Surf. Physicochem. Eng. Asp.* **1998**, *136* (1), 133–150. [https://doi.org/10.1016/S0927-7757\(97\)00323-3](https://doi.org/10.1016/S0927-7757(97)00323-3).
- (121) Li, Y.; Guo, Y.; Bao, M.; Gao, X. Investigation of Interfacial and Structural Properties of CTAB at the Oil/Water Interface Using Dissipative Particle Dynamics Simulations. *J. Colloid Interface Sci.* **2011**, *361* (2), 573–580. <https://doi.org/10.1016/j.jcis.2011.05.078>.
- (122) Ram-On, M.; Cohen, Y.; Talmon, Y. Effect of Polyelectrolyte Stiffness and Solution PH on the Nanostructure of Complexes Formed by Cationic Amphiphiles and Negatively Charged Polyelectrolytes. *J. Phys. Chem. B* **2016**, *120* (26), 5907–5915. <https://doi.org/10.1021/acs.jpcc.6b01138>.
- (123) Choi, L. S.; Kim, O. K. Fluorescence Probe Studies of Poly(Acrylic Acid)-Cationic Surfactant Interactions Following High Shear. *Langmuir* **1994**, *10* (1), 57–60. <https://doi.org/10.1021/la00013a008>.
- (124) Shioi, A.; Harada, M.; Obika, M.; Adachi, M. Structure and Properties of Fluids Composed of Polyelectrolyte and Ionic Surfactant in Organic Phase: Poly(Acrylic Acid) and Didodecyldimethylammonium Bromide. *Langmuir* **1998**, *14* (17), 4737–4743. <https://doi.org/10.1021/la971283k>.
- (125) Golan, S.; Talmon, Y. Nanostructure of Complexes Between Cationic Lipids and an Oppositely Charged Polyelectrolyte. *Langmuir* **2012**, *28* (3), 1668–1672. <https://doi.org/10.1021/la204095s>.
- (126) Sulatha, M. S.; Natarajan, U. Molecular Dynamics Simulations of Adsorption of Poly(Acrylic Acid) and Poly(Methacrylic Acid) on Dodecyltrimethylammonium Chloride Micelle in Water: Effect of Charge Density. *J. Phys. Chem. B* **2015**, *119* (38), 12526–12539. <https://doi.org/10.1021/acs.jpcc.5b04680>.

- (127) Kristen-Hochrein, N.; Laschewsky, A.; Miller, R.; von Klitzing, R. Stability of Foam Films of Oppositely Charged Polyelectrolyte/Surfactant Mixtures: Effect of Isoelectric Point. *J. Phys. Chem. B* **2011**, *115* (49), 14475–14483. <https://doi.org/10.1021/jp206964k>.
- (128) Arnold, R. The Titration of Polymeric Acids. *J. Colloid Sci.* **1957**, *12* (6), 549–556. [https://doi.org/10.1016/0095-8522\(57\)90060-0](https://doi.org/10.1016/0095-8522(57)90060-0).
- (129) Lencina, M. M. S.; Miconi, E. F.; Leyes, M. D. F.; Domínguez, C.; Cuenca, E.; Ritacco, H. A. Effect of Surfactant Concentration on the Responsiveness of a Thermoresponsive Copolymer/Surfactant Mixture with Potential Application on Smart Foams Formulations. *ArXiv170702451 Cond-Mat* **2017**.
- (130) Dickhaus, B. N.; Priefer, R. Determination of Polyelectrolyte PKa Values Using Surface-to-Air Tension Measurements. *Colloids Surf. Physicochem. Eng. Asp.* **2016**, *488*, 15–19. <https://doi.org/10.1016/j.colsurfa.2015.10.015>.
- (131) Katchalsky, A.; Eisenberg, H. Molecular Weight of Polyacrylic and Polymethacrylic Acid. *J. Polym. Sci.* **1951**, *6* (2), 145–154. <https://doi.org/10.1002/pol.1951.120060202>.
- (132) Aricov, L.; Petkova, H.; Arabadzhieva, D.; Iovescu, A.; Mileva, E.; Khristov, K.; Stinga, G.; Mihailescu, C.-F.; Anghel, D. F.; Todorov, R. Aqueous Solutions of Associative Poly(Acrylates): Bulk and Interfacial Properties. *Colloids Surf. Physicochem. Eng. Asp.* **2016**, *505*, 138–149. <https://doi.org/10.1016/j.colsurfa.2016.02.018>.
- (133) Kiefer, J. J.; Somasundaran, P.; Ananthapadmanabhan, K. P. Interaction of Tetradecyltrimethylammonium Bromide with Poly(Acrylic Acid) and Poly(Methacrylic Acid). Effect of Charge Density. *Langmuir* **1993**, *9* (5), 1187–1192. <https://doi.org/10.1021/la00029a007>.
- (134) *Polymer Solutions, Blends, and Interfaces: Proceedings of the Procter and Gamble UERP Symposium*; Noda, I., Rubingh, D. N., Eds.; Studies in polymer science; Elsevier: Amsterdam ; New York, 1992.
- (135) Wan Yunus, W. M. Z.; Taylor, J.; Bloor, D. M.; Hall, D. G.; Wyn-Jones, E. Electrochemical Measurements on the Binding of Sodium Dodecyl Sulfate and Dodecyltrimethylammonium Bromide with .Alpha.- and .Beta.-Cyclodextrins. *J. Phys. Chem.* **1992**, *96* (22), 8979–8982. <https://doi.org/10.1021/j100201a052>.
- (136) Fundin, J.; Hansson, P.; Brown, W.; Lidegran, I. Poly(Acrylic Acid)–Cetyltrimethylammonium Bromide Interactions Studied Using Dynamic and Static Light Scattering and Time-Resolved Fluorescence Quenching. *Macromolecules* **1997**, *30* (4), 1118–1126. <https://doi.org/10.1021/ma950880f>.

- (137) Zhang, J.; Thomas, R. K.; Penfold, J. Interaction of Oppositely Charged Polyelectrolyte–Ionic Surfactant Mixtures: Adsorption of Sodium Poly(Acrylic Acid)–Dodecyl Trimethyl Ammonium Bromide Mixtures at the Air–Water Interface. *Soft Matter* **2005**, *1* (4), 310. <https://doi.org/10.1039/b508176a>.
- (138) Beaman, D. K.; Robertson, E. J.; Richmond, G. L. Metal Ions: Driving the Orderly Assembly of Polyelectrolytes at a Hydrophobic Surface. *Langmuir* **2012**, *28* (40), 14245–14253. <https://doi.org/10.1021/la302917p>.
- (139) Robertson, E. J.; Beaman, D. K.; Richmond, G. L. Designated Drivers: The Differing Roles of Divalent Metal Ions in Surfactant Adsorption at the Oil–Water Interface. *Langmuir* **2013**, *29* (50), 15511–15520. <https://doi.org/10.1021/la403665n>.
- (140) Robertson, E. J.; Carpenter, A. P.; Olson, C. M.; Ciszewski, R. K.; Richmond, G. L. Metal Ion Induced Adsorption and Ordering of Charged Macromolecules at the Aqueous/Hydrophobic Liquid Interface. *J. Phys. Chem. C* **2014**, *118* (28), 15260–15273. <https://doi.org/10.1021/jp503051w>.
- (141) Gordon, B. P.; Moore, F. G.; Scatena, L. F.; Valley, N. A.; Wren, S. N.; Richmond, G. L. Model Behavior: Characterization of Hydroxyacetone at the Air–Water Interface Using Experimental and Computational Vibrational Sum Frequency Spectroscopy. *J. Phys. Chem. A* **2018**, *122* (15), 3837–3849. <https://doi.org/10.1021/acs.jpca.8b01193>.
- (142) Gragson, D. E.; Richmond, G. L. Probing the Structure of Water Molecules at an Oil/Water Interface in the Presence of a Charged Soluble Surfactant through Isotopic Dilution Studies. *J. Phys. Chem. B* **1998**, *102* (3), 569–576.
- (143) Wolfram|Alpha: Making the world’s knowledge computable [www.wolframalpha.com/](http://www.wolframalpha.com/) (accessed Apr 13, 2019).